

# **USE OF CARBON BASED NANOFILLERS FOR ENERGY HARVESTING APPLICATIONS**

**Ph.D. THESIS**

*by*

**NAVJOT KAUR**



**CENTRE OF NANOTECHNOLOGY  
INDIAN INSTITUTE OF TECHNOLOGY ROORKEE  
ROORKEE – 247 667 (INDIA)  
MARCH, 2019**



# USE OF CARBON BASED NANOFILLERS FOR ENERGY HARVESTING APPLICATIONS

A THESIS

*Submitted in partial fulfilment of the requirements for the award of the degree*

*of*

DOCTOR OF PHILOSOPHY

*in*

CENTRE OF NANOTECHNOLOGY

*by*

NAVJOT KAUR



**CENTRE OF NANOTECHNOLOGY  
INDIAN INSTITUTE OF TECHNOLOGY ROORKEE  
ROORKEE – 247 667 (INDIA)  
MARCH, 2019**







**©INDIAN INSTITUTE OF TECHNOLOGY ROORKEE, ROORKEE – 2019  
ALL RIGHTS RESERVED**



# INDIAN INSTITUTE OF TECHNOLOGY ROORKEE ROORKEE

## CANDIDATE'S DECLARATION

I hereby certify that the work which is being presented in the thesis entitled “**USE OF CARBON BASED NANOFILLERS FOR ENERGY HARVESTING APPLICATIONS**”, in partial fulfilment of the requirements for the award of the Degree of Doctor of Philosophy and submitted in the Centre of Nanotechnology of the Indian Institute of Technology Roorkee, Roorkee is an authentic record of my own work carried out during a period from July, 2015 to March, 2019 under the supervision of Dr. Kaushik Pal, Associate Professor, Department of Mechanical and Industrial Engineering, Joint Faculty, Centre of Nanotechnology, Indian Institute of Technology Roorkee, Roorkee.

The matter presented in this thesis has not been submitted by me for the award of any other degree of this or any other Institution.

(NAVJOT KAUR)

This is to certify that the above statement made by the candidate is correct to the best of my knowledge.

(Dr. Kaushik Pal)  
Supervisor

Date: \_\_\_\_\_

The Ph.D. Viva-Voce Examination of **Ms. Navjot Kaur**, Research Scholar, has been held on 2<sup>nd</sup> August, 2019.

**Chairman, SRC**

**Signature of External Examiner**

This is to certify that the student has made all the corrections in the thesis.

**Signature of Supervisor (s)**

**Head of the Department**







*DEDICATED TO  
“MY BELOVED PARENTS”*

## ACKNOWLEDGEMENTS

---

First and foremost, I thank to **Almighty God**, who showered his blessings upon me and gave the strength and determination to complete the PhD Dissertation work. The research accomplishments presented herein would have never been possible without the significant contributions and enduring support of several individuals.

I would like to thank my supervisor **Dr. Kaushik Pal**, Associate Professor, Department of Mechanical and Industrial Engineering, IIT Roorkee for his advice, supervision, and crucial contribution to accomplish this research work. His involvement along with his originality has triggered and nourished my intellectual maturity that will benefit me in future.

I am highly thankful to **Dr. R. K. Dutta, Head**, Centre of Nanotechnology, IIT Roorkee for rendering all the research facilities in the Centre. I sincerely acknowledge **University Grants Commission (UGC)**, Government of India, for providing financial assistance (Maulana Azad National Fellowship (MANF No.: MANF-2014-15-SIK-PUN-47449) to perform this research work comfortably.

I feel honored and privileged to extend my gratitude to **Prof. Sumeer K. Nath**, Chairman, Student Research Committee (SRC), Professor, Department of Metallurgical and Materials Engineering, IIT Roorkee, **Dr. Prakash Biswas** (External Member, SRC), Associate Professor, Department of Chemical Engineering, IIT Roorkee and **Dr. Rajib Chowdhury** (Internal Member, SRC), Assistant Professor, Department of Civil Engineering, IIT Roorkee for their support and giving me numerous valuable insights into noble aspects of research work.

I gratefully acknowledge the Laboratory staff in Centre of Nanotechnology, Department of Mechanical and Industrial Engineering and Institute Instrumentation Centre for their help and support for the usage of equipments and conducting experiments. I would like to thank my labmates, Dr. Subhash Singh, Dr. Vinay Panwar, Mr. Souvik Bag, Mr. Jitendra Bahadur, Mr. Pushpendra Singh, Ms. Keerti Rathi, Ms. Nidhi Pal, Mr. Tushar Roy, Ms. Manmeet Kaur, Mr. Vivek Verma, Ms. Meenakshi, Ms. Swati Singh and Mr. Rishikant Sharma for their regular help and encouragement.

I am extremely thankful to my family for their love, blessings and continuous motivation throughout my Ph.D. work. I am highly obliged to my mother and acknowledge her for their unconditional love and encouragement. I want to thank my brother (Mr. Kamaljot Singh) for his constant moral support throughout this dissertation work. I would like to express my heartiest gratitude to them.

Special thanks to my friends and all other colleagues who always supported me in personal matters and present with me during my special moments.

**IIT Roorkee**

**March, 2019**

**(NAVJOT KAUR)**

## ABSTRACT

---

Energy is the essential requirement for today's life. Due to the diminution of the energy sources, it is necessary develop devices that can harvest the wasted/unused energy that exists in the ambient environment. To address this, triboelectric nanogenerators (TENGs) have been developed as an innovative paradigm for energy harvesting. TENG is a device that can harvest mechanical energy present in the surrounding environment into electrical energy by the combination of triboelectric and electrostatic induction effect. The electrical outputs obtained from TENGs depend on the friction of materials that are selected from the triboelectric series on the basis of their triboelectro-negativity and triboelectro-positivity. So, in this regard, we have selected aluminum and nylon 6,6 as triboelectro-positive materials and polyvinylidene fluoride (PVDF) as electronegative material, according to triboelectric series. In order to enhance the electronegativity of the PVDF polymer, we incorporated the carbon based nanofillers like reduced graphene oxide nanoribbons (rGONRs) and fluorinated-graphene nanoribbons (F-GNRs), which contain various functional groups such as as hydroxyl (-OH), carboxyl (-COOH), epoxy (C-O-C) and fluorine (-F), which will improve the electronegativity of the resultant materials.

So, we have synthesized rGONRs through unzipping of MWCNTs and F-GNRs via chemical modification (i.e. functionalization) of rGONRs. Moreover, we have fabricated the nanofibers of nylon 6,6, PVDF and PVDF/F-GNRs composite via electro-spinning technique. These synthesized materials are examined using various characterization techniques such as X-ray diffraction (XRD), Field emission scanning electron microscopy (FESEM), Energy-dispersive X-ray spectroscopy (EDX), Raman spectroscopy, Atomic force microscopy (AFM) and Fourier Transformation Infrared spectrophotometer (FTIR).

In this dissertation work, we have reported the comprehensive review on the triboelectric nanogenerator (TENG), fabrication of an arc-shaped single electrode mode based TENG and vertical contact-separation mode based TENG. The arch-shaped single electrode based TENG was fabricated using rGONRs/PVDF thin film act as a triboelectro-negative and aluminum would act as a triboelectro-positive material, which effectively convert mechanical energy into electrical energy. The incorporation of rGONRs in PVDF polymer enhances average surface roughness of rGONRs/PVDF thin film. With the combination of the enhancement of average

roughness and presence of various functional groups, which indicate improvement in charge trapping capacity of prepared film. The output performance was discussed experimentally as well as theoretically. The maximum peak voltage was found to be 0.35V. The newly designed TENG to harvest mechanical energy and opens up many new avenues of research in the energy harvesting applications.

In the vertical contact–separation mode based TENG using electrospun PVDF/F-GNRs and nylon nanofibers as triboelectro-negative and triboelectro-positive materials, respectively. The fabricated nanofibers were characterized and further used in the fabrication of TENG. The obtained maximum open-circuit voltage and short-circuit current are found to be 4.59 V and 98 nA, respectively, at the maximum force of 260 N. Moreover, electrical charge (Q) after 4.52 sec is examined to be 443 nC. The fabricated TENG is stable up to 2,000 cycles without any drop in output performance and also nanostructures are not get damaged. If the generated electrical output is stored in the rechargeable battery, then it could be used to drive various portable electronic devices.



## TABLE OF CONTENTS

<b>Title</b>	<b>Page No.</b>
<b>CANDIDATE'S DECLARATION</b>	i
<b>ACKNOWLEDGEMENTS</b>	v
<b>ABSTRACT</b>	vii
<b>TABLE OF CONTENTS</b>	ix
<b>LIST OF FIGURES</b>	xiii
<b>LIST OF TABLES</b>	xix
<b>LIST OF ACRONYMS</b>	xxi
<b>LIST OF NOMENCLATURE</b>	xxvii
<b>LIST OF UNITS</b>	xxix
<b>Chapter 1: INTRODUCTION</b>	1
<b>1.1 Nanotechnology</b>	4
<b>1.2 Energy</b>	5
<b>1.3 Energy Harvesting and Energy Storage</b>	5
<b>1.3.1 Energy Harvesting</b>	6
<b>1.3.2 Energy Storage</b>	7
<b>1.4 Nanogenerator</b>	7
<b>1.4.1 Piezoelectric effect</b>	8
<b>1.4.2 Pyroelectric effect</b>	9
<b>1.4.3 Triboelectric effect</b>	9
<b>1.5 Triboelectric Nanogenerator</b>	11
<b>1.6 Various Operating Modes of TENG</b>	11
<b>1.6.1 Vertical contact-separation mode</b>	12
<b>1.6.2 In-plane sliding mode</b>	12
<b>1.6.3 Single electrode mode</b>	12
<b>1.6.4 Free standing triboelectric layer mode</b>	13
<b>1.7 Applications of TENG</b>	14

<b>1.8 Objectives of Present Work</b>	16
<b>1.9 Organization of the Thesis</b>	16
<b>Chapter 2: LITERATURE REVIEW</b>	19
<b>2.1 Modes of Operation</b>	21
2.1.1 Vertical contact separation mode	21
2.1.2 Single electrode mode	42
<b>2.2 Key challenges</b>	53
<b>2.3 Factors responsible for the output of TENG</b>	53
<b>2.4 Identified Research Gaps</b>	54
<b>2.5 Research Plan</b>	54
<b>Chapter 3: EXPERIMENTAL DETAILS</b>	57
<b>3.1 Materials and Chemicals Used</b>	59
<b>3.2 Synthesis of various nanofillers</b>	59
3.2.1 Reduced oxidized graphene nanoribbons	59
3.2.2 Fluorinated-graphene nanoribbons	60
<b>3.3 Fabrication of thin film</b>	61
<b>3.4 Fabrication of nanofibers</b>	62
3.4.1 Polyamide 6,6 (nylon) nanofibers	62
3.4.2 PVDF nanofibers	65
3.4.3 PVDF/F-GNRs composite nanofibers	67
<b>3.5 Characterization Techniques and Instruments</b>	69
3.5.1 Material Characterizations	69
3.5.2 Nanogenerator Characterization	70
<b>Chapter 4: RESULTS AND DISCUSSION</b>	71
<b>Section 4.1 Effective energy harvesting from a single electrode based triboelectric nanogenerator</b>	73
4.1.1 X-ray diffraction Analysis	73
4.1.2 Fourier Transformation Infrared (FTIR) Spectroscopy	74

4.1.3	Morphological Analysis	75
4.1.4	Raman Spectroscopy Analysis	75
4.1.5	Atomic Force Microscopy (AFM)	77
4.1.6	Electrochemical Measurements	77
4.1.7	TENG Fabrication	80
Section 4.2	Fabrication of triboelectric nanogenerator using fluorinated-graphene nanoribbons and poly(vinylidene fluoride) composite nanofibers	87
4.2.1	Fabrication of TENG	87
4.2.2	Morphological Analysis	88
4.2.3	X-ray diffraction Analysis	93
4.2.4	Fourier Transformation Infrared (FTIR) Spectroscopy	95
4.2.5	Raman Spectroscopy Analysis	97
4.2.6	Mechanism behind the working of TENG	98
Chapter 5:	SUMMARY AND CONCLUSIONS	107
5.1	Research Summary	109
5.2	Conclusions	110
Chapter 6:	SCOPE FOR FUTURE WORK	111
REFERENCES		115
LIST OF PUBLICATIONS		137
PRESENTATIONS IN CONFERENCES		139





## LIST OF FIGURES

Figure No.	Figure Caption	Page No.
1.1	Relative Micro to Nano level scale	3
1.2	Diverse applications of nanotechnology	4
1.3	Different types of nanogenerators	8
1.4	Mechanism behind piezoelectric nanogenerator	8
1.5	Mechanism behind pyroelectric nanogenerator	9
1.6	A list of triboelectric series containing materials according to their tendency to gain (negative) or loose electrons (positive) in frictional and contact charging process	10
1.7	The working mechanism behind triboelectric nanogenerator	11
1.8	The diverse fundamental modes of TENG	12
1.9	Different types of energies harvested by TENG and their applications in daily life	15
3.1	Schematic diagram of synthesis process for rGONRs from unzipping of MWCNTs through chemical treatment	60
3.2	Schematic diagram of synthesis process for F-GNRs through chemical route	60
3.3	Schematic diagram of fabrication process for rGONRs/PVDF thin film	61
3.4	Schematic diagram of fabrication process of nanofibers	62
3.5	<b>(a &amp; b)</b> FESEM images of nylon nanofibers with optimization parameters (feed rate = 0.5 ml h <sup>-1</sup> , TCD = 20 cm, voltage = 20 KV) at low and high magnifications, respectively <b>(c)</b> EDAX analysis of inset nylon nanofibers <b>(d)</b> Composition of the various elements (C, N, O) present in nylon nanofibers	63
3.6	<b>(a &amp; b)</b> FESEM images of nylon nanofibers with optimization parameters (feed rate = 0.4 ml h <sup>-1</sup> , TCD = 20 cm, voltage = 20 KV), at low and high resolutions, respectively <b>(c)</b> EDAX analysis <b>(d)</b>	64

Composition of the various elements (C, N, O) present in Nylon nanofibers.

- 3.7 **(a & b)** FESEM images of PVDF nanofibers with optimization parameters (feed rate = 0.5 ml h<sup>-1</sup>, TCD = 15 cm, voltage = 11 KV) **(c)** EDAX analysis corresponding to inset PVDF nanofibers **(d)** Composition of the various elements (C, F, Al) present in PVDF nanofibers, here Al is present due to aluminium foil substrate, which was used to collect nanofibers during electrospinning 65
- 3.8 **(a & b)** FESEM images of PVDF nanofibers with optimization parameters (feed rate = 0.8 ml h<sup>-1</sup>, TCD = 10 cm, voltage = 12 KV) at high resolutions, **(c)** EDAX analysis **(d)** Composition of the various elements (C, F, Al) present in PVDF nanofibers, here Al foil is used to collect nanofibers during electrospinning 66
- 3.9 **(a & b)** FESEM images of PVDF/F-GNRs nanofibers with optimization parameters (feed rate = 0.8 ml h<sup>-1</sup>, TCD = 10 cm, voltage = 12 KV) at low and high resolutions, respectively **(c)** EDAX analysis corresponding to inset of PVDF/F-GNRs nanofibers **(d)** Composition of the various elements (C, F, O, Al) present in PVDF/F-GNRs nanofibers, here Al foil is used to collect nanofibers during electrospinning 67
- 3.10 **(a & b)** FESEM images of PVDF/F-GNRs nanofibers with optimization parameters (feed rate = 0.3 ml h<sup>-1</sup>, TCD = 10 cm, voltage = 15 KV) low and high resolutions, respectively **(c)** EDAX analysis **(d)** Composition of the various elements (C, F, O, and Al) present in PVDF/F-GNRs nanofibers, here Al foil was used to collect nanofibers during electrospinning 68
- 3.11 Electrical outputs (Current and Voltage) of fabricated TENG in initial position or without hand pressing 70
- 4.1.1 Diffraction pattern of rGONRs 73
- 4.1.2 Diffraction pattern of rGONRs/PVDF thin film 74
- 4.1.3 Fourier transform infrared (FTIR) spectroscopy of rGONRs 75

4.1.4	(a) FE-SEM image and (b) TEM image of rGONRs (c) Elemental analysis using energy dispersive X-ray analysis (EDAX) of the prepared rGONRs and the composition of C and O as shown in the inset	76
4.1.5	Raman spectra of rGONRs/PVDF thin film	76
4.1.6	3D-AFM image of the rGONRs/PVDF thin film (a & b) Side view. (c) Top view. (d) Height profile of thin film	77
4.1.7	Surface Profilometry analysis has been performed to analyze the surface morphology of the rGONRs thin film and rGONRs/PVDF thin film	78
4.1.8	Two probe I-V characteristic measurement of the pristine rGONRs and rGONRs/PVDF composite	79
4.1.9	Cyclic voltammetry of the pristine rGONRs and rGONRs/PVDF composite	79
4.1.10	(a) Schematic view of the rGONRs/PVDF based triboelectric nanogenerator (b) Optical images of triboelectric nanogenerator	80
4.1.11	(a) Optical image of rGONRs/PVDF thin film (b) FE-SEM image of thin film of rGONRs/PVDF composite	81
4.1.12	(a) Shows the schematic view of rGONRs/PVDF based single electrode TENG (b) In contact and separation mode, how the electricity is produced by TENG	82
4.1.13	(a) Output voltage of the rGONRs/PVDF based triboelectric nanogenerator (b) Output voltage of Kapton tape TENG (c) Shows that the rGONRs/PVDF based TENG was quite stable upto 500 cycles	83
4.1.14	(a) COMSOL simulations for potential distribution at different gap distances 0.2, 3, 6, 9 and 12 cm, respectively between rGONRs/PVDF thin film and Al foil. The inset shows the model for the calculation (b) Charges produced on the Al foil are decreasing by increasing the gap distance between rGONRs/PVDF film and Al foil	84

4.2.1	Fabrication of the TENG <b>(a)</b> PMMA sheet as substrate material <b>(b)</b> Aluminium (Al) is fixed in the middle part of the PMMA sheet and made four half drilled holes on the four corners <b>(c)</b> Nanofibers via electro-spinning method are fabricated on the Al sheet <b>(d)</b> Both the substrates are assembled, where springs are used for maintaining the gap distance between them <b>(e)</b> Optical image of the fabricated TENG	87
4.2.2	<b>(a)</b> FE-SEM analysis of the nylon nanofibers at low resolution and <b>(b)</b> Highly magnified image of the nylon nanofibers <b>(c)</b> EDAX analysis with weight% and atomic% corresponding to various elements present <b>(d)</b> Diameter distribution histogram of the nylon nanofibers	88
4.2.3	<b>(a)</b> Elemental mapping of the nylon nanofibers <b>(b)</b> EDAX line frequency maps of the elements present in the nylon nanofibers	89
4.2.4	<b>(a) &amp; (b)</b> FE-SEM analysis at high magnification of the PVDF nanofibers <b>(c)</b> EDAX analysis for various elements present in the PVDF nanofibers <b>(d)</b> Diameter distribution histogram of the PVDF nanofibers	90
4.2.5	<b>(a)</b> Elemental mapping and <b>(b)</b> EDAX line frequency maps scan of the PVDF nanofibers	90
4.2.6	<b>(a)</b> SEM image of the synthesised rGONRs through unzipping of Multiwalled-CNTs <b>(b)</b> EDAX analysis shows the weight% of the elements exists in the rGONRs <b>(c)</b> EDAX analysis shows the weight% of the elements exists in the fluorinated-GNRs (F-GNRs) <b>(d)</b> SEM image of the synthesised F-GNRs from rGONRs through HF acid treatment	91
4.2.7	<b>(a)</b> FE-SEM image of the PVDF/F-GNRs nanofibers <b>(b)</b> Highly magnified image of the composite (PVDF/F-GNRs) nanofibers <b>(c)</b> EDAX analysis of composite nanofibers <b>(d)</b> Diameter distribution histogram of the composite nanofibers	92

4.2.8	(a) Elemental mapping distribution for various elements exist in the sample (b) EDAX line frequency maps of the elements present in the composite nanofibers	93
4.2.9	X-ray Diffraction pattern of (a) fluorinated-GNRs (F-GNRs) (b) rGONRs	94
4.2.10	XRD patterns of (a) PVDF/F-GNRs composite nanofibers (b) Pristine PVDF nanofibers and (c) Nylon 6,6 nanofibers	95
4.2.11	Fourier Transformer infrared (FTIR) spectrum of (a) Pristine PVDF nanofibers and PVDF/F-GNRs composite nanofibers (b) Nylon 6,6 nanofibers	96
4.2.12	Fourier Transformer infrared (FTIR) spectrum of rGONRs and fluorinated-GNRs (F-GNRs)	97
4.2.13	RAMAN Spectroscopy of (a) rGONRs and (b) fluorinated-GNRs (F-GNRs)	98
4.2.14	(a) Schematic of the fabricated TENG (b-f) Working mechanism of the TENG. (b) Initial position, when no external mechanical force is applied (c) By applying external force on the top substrate, it brings PVDF/F-GNRs nanofibers layer into contact with nylon nanofibers layer, generating negative triboelectric charges on the PVDF/F-GNRs side and positive charges on the nylon side (d) By removing the external force, separation between the electrodes occurs and potential difference drives the electrons from the lower electrode to the top electrode, triboelectric charges are distributed on the surfaces and the inductive charges are left behind (e) Initial position is achieved by all the negative triboelectric charges distributed on the contact surface (f) As the force is reapplied, the electrons flow back towards the lower side electrode for screening the inductive charges Note: For the structure simplification, springs and nanofibers morphology in the schematics are not shown	99
4.2.15	Electrical outputs of the fabricated TENG using pristine PVDF and nylon nanofibers: (a) $V_{OC}$ (volts) (inset: mechanical energy is applied on the TENG to get the output) and (b) $I_{SC}$ (nA) For	101

fabricated TENG using PVDF/F-GNRs and nylon nanofibers: **(c)**  $V_{OC}$  (volts) and **(d)**  $I_{SC}$  (nA) **(e)** Schematic for dispersion of F-GNRs in a PVDF nanofiber, and stored surface charge on the PVDF/F-GNRs nanofibers

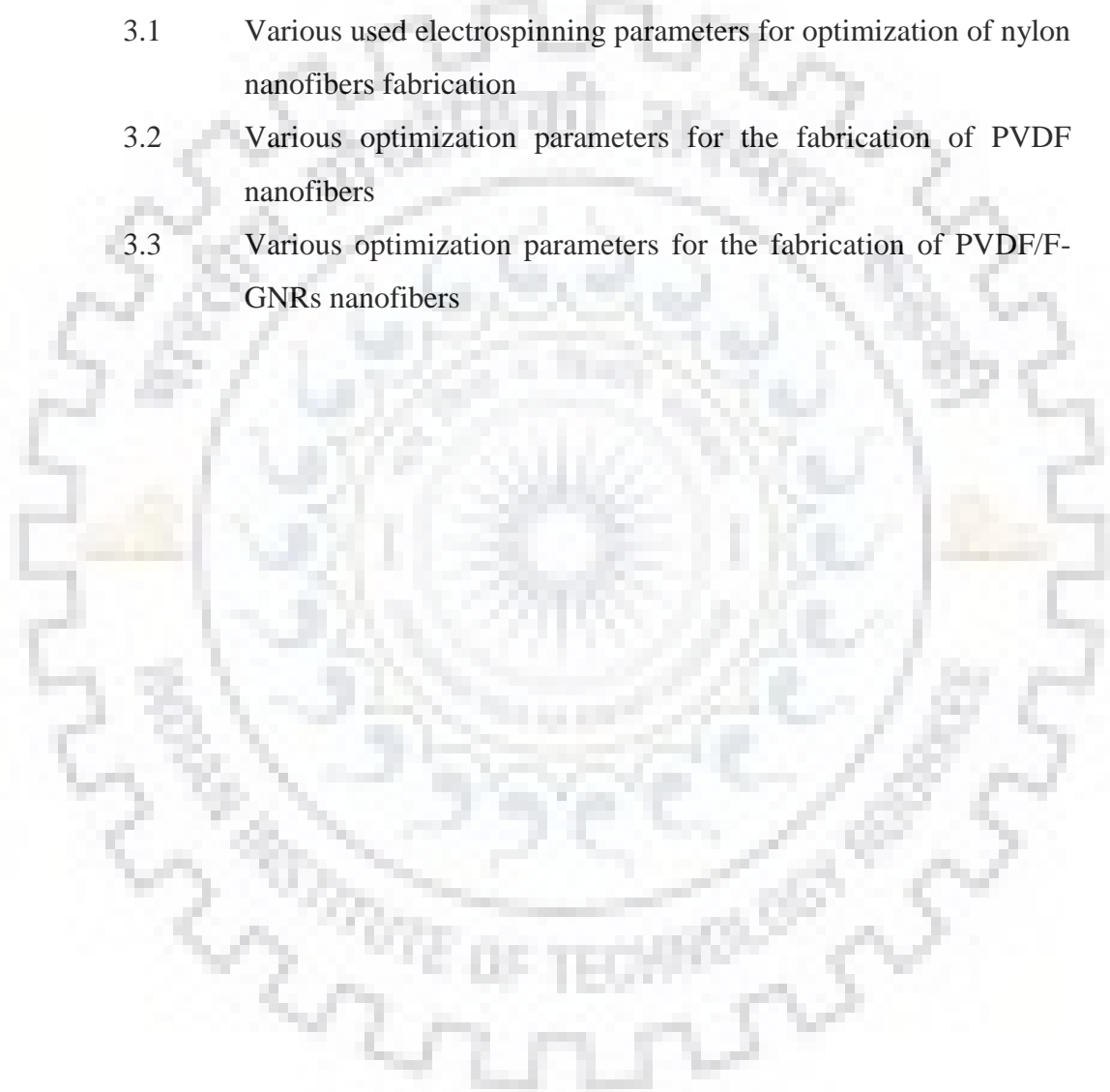
4.2.16 Electrical outputs (Current and Voltage) of fabricated TENG in hand pressing mode 103



## LIST OF TABLES

---

<b>Table No.</b>	<b>Table Caption</b>	<b>Page No.</b>
2.1	Comparative study for different modes of fabricated TENGs	49
3.1	Various used electrospinning parameters for optimization of nylon nanofibers fabrication	63
3.2	Various optimization parameters for the fabrication of PVDF nanofibers	67
3.3	Various optimization parameters for the fabrication of PVDF/F-GNRs nanofibers	69







## LIST OF ACRONYMS

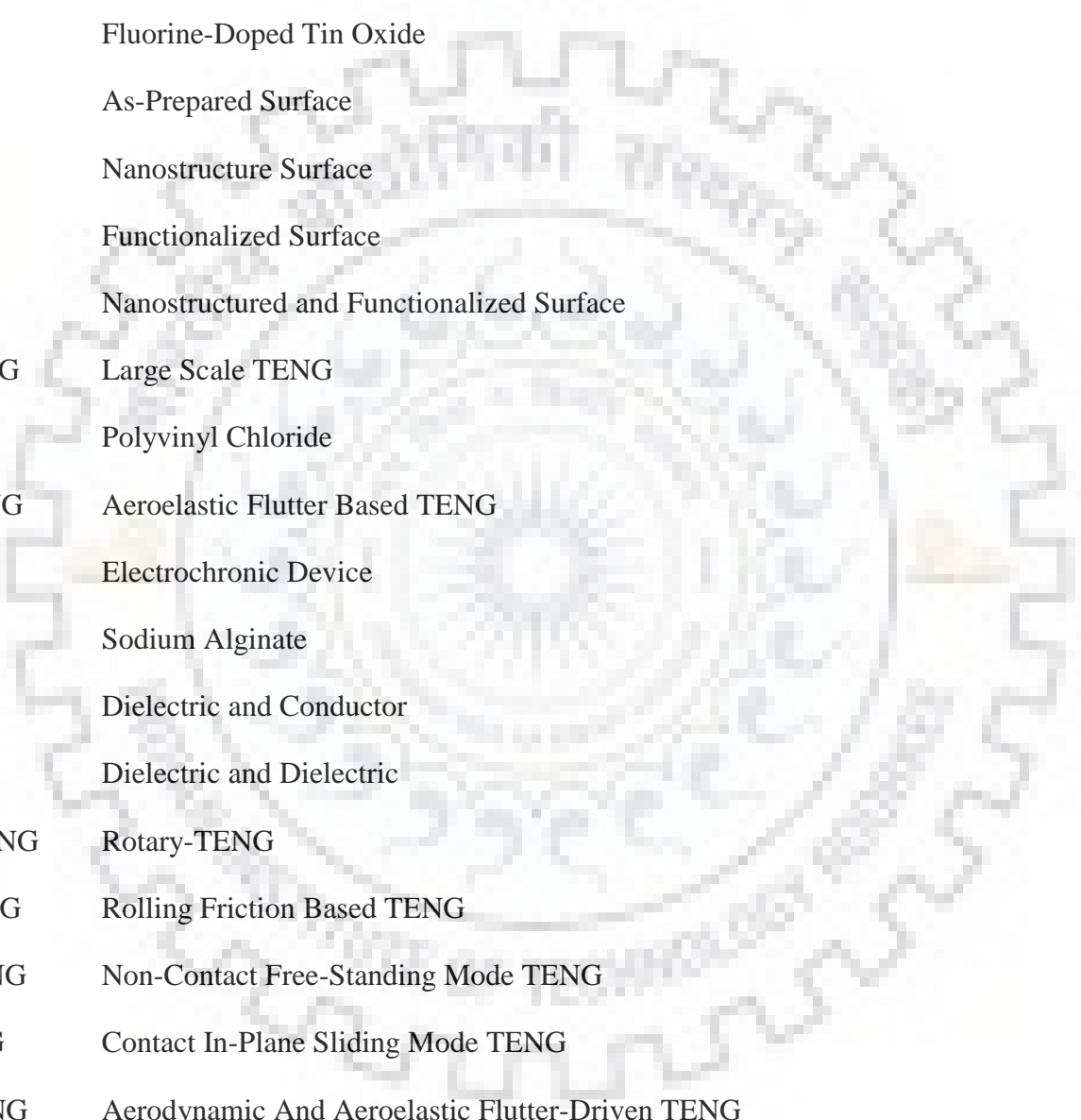
---

MEMS	Micro-Electromechanical Systems
NEMS	Nano-Electromechanical Systems
PTFE	Polytetrafluoroethylene
FESEM	Field-Emission Scanning Electron Microscopy
FEP	Fluorinated Ethylene Propylene
HDPE	High-Density Polyethylene
PP	Polypropylene
PET	Polyethylene Terephthalate/Polyester
PMMA	Poly(Methyl Methacrylate)
PVDF	Polyvinylidene difluoride or Polyvinylidene Fluoride
PI	Polyimide or kapton
Al	Aluminium
SiO <sub>2</sub>	Silicon Dioxide
Si <sub>3</sub> N <sub>4</sub>	Silicon Nitride
Al <sub>2</sub> O <sub>3</sub>	Aluminium Oxide
BaTiO <sub>3</sub>	Barium Titanate
ZnO	Zinc Oxide
AlN	Aluminium Nitride
KNbO <sub>3</sub>	Potassium Niobate
NG	Nanogenerator
TENG	Triboelectric Nanogenerator
ITO	Indium Tin Oxide

Ag	Silver
Au	Gold
LEDs	Light-Emitting Diodes
Pb	Lead
NW	Nanowires
Li	Lithium
rGONRs	Reduced Graphene Oxide Nanoribbons
F-GNRs	Fluorinated-Graphene Nanoribbons
PDMS	Polydimethylsiloxane
PECVD	Plasma-Enhanced Chemical Vapour Deposition
PVA	Polyvinyl Alcohol
AAO	Anodic Aluminium Oxide
SEM	Scanning Electron Microscope
ID	Instantaneous Discharge
CD	Continuous Discharging
PA	Polyamide 6,6
PVD	Pulsed Vapour Deposition
Cu	Copper
EC	Ethyl Cellulose
PLLA	Poly-L-Lactic Acid
P(VDF-HFP)	Poly(Vinylidene Fluoride-Co-Hexafluoropropylene)
NaOH	Sodium Hydroxide
UVO	Ultraviolet-Ozone
PHBV	Poly(3-Hydroxybutyrate-Co-3-Hydroxyvalerate)

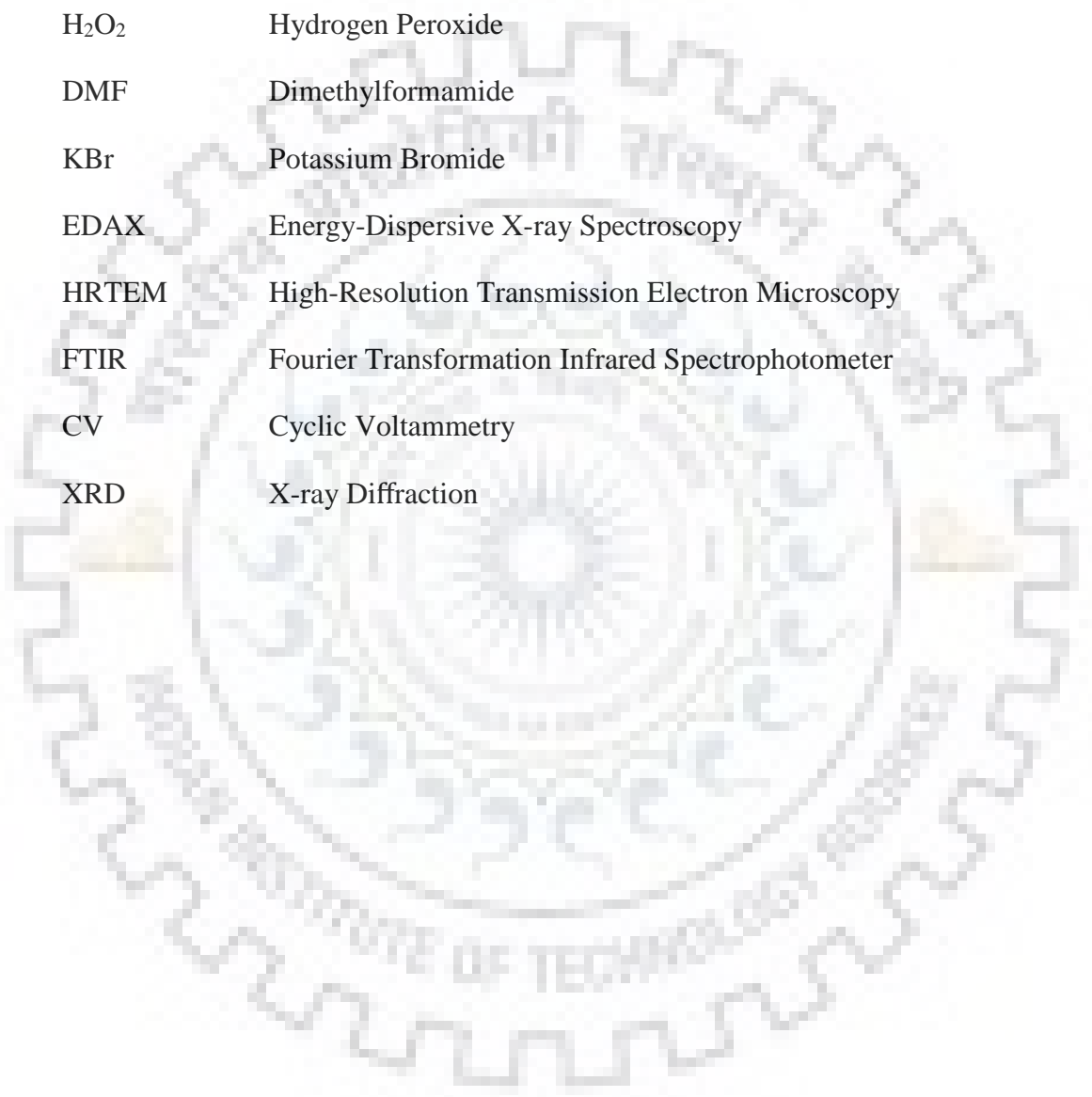


GO	Graphene Oxide
PMNF	Porous Micro-Nickel Foam
AuNF	Gold Nanoflowers
MWCNT	Multiwalled Carbon Nanotubes
RH	Single Rice Husk
ARH	Rice Husk Array
PFTS	1H,1H,2H,2H-Per-Fluorooctyltrichlorosilane
PS	Polystyrene
B-TENG	Elastic Bellow-TENG
ESD	Electrostatic Discharge
PPy	Polypyrrole
SPS	Self-Powered Synthesis
SCPS	Self-Charging Power System
WAO	Water-Assisted Oxidation
CO <sub>2</sub>	Carbon Dioxide
DI	Deionized
UV	Ultraviolet
CCS-TENG	Corrugated-Core Sandwich-Structured TENG
PSR	Portable Self-Retracting
LCD	Liquid Crystal Display
CNTs	Carbon Nanotubes
PU	Polyurethane
ICP	Inductively Coupled Plasma
PCB	Printed Circuit Broad



r-TENG	Rotating TENG
T-TENG	Transparent TENG
FEM	Finite Element Method
AFM	Atomic Force Microscopy
FTO	Fluorine-Doped Tin Oxide
AP	As-Prepared Surface
NS	Nanostructure Surface
FS	Functionalized Surface
NFS	Nanostructured and Functionalized Surface
LS-TENG	Large Scale TENG
PVC	Polyvinyl Chloride
AF-TENG	Aeroelastic Flutter Based TENG
ECD	Electrochromic Device
SA	Sodium Alginate
D-C	Dielectric and Conductor
D-D	Dielectric and Dielectric
2D r-TENG	Rotary-TENG
RF-TENG	Rolling Friction Based TENG
NC-TENG	Non-Contact Free-Standing Mode TENG
C-TENG	Contact In-Plane Sliding Mode TENG
FM-TENG	Aerodynamic And Aeroelastic Flutter-Driven TENG
O <sub>2</sub>	Oxygen
Ar	Argon
HF	Hydrofluoric Acid

H <sub>2</sub> SO <sub>4</sub>	Concentrated Sulphuric Acid
DCM	Dichloromethane
DMAc	Dimethylacetamide
KMnO <sub>4</sub>	Potassium Permanganate
H <sub>2</sub> O <sub>2</sub>	Hydrogen Peroxide
DMF	Dimethylformamide
KBr	Potassium Bromide
EDAX	Energy-Dispersive X-ray Spectroscopy
HRTEM	High-Resolution Transmission Electron Microscopy
FTIR	Fourier Transformation Infrared Spectrophotometer
CV	Cyclic Voltammetry
XRD	X-ray Diffraction





## LIST OF NOMENCLATURES

---


$s/v$	surface to volume ratio
$V_{OC}$	open circuit voltage
$I_{SC}$	short circuit current
$I_{CC}$	closed circuit current
$J_{SC}$	short-circuit current density
$\epsilon_0$	vacuum permittivity
$\sigma$	triboelectric charge density
$d$	gap distance among the two materials
$\sigma'$	induced charge density
$d_1$	thickness of the PMMA layer
$d_2$	thickness of the kapton film
$\epsilon_{rp}$	relative permittivity of PMMA film
$\epsilon_{rk}$	relative permittivity of kapton film
$\sigma$	charge density
$S$	area around the plate
$x(t)$	the separation between Al and kapton films
$d$	the thickness of kapton film
$\epsilon_r$	relative dielectric constant of the kapton film
$\epsilon_0$	dielectric constant of the vacuum
$f_0$	natural frequency
$k$	the stiffness coefficient
$m_0$	mass of the upper substrate plus the Al film



$\Delta Q$	transferred charge quantity
$\lambda$	wavelength of the incident light
$n_0$	refractive indices of air
$n_1$	refractive indices of PTFE film
$n_2$	refractive indices of FTO
$I_D/I_G$	ratio of intensity for D and G bands
$W$	instantaneous power output,
$I_{peak}$	peak value of $I_{sc}$
$R$	load resistance applied in the circuit
$E_1, E_2, \text{ and } E_{air}$	electric-field strengths
$t_1$	thicknesses of the nylon nanofibers layer
$t_2$	thicknesses of the PVDF/F-GNRs nanofibers layers
$d$	gap distance among both the induced surfaces
$\epsilon_{r1} \text{ and } \epsilon_{r2}$	relative permittivity of both the layers
$A$	Area of the electrode
$Q$	transferred charges between the electrodes
$\sigma$	theoretically charge density
$\lambda$	wavelength of the incident light
$n_0$	refractive indices of air
$n_1$	refractive indices of the PTFE film
$n_2$	refractive indices of FTO
$k$	constant

## LIST OF UNITS

---



$V$	Volt
$kV$	Kilovolt
$nm$	Nanometre
$mm$	Millimetre
$\mu m$	Micrometre
$m$	Meter
$\mu A$	Micro-ampere
$nA$	Nano-ampere
$mA$	Milli-ampere
$ml$	Milliliter
$\mu L$	Microliter
$\mu A m^{-2}$	Microampere per meter square
$mA cm^{-2}$	Milliampere per centimetre square
$nA cm^{-2}$	Nanoampere per centimetre square
$mA m^{-2}$	Milliampere per meter square
$A m^{-2}$	Ampere per meter square
$\mu W m^{-2}$	Micro-Watt per meter square
$\mu W cm^{-2}$	Micro-Watt per centimetre square
$W m^{-2}$	Watt per meter square
$mW m^{-2}$	Milliwatt per meter square
$mW cm^{-2}$	Milliwatt per kilometre square
$W m^{-3}$	Watt per meter cube

$W$	Watt
$\mu W$	Micro-watt
$MW$	Mega-watt
$\Omega$	Ohms
$k\Omega$	Kilo ohms
$M\Omega$	Mega ohms
$G\Omega$	Giga ohms
$m s^{-1}$	Meter per second
$m s^{-2}$	Meter per second square
$\mu F$	Micro-farad
$Rad s^{-1}$	Radian per second
$rpm$	Revolutions per minute
$\mu C$	Micro-coulomb
$s$	Second
$min$	Minutes
$h$	Hour
$cm$	Centimetre
$cm^2$	Centimetre square
$cm^3$	Centimetre cube
$km^2$	Kilometre square
$mAh$	Milliamp hour
$Hz$	Hertz
$mg$	Milligram
$g$	Gram

$Pa$	Pascal
$kPa$	Kilopascal
$N$	Newton
$\theta$	Angle degree
$Hz/ms^{-1}$	Hertz/ meter per second
$\mu A MPa^{-1}$	Micro-ampere per mega pascal
$mLs^{-1}$	Millilitre per second
$nA kPa^{-1}$	Nanoampere per killo-Pascal
$V kPa^{-1}$	Volt per killoPascal
$V mm^{-1}$	Volt per millimetre
$nA mm^{-1}$	Nanoampere per millimetre
$\mu C m^{-2}$	Micro-coulomb per meter square
$mV g^{-1}$	Millivolt per gram
$wt\%$	Weight percent
$mJ$	Millijoule
$nC J^{-1}$	Nano coulomb per joule
$N m^{-1}$	Newton per meter
$ml h^{-1}$	Millilitre per hour
$mV s^{-1}$	Millivolt per second
$\Omega \mu m^{-2}$	Ohm per micrometre square



## Chapter 1

### INTRODUCTION

---



Bulk materials are those macroscopic materials, which are present around us, could be seen with naked eye and possess continuous physical properties. The micron-sized particles (e.g., pollen grain, dust, etc.) also retain same properties as that of macroscopic materials. Nonetheless, when any dimension of substance is reduced to nano-scale dimension (i.e. between 1 - 100 nm) the substance starts behaving in peculiar way. Here, quantum mechanics is used to describe such peculiarity as due to failure of classical physics. The materials at nano-scale exhibit different physical, chemical, electrical, optical and bio-logical properties to their macro/micro-scopic counterpart. For example, gold nanoparticles exhibit entirely different properties (e.g., electrical, mechanical, optical, etc.) as that from bulk. **Figure 1.1** demonstrates the scale from millimetre (mm) to nanometre (nm) with the examples in the respective scale.

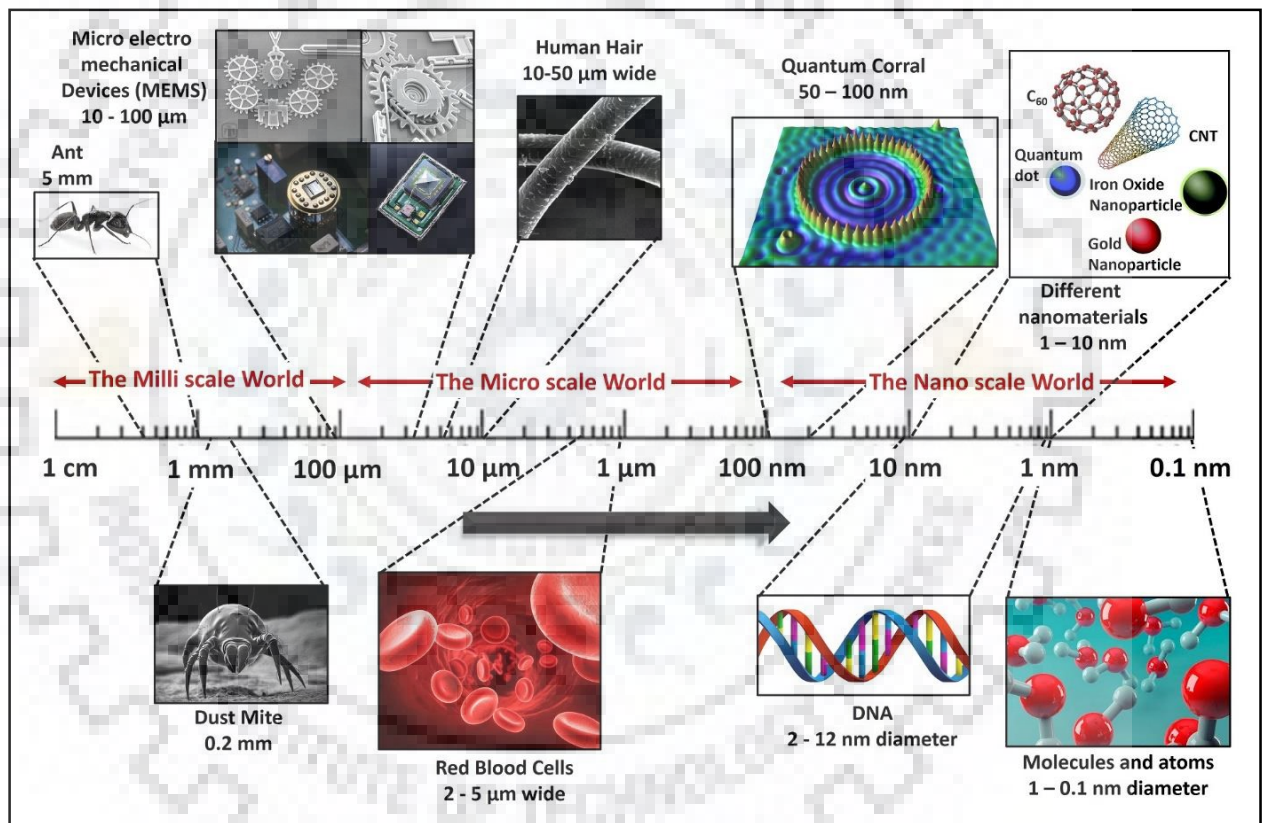


**Figure 1.1.** Relative Micro to Nano level scale

In 1959, the concept nanotechnology was first conferred in the talk ‘There’s Plenty of Room at the Bottom’, which was delivered by renowned physicist Richard Feynman. Then in 1974, Norio Taniguchi was the first person, who used the term “Nanotechnology”, however it was not known extensively.

## 1.1 Nanotechnology

Nanotechnology may be defined as the utilization of materials and device or system fabrications by controlling materials, manipulating and assembly of supermolecules, molecules, atoms structures on the nanometer scale i.e. atleast one of the dimension is in nanometer (1-100 nm). In the recent past, nanotechnology has been eminently overwhelmed multi-disciplinary fields for instance chemistry, applied chemistry, chemical engineering, materials science, physics, applied physics, mechanical engineering, biological engineering, electrical and electronic engineering and so on. As the dimension of the materials is reduced to nano level (Figure 1.1), then various properties drastically changed from their bulk state, this is due to the quantum confinement phenomena. When the material reaches at nano-scale, surface to volume ratio (s/v) intensively increases. Additionally, surface energy also influences many properties like physical, chemical, and mechanical due to which nanomaterials becomes more ductile, durable and also show many innovative properties, which open new vistas for research in various fields, which do not exist in the bulk material.

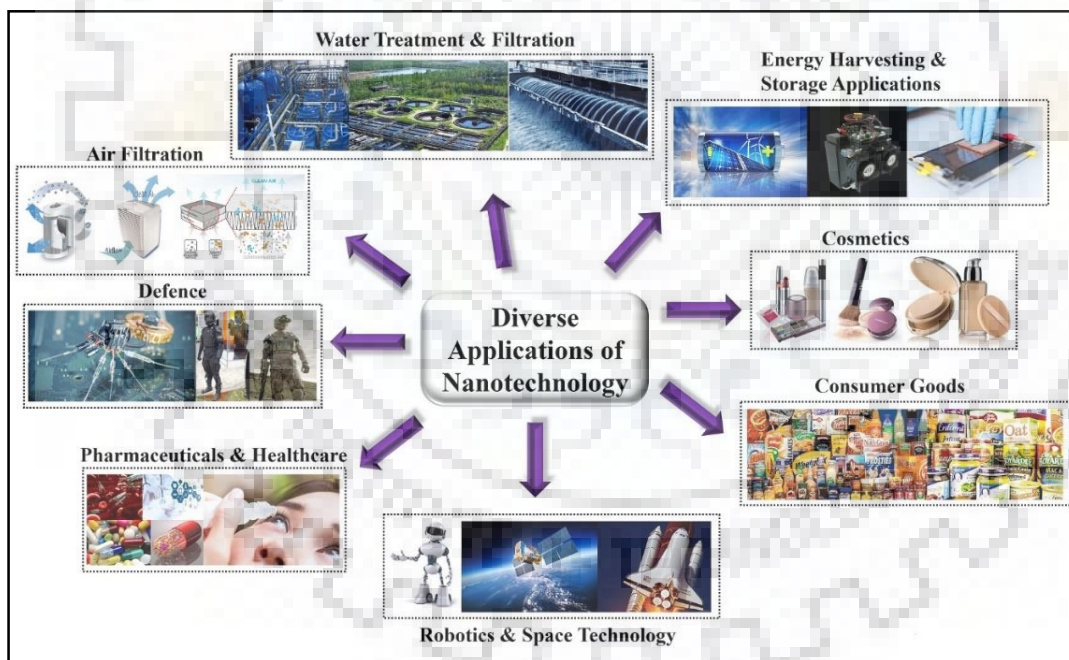


**Figure 1.2.** Diverse applications of nanotechnology

Due to these different unique properties, the nanomaterials have many applications in the various field such as nanobiotechnology, energy harvesting and storage, water treatment, air pollution control, aerospace, nano-foods, surface coatings, textiles, cosmetics, electronics gadget, spintronics devices, sensors and so on as shown in **Figure 1.2**. Among these applications, the energy harvesting and storage using nanomaterials create much attention towards our daily life.



## **1.2 Energy**

Energy is one of the utmost essential resource that dictate the excellence towards our today's life. However, with the energy crises and menace of global warming, we have to search green and renewable energy resources, which is one of the challenge for human society to sustainable development. For powering the world today, well-known energy resources like hydroelectricity, coal, petroleum, and natural gases are naturally available and in addition to these resources, the alternative energy resources such as solar energy, nuclear energy, biomass energy, geothermal and wind energy are also available. But at small scale, for powering small electronic devices, which includes micro-electromechanical systems (MEMS), nano-electromechanical systems (NEMS), maintenance-free, wireless sensor network and even portable wearable/portable personal electronic devices, etc.; energy is also perilously needed.

Nowadays, energy-harvesting techniques are drawing much attention because of the increasing demands of the society for self-powered and autonomous sensors. Fossil fuel energy is very limited for the next generation, which turns the focus of research society to develop a new eco-friendly energy source from available renewable energy sources. There are various renewable energy sources that are already familiar such as, water, wind, solar energy and so on. The main efforts of these energy resources are to fulfil the requirements of major target grid i.e. in mega- to giga-watt power scales. The factors to be considered while choosing these kinds of resources are good efficiency, inexpensiveness, and better reliability.

In recent years, applications and dissemination of portable electronics devices have grasped every part of our day-to-day life. Various kinds of sensor-enabled devices for environmental protection, health monitoring, infrastructure monitoring, security, and medical care have already flourished. The power required to drive such small units is very small (in the microwatt range). By 2020, Cisco has predicted that the world would have trillions of sensor-enabled units distributed all over the earth [1]. So, it has become necessity to develop the technique with which one can drive the various wearable electronic devices, without using power banks, etc. Nowadays, harvesting various types of energies (thermal/mechanical, wind, water, solar, etc.) into usable form is attracting much more attention.

## **1.3 Energy Harvesting and Energy Storage**

Energy harvesting and energy storage are the two different approaches, which are carried out simultaneously.

### 1.3.1 Energy Harvesting

Energy harvesting is the technique, in which energy from ambient sources is converted into useful energy and this energy is further used for driving the wearable devices. It is becoming essential due to the increasing requirements of electronic devices; portability has become a necessity for today's life. The cell phones, smart watches, portable music players, tablet computers, etc., are common examples of portable electronic devices and have become a part of daily life. So, it is essential to develop a technique that can charge these portable devices. Wires and batteries such as Li-ion batteries are not efficient and durable, so the research community must think of an alternate device that would be more stable, cheaper, and function for a long time. Today, energy harvesting is generated via human actions for the purpose of communication, safety health, and so on. The most common energy allied with human activities is mechanical energy (human body motions), which could also be termed as wasted energy. Wasted energy also includes photovoltaic energy, thermal energy, and mechanical energy, which are available in our daily life and are very beneficial from the view point of portable devices applications. Nanogenerators (NGs) have been introduced to harvest human energy, that is, from breathing, walking, running and etc. There are other feasible techniques based on electromagnetic, electrets, and piezoelectric vibrational energy harvesters that convert mechanical energy into electrical energy. There are other feasible techniques based on electromagnetic, electrets, piezoelectric vibrational energy harvesters, solar cells, and etc., that convert one form of energy into another [2–11].

The electromagnetic micro power generators operate on the principle of the electromagnetic effect, in which relative motion between used permanent magnet and coil or conductor to transform electrical energy according to the Faraday's laws of induction [12]. The term 'electret' is formed by the combining two terms, i.e. electron and magnet and is described as a nascent class of solid dielectric materials (organic and inorganic), including Polytetrafluoroethylene (PTFE), Fluorinated ethylene propylene (FEP), High-density polyethylene (HDPE), Polypropylene (PP), Polyethylene terephthalate (PET), Poly(methyl methacrylate) (PMMA), Polyvinylidene fluoride (PVDF), Polyimide (PI), Silicon dioxide ( $\text{SiO}_2$ ), Silicon Nitride ( $\text{Si}_3\text{N}_4$ ), Aluminium oxide ( $\text{Al}_2\text{O}_3$ ), and etc. having an ability to fix the quasi-permanent electric moment or long term dipole charge storage capacity, which provides an external electric field in the deficiency of an applied field [13]. However, organic electret materials exhibit high charge density and good stability in comparison of inorganic. A micro power generator based on electrets produces electricity by harvesting energy from diverse human

motions such as touching, tapping, rubbing, and mechanical vibrations [12,14]. In the electret power generator, the dielectric material (electret) is fixed onto the prepared electrode and then charged with a Corona charging process [12,15], which converts the electret into a quasi-permanent dipole charged material and hence generates primary surface potential with constant electrostatic field [15]. A piezoelectric micro power generator uses piezoelectric effects, in which piezoelectric materials such as Barium titanate ( $\text{BaTiO}_3$ ), Zinc oxide ( $\text{ZnO}$ ), Aluminium nitride ( $\text{AlN}$ ), Potassium niobate ( $\text{KNbO}_3$ ) etc., can produce electricity when subjected to mechanical stress or when both sides of material are under pressure [12]. Solar cell is the device that converts the sunlight direct into electrical energy using photovoltaic effect [16–18].

It is necessary to incorporate energy harvesting with the battery to build self-powered devices. This would act as the background for the nanogenerator and be an innovative approach for nanoenergy. In 2006, Wang *et al.* introduced a nanogenerator that successfully used an atomic force microscopy (AFM) tip to scavenge vibrational, mechanical, or/and hydraulic energy into electrical energy by deflecting  $\text{ZnO}$  nanowires in contact mode [19]. A nanogenerator is a device that harvests mechanical, vibrational, wind, water energy, and so on into electrical energy. In the last ten years, many research groups have fabricated NGs that could successfully convert mechanical, thermal, or vibrational energy into electrical energy via small-scale physical changes.

### **1.3.2 Energy Storage**

Energy storage is the technique for capturing the produced energy that could be used in future. The device, which has the capability to store the energy is known as battery or accumulator. There are various different types of energies, which could be stored by different types of storage devices such as Li-ion batteries, electro-chemical capacitors, super-capacitors, fuel cells, hydrogen storage and so on [20–24].

### **1.4 Nanogenerator**

In the past few years, efforts have been taken to develop nanogenerators for building self-charged systems. The working mechanism for nanogenerator significantly depends on various physical effects like the piezoelectric, pyroelectric, and triboelectric for scavenging mechanical or thermal energy. The various different types of nanogenerators based on these effects are shown in **Figure 1.3**.

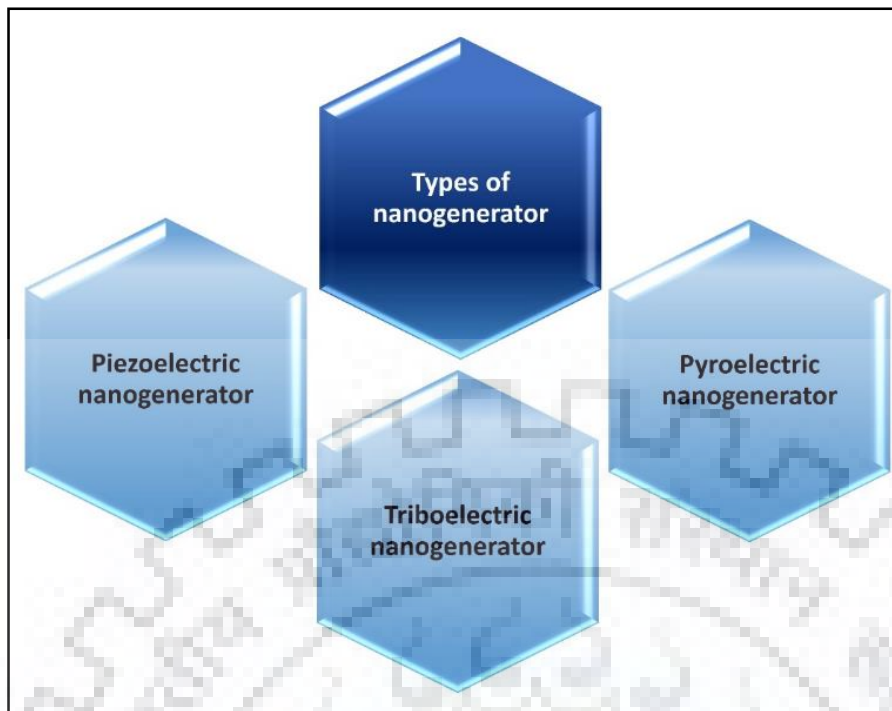


**Figure 1.3.** Different types of nanogenerators

#### 1.4.1 Piezoelectric effect

The electrical energy is generated from piezoelectric materials, when mechanical energy is applied to it, this effect is known as the piezoelectric effect (as illustrated in **Figure 1.4**). The nanogenerators based on piezoelectric effect are known as piezoelectric nanogenerators [3,25–33].

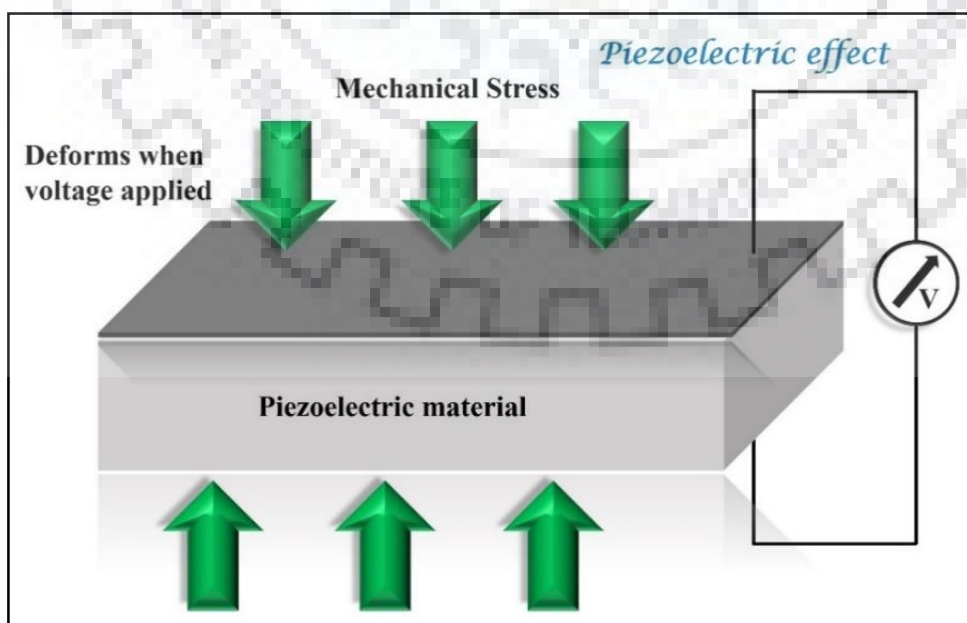


**Figure 1.4.** Mechanism behind piezoelectric nanogenerator

### 1.4.2 Pyroelectric effect

The nanogenerators (NGs) based on pyroelectric effects relies on the Seebeck effect i.e. exploits a temperature difference produced between the dissimilar electrodes for driving the dispersal of the charge carriers [34–43] as shown in **Figure 1.5**. In this effect, input is given in low operating frequencies with certain time intervals and get small power outputs.

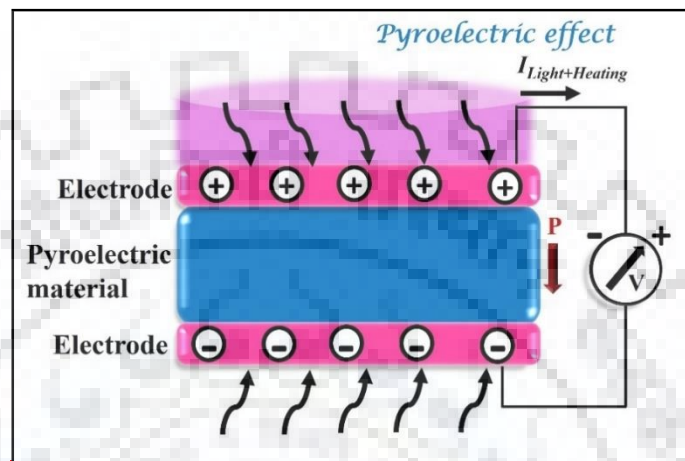




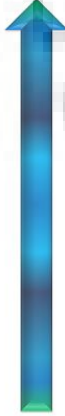

**Figure 1.5.** Mechanism behind pyroelectric nanogenerator

### 1.4.3 Triboelectric effect

Triboelectric charges refer to the charges generated on the surfaces of two dissimilar materials after contact, and these charges induce electric potential between the conductive electrodes when relative motion is made [44]. This induced potential drives the flow of mobile charges and current between the electrodes. The triboelectric charges are limited to the surface of the materials; they neither exterminate nor recombine. As soon as the materials are separated from each other, the material with large electronegativity will gain charge while the other with less electronegativity will lose charges, as shown in the triboelectric series (**Figure 1.6**) [45].

#### *Triboelectric series*

There are various nanomaterials presented with different unique optical, electrical, physical and chemical properties in the broad library of energy harvesting materials. Among these, some materials have the tendency to lose and gain the electrons. So, according to their such tendency, they are classified into tabular series with increasing/decreasing tribo-electronegativity known as triboelectric series, which is shown in Figure 1.6 [45,46].

<b>Positive</b> 	Aniline-formol resin	Polyvinyl alcohol	<b>Negative</b> 
	Polyformaldehyde 1.3-1.4	Polyester (Dacron) (PET)	
	Ethlcellulose	Polyisobutylene	
	Polyamide 11	Polyuretane flexible sponge	
	Polyamide 6-6	Polyethylene Terephthalate	
	Melanime formol	Polyvinyl butyral	
	Wool, knitted	Formo-phenolique,hardened	
	Silk,woven	Polychlorobutadiene	
	Polyethylene glycol succinate	Butadiene-acrylonitrile copolymer	
	Cellulose	Natural rubber	
	Cellulose acetate	Polyacrilonitrile	
	Polyethlene glycol adipate	Acrylonitrile-vinyl chloride	
	Polydiallyl phthalate	Polybisphenol carbonate	
	Cellulose sponge	Polychloroether	
	Cotton, woven	Polyvinyldine chloride (Saran)	
	Polyurethane elastomer	Poly(2,6-dimethyl polyphenyleneoxide)	
	Styrene-acrylonitrile copolymer	Polystyrene	
	Styrene-butadiene copolymer	Polyethylene	
	Wood	Polypropylene	
	Hard rubber	Polydiphenyl propane carbonate	
Acetate, Rayon	Polyimide (Kapton)		
Polymethyl methacrylate (Lucite)	Polyethyleen teraphtalate		
Polyvinyl alcohol	Polyvinyl Chloride (PVC)		
(continued)	Polyvinylidene fluoride (PVDF)		
	Polyterafluoroethylene (Teflon)		
<b>Positive</b> 	Polyformaldehyde 1.3-1.4	(continued)	<b>Negative</b> 
	Etylcellulose	Polyester (Dacron)	
	Polyamide 11	Polyisobutylene	
	Polyamide 6-6	Polyuretane flexible sponge	
	Melanime formal	Polyethylene Terephthalate	
	Wool, knitted	Polyvinyl butyral	
	Silk, Woven	Polychlorobutadiene	
	Aluminum	Natural rubber	
	Paper	Polyacrilonitrile	
	Cotton, woven	Acrylonitrile-vinyl chloride	
	Steel	Polybisphenol carbonate	
	Wood	Polychloroether	
	Hard rubber	Polyvinyldine chloride (Saran)	
	Nickel, copper	Polystyrene	
	Sulfur	Polyethylene	
	Brass, Silver	Polypropylene	
	Acetate, Rayon	Polyimide (Kapton)	
	Polymethyl methacrylate (Lucite)	Polyvinyl Chloride (PVC)	
	Polyvinyl alcohol	Polydimethylsiloxane (PDMS)	
	(continued)	Polyterafluoroethylene (Teflon)	

**Figure 1.6.** A list of triboelectric series containing materials according to their tendency to gain (negative) or loose electrons (positive) in frictional and contact charging process [45]

The electrostatic induction effect, which is used to generate electricity, has crucial improvement in the TENG working as depicted in **Figure 1.7**. The triboelectric charges are induced on the back side of the conductive electrodes. The induced charges on the back side of the electrodes provide mobile charges; when these two materials make a relative motion, they acquire opposite charges, as due to the consistent flow of induced charges electric potential that is created between these two electrodes. Therefore, mechanical energy is converted into electrical energy.

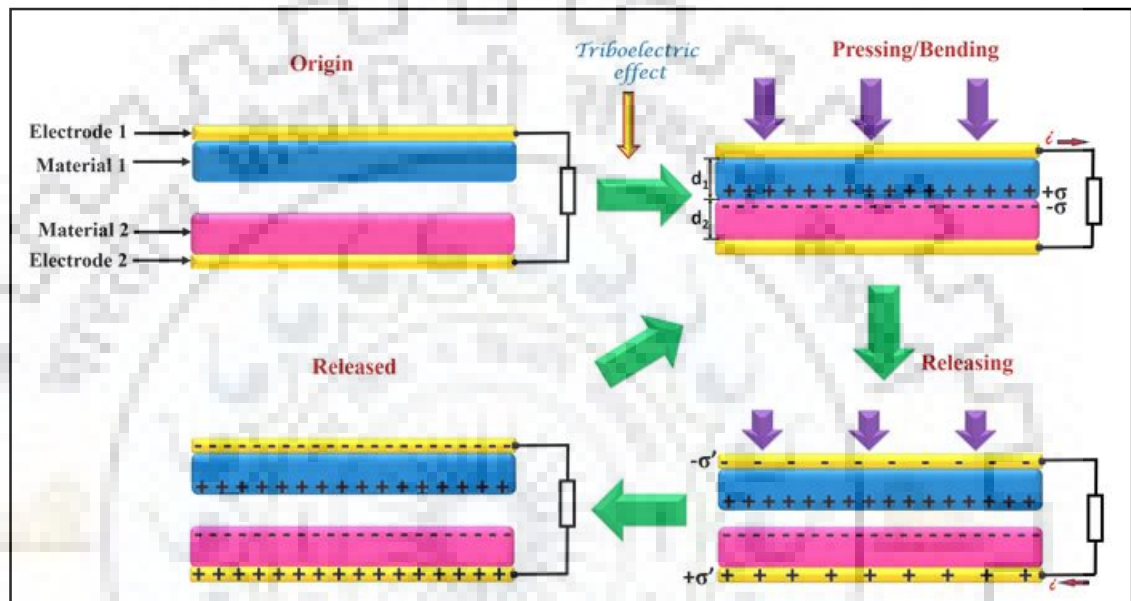


**Figure 1.7.** The working mechanism behind triboelectric nanogenerator

## 1.5 Triboelectric Nanogenerator

Due to the tribo-electric effect, the materials become electrically charged and acquire opposite charges on the surfaces. Foraging the mechanical energy produced from the environment via the triboelectric effect, has been confirmed to be cheap, simple, robust, and cost effective. The nanogenerators based on the triboelectric effect are known as triboelectric nanogenerators (TENG) [47,48]. In the past few years, efforts have been taken to develop nanogenerators for building self-charged systems. The working mechanism for TENGs significantly depends on the triboelectric effect for scavenging mechanical energy [49].

## 1.6 Various Operating Modes of TENGs

There are various forms of relative motion of the TENG to harvest mechanical energy are vertical contact mode [50–55], lateral sliding mode [56–66], single electrode mode [67–72] and free standing triboelectric layer mode [73–76] as shown in **Figure 1.8**.

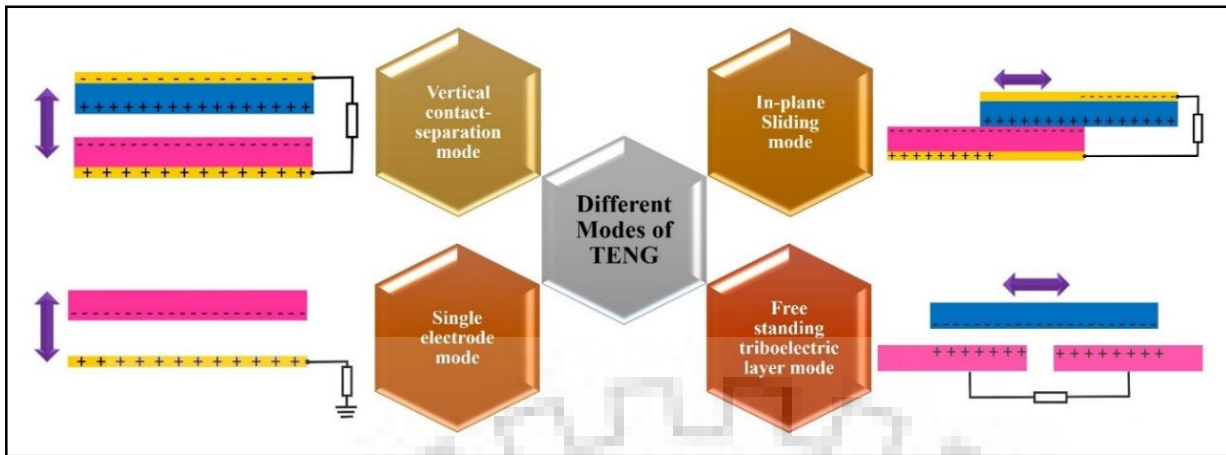


**Figure 1.8.** The diverse fundamental modes of TENG

### 1.6.1 Vertical contact-separation mode

In vertical contact separation mode, the motion of the charged surfaces in a TENG is perpendicular to each other. The vertical contact separation mode is used to harvest energy, which could be generated from engine vibration [50], finger typing [51], biomedical systems [52] and human walking [53–55].

### 1.6.2 In-plane sliding mode

The relative sliding motion between the two dielectric surfaces, can cause triboelectric charges to develop on their contact surfaces [56–60]. The horizontal polarization would be established along the sliding direction of the films, and thus the triboelectric charges are fully balanced with the flow of electrons among the electrodes. The movement of sliding apart and coming close would produce electrical outputs as voltage and current. The lateral sliding mode has been used to harvest energy, which could be generated from cylindrical rotation [61], disc rotation [34, 35], planar motions [28, 29, 36], hydropower [65], wind energy [66] and rotational kinetic energy [62].

### 1.6.3 Single electrode mode

The previously discussed two modes (vertical contact-separation mode and in-plane sliding mode) of TENGs must be attached with wire and an electrode. This type of device configuration restricts the applicability and versatility for harvesting energy from a random or a willingly moving object because the object must be mounted with an interconnector to the entire system and can work in mobile cases. To solve this problem, a single electrode mode of TENG has been reported [67–69], in which the bottom electrode is grounded. If the TENG has limited



size, the contact and separation of both the electrodes would alter the local electrical field distribution so the electrons would exchange between the ground and the bottom electrode to maintain the potential difference between the electrodes. The single electrode mode is used to harvest energy, which is generated from turning the book pages [70], air flow [71], rain drop [69], rotating tire [72] and so on.

#### **1.6.4 Free standing triboelectric layer mode**

When the moving object comes into contact with air or other objects, for instance when we walk on the floor, generally shoes become charged. The charges that are produced remain on the surface for many hours and at this moment friction or contact is unessential for this period because maximum charge density is already present on the surface. A pair of symmetric electrodes could be attached below the dielectric layer, gap distance and size of the electrodes are of same order as the magnitude of the moving object. The objects contact and/or separation from the electrodes would generate an asymmetric charge distribution in the media, due to which electrons would be able to flow among electrodes to equalize the local potential distribution [45, 46]. The power would be produced by the oscillations of the electrons among the paired electrodes. The top dielectric layer of the electrode should not come in contact directly with the moving object, so as to facilitate the free rotation, in rotation mode that could be possible without mechanical connection and the damage to the surfaces could also be radically abridged. While comparing with the previously studied single electrode mode, no screening effect [76] is observed in free-standing triboelectric mode, but transfer of electrons electrostatically-induced the same amount of triboelectric charges on the free standing layer. Compared with the in-plane sliding mode, there could be direct physical contact among the triboelectric surfaces but it will not affect the material surface and less amount of heat would be generated even for unremitting working [75].

Among these, this work is focused on Single Electrode mode and Vertical Contact Separation mode. The main aim of this work is to enhance the electronegativity of pristine polymer triboelectric material (PVDF) by incorporation of functionalized carbon derivatives (reduced graphene oxide nanoribbons (rGONRs), Fluorinated graphene nanoribbons (F-GNRs)) and analyse their effect on output performance. Electronegativity plays a key role to enhance the charge trapping phenomena. It has been revealed that the functionalized carbon based nanofillers such as graphene oxide, reduced graphene oxide, reduced graphene oxide nanoribbons, Fluorinated graphene nanoribbons, etc.) exhibited negative charge on their surface due to the presence of various electronegative groups such as oxygen containing functional groups such as

hydroxyl (-OH), carboxyl (-COOH), epoxy (C-O-C) group and fluorine functional group. Therefore, the amount of negative surface charge highly depends on the oxygen and Fluorine groups. When the oxygen and fluorine functionalized carbon based nanofillers are combined with the pristine polymer (tribo-negative material), then it increases the tribo-negativity of the resulting composite material, which will be a good impact for output performance of TENG.

Some research works have also been reported on graphene based TENG, in which graphene used as electrode materials for collecting the charges [77,78] . But in contrast, this thesis work is focused on functionalized carbon derivatives such as reduced graphene oxide nanoribbons and fluorinated graphene nanoribbons as fillers which were used to enhance the electronegativity of resulting polymer composite that leads to higher electrical output.

### **1.7 Applications of TENG**

Triboelectric nanogenerators currently have a wide range of applications in energy harvesting. It is well-known that these TENGs are advantageous as they do not need any kind of external power source to drive the load. These TENGs effectively harvest vibrational energy [50,79] to power small electronic devices and are sometimes used as an active vibration sensor. Human body motions have plentiful energy that could be harvested by the TENGs and used for charging small portable devices or in biomedical applications as shown in **Figure 1.9**.

For sensing the pressure applied, the principle of TENGs could be effectively used as an active self-powered pressure/force sensor [67,80–84] or vibration sensor [85,86]. TENGs could have potential applications in the fabrication of chemical sensors and biochemical sensors [87,88]. Effectively harvesting kinetic energy via a TENG for water splitting applications [89]. This principle could be used in a keyboard [90] that can detect, identify and record the signals in the system. By integrating TENG in the sole of a shoe, which can harvest the energy generated by walking and running [55,77]. The energy produced from the TENG is effectively stored in the attached Li-ion battery [91]. TENGs are also integrated with photovoltaic technology to form hybrid energy cell, which can harvest water energy as well as solar energy individually [92,93] even in harsh conditions. The conformal, graphene-based TENG can be integrated with human skin and can detect the touch of fingers and convert these touches into Morse code [78], that can be further used for communicating with the speech-impaired people. A LabVIEW-controlled voltage meter can effectively convert the signals into digital form and further transfer them to a mobile device. These are some of the applications where TENG could be effectively used and

there may be many more applications that could make use of the energy generated from TENGs [94].



**Figure 1.9.** Different types of energies harvested by TENGs and their applications in daily life

For sensing the pressure applied, the principle of TENGs could be effectively used as an active self-powered pressure/force sensor [67,80–84] or vibration sensor [85,86]. TENGs could have potential applications in the fabrication of chemical sensors and biochemical sensors [87,88]. Effectively harvesting kinetic energy via a TENG for water splitting applications [89]. This principle could be used in a keyboard [90] that can detect, identify and record the signals in the system. By integrating TENG in the sole of a shoe, which can harvest the energy generated by walking and running [55,77]. The energy produced from the TENG is effectively stored in the attached Li-ion battery [91]. TENGs are also integrated with photovoltaic technology to form hybrid energy cell, which can harvest water energy as well as solar energy individually [92,93] even in harsh conditions. The conformal, graphene-based TENG can be integrated with human skin and can detect the touch of fingers and convert these touches into Morse code [78], that can be further used for communicating with the speech-impaired people. A LabVIEW-controlled voltage meter can effectively convert the signals into digital form and further transfer them to a mobile device. These are some of the applications where TENG could be effectively used and

there may be many more applications that could make use of the energy generated from TENGs [94].

## 1.8 Objectives of Present Work

The main objectives of this research work are as follows:

- (i) To replace the pristine polymer, nanofillers incorporated with polymer will be used to enhance the charge trapping phenomena in triboelectric nanogenerator.
- (ii) The required nanocomposites will be used to increase the electro-negativity of resulting material.
- (iii) Different types of nanofillers (rGONRs, F-GNRs) with combination of the polymer will be studied to enhance the performance.
- (iv) To fabricate the TENGs using above selected materials and analyse the generated electrical outputs with the satisfactory level.

## 1.9 Organization of the Thesis

The work presented in this dissertation is planned to fabricate energy harvester by using carbon based nanofillers. The dissertation comprises six chapters, which includes the background of the nanogenerators, motivation of the present work and focuses on the research activities. In this section, the content of different chapters are briefly discussed.

**Chapter-1:** The chapter named “**Introduction**” includes brief introduction about the energy, various energy harvesting and energy storage techniques. Subsequently, various effects on which the nanogenerator work is discussed and then, triboelectric nanogenerator with its various modes of operations have been briefly discussed. Later on, the objectives of the present work are defined. Finally, the organization of the thesis is incorporated in this chapter.

**Chapter-2:** The chapter named “**Literature Review**” includes the brief study of the various modes of TENGs, which had been fabricated using different materials with diverse applications. Comparative study of the TENG was also discussed. The research gaps that are present in the literature has been identified. The planning of research has been prepared and discussed in this chapter.

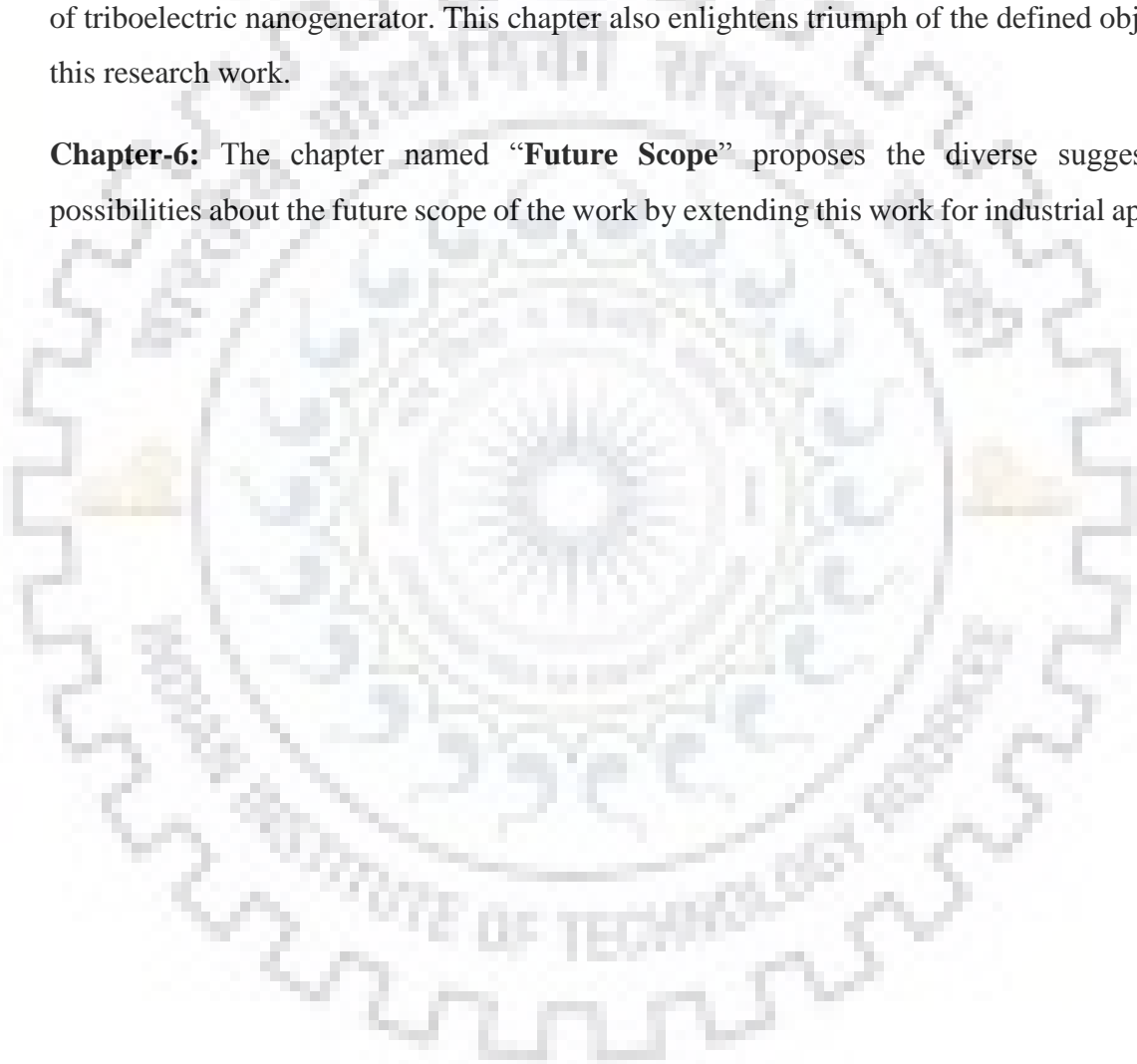
**Chapter-3:** The chapter named “**Experimental Details**” includes the list of chemicals and materials used, methods for the synthesis of rGONRs and functionalized GNRs. Here, we also

discussed the different characterization techniques, which are used for analysis of synthesized materials as well as for the fabricated nanogenerator.

**Chapter-4:** The chapter named “**Results and Discussion**” contains the results acquired from different characterization techniques. The discussions, which are related with the synthesis of the nanomaterials, their modifications and further used them in the fabrication of nanogenerator.

**Chapter-5:** The chapter named “**Summary and Conclusions**” provides the research summary and conclusions drawn from the present work with the key findings and progresses in the field of triboelectric nanogenerator. This chapter also enlightens triumph of the defined objectives for this research work.

**Chapter-6:** The chapter named “**Future Scope**” proposes the diverse suggestions and possibilities about the future scope of the work by extending this work for industrial applications.







## Chapter 2

### LITERATURE REVIEW

---





Energy is the essential requirement of daily life. Due to the diminution of the energy sources, it is necessary to develop devices that can harvest the unused/wasted energy that exists in the ambient environment. In this regard, triboelectric nanogenerators (TENGs) have been developed as an innovative paradigm for energy harvesting. They can harvest the various forms of mechanical energy, including vibrations, ocean waves, human motion, rain drops, flowing water, the motion of an automobile, wind, rotational energy, and mechanical triggering. TENGs can combine the contact electrification and electrostatic induction for energy conversion. It operates on four fundamental modes for conversion of mechanical energy into electrical energy to power small-scale electronic devices such as mobile phones, mp3 players, smart watches, sensors and etc. [80,78,95–190]. The electrical outputs obtained from TENGs depend on the friction of materials, where materials are selected from the triboelectric series on the basis of their electronegativity and electropositivity.

For choosing the objectives of the present research work and identifying the research gaps, the literature review has been carried out on the two basic modes of operations. And, also a broad study of the various modes of triboelectric nanogenerators has been done. The various nano-materials mainly polymers with different morphologies, which are used for fabrication of the TENG have also been discussed.

## **2.1 Modes of operation**

Our research work is focused on two modes i.e. vertical contact separation mode and single electrode mode.

### **2.1.1 Vertical contact separation mode**

In vertical contact separation mode, the motion of the charged surfaces in a TENG is perpendicular to each other. The vertical contact separation mode could be used to harvest energy, which was generated from engine vibration [50], finger typing [51], biomedical systems [52] and human walking [53–55]. In 2012, Fan and co-workers first demonstrated the flexible TENG [47] by piling polyester (PET) and kapton thin films on one another through mechanical deformation. The electrical outputs are found to be  $\sim 10.4 \text{ mW cm}^{-3}$ ,  $0.6 \mu\text{A}$  and  $3.3 \text{ V}$  for the peak power density, short-circuit current and open-circuit voltage, respectively.

Thereafter, Zhu *et al.* published a clear and accurate explanation of the nanogenerator based on the energy generation process [191]. They demonstrated a TENG in which poly(methylmethacrylate) (PMMA) and kapton were used as the two materials with charges

generated on them. When the external force is applied, both the materials gain charges due to triboelectric effect [192–194]. As PMMA polymer is higher in triboelectric series, it loses electrons and gains positive charge while the kapton surface gains electrons from PMMA and it acquires a negative charge. When external force is released, an electric potential difference is generated among the electrodes. The electric potential difference calculated using Equation (2.1) and expressed as:

$$V_{OC} = \frac{\sigma d}{\epsilon_0} \quad (2.1)$$

Where,  $V_{OC}$  is the open-circuit voltage,  $\epsilon_0$  is the vacuum permittivity and  $\sigma$  and  $d$  are triboelectric charge density and gap distance between the two materials, respectively. As the PMMA layer returns to its original position, the open-circuit voltage is reduced and becomes zero when the complete contact is in equilibrium. This phenomena states that  $V_{OC}$  depends on the comparative position of both the charged layers. If the two charged layers have become still, then  $V_{OC}$  will be neutralised.

The induced charge density ( $\sigma'$ ) can be calculated by using Equation (2.2) and is expressed as follows:

$$\sigma' = \frac{\sigma d \epsilon_{rk} \epsilon_{rp}}{d_1 \epsilon_{rp} + d \epsilon_{rk} \epsilon_{rp} + d_1 \epsilon_{rk}} \quad (2.2)$$

Where  $d_1$  and  $d_2$  are the thickness of the PMMA layer and the kapton film, respectively,  $\epsilon_{rp}$  and  $\epsilon_{rk}$  are relative permittivities of PMMA and kapton film, respectively. The flow of induced charges then forms the output current having direction depending upon the mechanical motion i.e. pressed or released. Therefore, the reciprocating motion produces alternating current. The maximum open-circuit voltage was found to be 110 V with  $31.2 \text{ mW cm}^{-3}$  as the highest instantaneous electric power density.

Wang and co-workers used contact electrification technique based on polymer-metal electrodes to generate electrical output between an Al metal foil and PDMS polymer thin film for fabricating an arc-shaped TENG [195]. For the top electrode, a layer of  $\text{SiO}_2$  film (500 nm) is coated through plasma-enhanced chemical vapour deposition (PECVD) at  $250 \text{ }^\circ\text{C}$  on top of a flat kapton film. Then, the patterned PDMS layer is fixed on the other side of kapton using a PDMS bonding layer and on the top of  $\text{SiO}_2$  layer, and an electrode is fixed. For the lower plate, Al is patterned using a photolithography technique, which acts as both electrode as well as contact surface. Finally, both the fabricated plates of equal size are attached head-on and the ends

are sealed. To create the gap between the plates, the soft Al plate is forced to bend outward under the shrinkage from the other plate. To realize the TENG, a compressive cycled force is applied onto the entire area ( $3 \text{ cm} \times 2.8 \text{ cm}$ ) of the device, so that the bending plates are flattened and come in contact with each other. Due to stored elastic energy, both the plates are separated from each other and then, due to resilience, they return to their original shape. The electrical outputs for the as-fabricated TENG reach  $94 \mu\text{A}$  for the short circuit current ( $I_{SC}$ ) and  $230 \text{ V}$  of  $V_{OC}$ . Furthermore, the experiment was performed numerically by using COMSOL Package. The TENG was tested at nine different frequencies (2 to 10 Hz) and it was found that  $V_{OC}$  remained same, as the amplitude of the triggering motor also remains constant. On the other hand, when frequency increased (2 to 10 Hz),  $I_{SC}$  rose from  $35$  to  $130 \mu\text{A}$  respectively. The obtained current and voltage reached  $0.13 \text{ mA}$  and  $230 \text{ V}$ , respectively with the maximum instantaneous power densities of  $3.56 \text{ mW cm}^{-2}$  and  $128 \text{ mW cm}^{-3}$  (entire volume of the device) [195].

An arch-shaped flexible TENG, which works on the principle of contact-separation and harvest irregular mechanical energy, developed by Zhong and his colleagues [51] using polytetrafluoroethylene (PTFE) and polyvinyl alcohol (PVA) nanofiber coated with silver (Ag) thin film; both would act as triboelectric materials. A thin layer of Cu film ( $200 \text{ nm}$ ) as a top electrode and is coated on  $3.5 \text{ cm} \times 2.5 \text{ cm}$  of PTFE film using a sputter coating technique. For the bottom electrode,  $3.5 \text{ cm} \times 2.2 \text{ cm}$  of polyethylene glycol terephthalate (PET) film of thickness  $0.22 \text{ mm}$  was deposited. Further, a layer of PVA nanowires was mounted on top of PET film and a thin film of Ag ( $100 \text{ nm}$  thick) was deposited using sputter coating. While assembling the arch-shaped TENG, the PTFE film was facing an Ag thin film and the edge along the length of both the films were fixed using kapton tape. The output concert of the TENG would be determined by many factors, such as: varying the frequency, spacer distance and load resistance. The authors measured the output current by connecting the two TENGs in parallel and in antiparallel, and found that the current increases and decreases, respectively, with an external load of  $500 \text{ M}\Omega$ . At  $3 \text{ Hz}$  frequency, it was found that with increase in deformation, the current increases from  $0.25 \text{ mA}$  at  $0.5 \text{ mm}$  to  $0.72 \text{ mA}$  at  $2 \text{ mm}$ . Moreover, the total number of charges transferred also increases with increase in distance between the electrodes. While increasing the load resistance, current decreases but voltage increases up to  $407 \text{ V}$  with output electrical power of  $0.23 \text{ mW}$  at  $300 \text{ M}\Omega$  load resistance. Moreover, the TENG was demonstrated by powering the  $50$  light-emitting diodes (LEDs) connected in series [51].

The simple structure for a TENG was demonstrated by Zhu and co-workers; it was based on contact separation mode with polydimethylsiloxane (PDMS) as the polymer and gold (Au) as

a metal thin film [196]. The fabricated TENG consisted of two substrates in the form of layers. In the fabrication process, PMMA material was selected as the substrate for both sides of the TENG. For the lower part, a thin film of Au was deposited on top of substrate and it played a dual role, i.e., it act as an electrode as well as a contact triboelectric-surface. Au nanoparticles were coated on the surface. A thin layer of Au was deposited on the substrate and then a layer of PDMS was coated and act as other triboelectric-material for the TENG. Both the prepared substrates were assembled with the four springs mounted at the corners, maintaining a small gap among the PDMS and the contact electrode (Au). The spring provided a restoring force that enabled continuous contact-separation between both portions, which are under external impact. The TENG generates current pulses that are triggered by the human footfalls, and resulting in 2 mA as a current output. This could immediately light up 600 LEDs, as all the LEDs are serially connected.

The 3D spiral structure integrated with vertical contact-separation TENG is explored by Hu *et al.* for harvesting the vibration energy [197]. The authors used an acrylic sheet as a substrate material and on them, two round plates were attached; one was mounted at the lower side of the 3D spiral structure and other was attached to the upper part of the cube's surface. For one side of TENG, an Al film was deposited on an anodic aluminium oxide (AAO) template, which acts as one of the triboelectric surfaces. The nanopores were uniformly distributed on the Al surface, which increased the effective surface area for triboelectrification with average diameter of 30 nm. On the other hand, a kapton film, modified with aligned nanowire structure and uniformly dispersed on the surface, which was further enhance the surface roughness. With the spiral oscillates, when both the materials come in contact with each other, electrons moved from Al film to the kapton film and acquired positive and negative charges, respectively. The flow of electrons stops when the distance of separation is maximized, and hence achieves an electrostatic equilibrium. Therefore, electricity would be generated by the mechanical disturbance in the spiral oscillates. The  $I_{SC}$  and  $V_{OC}$  can be calculated by using Equations (2.4) and (2.5), respectively, as follows:

$$I_{SC} = \frac{-S\sigma d}{\epsilon_r \left( \frac{d}{\epsilon_r} + x(t) \right)} \frac{dx(t)}{dt} \quad (2.4)$$

$$V_{OC} = - \frac{\sigma x(t)}{\epsilon_0} \quad (2.5)$$

Where,  $\sigma$  and  $S$  are defined as the charge density and area around the plate, respectively,  $x(t)$  is the separation between Al and kapton films,  $d$  is the thickness of kapton film, and  $\epsilon_r$  and  $\epsilon_0$  are

the relative dielectric constant of the kapton film and dielectric constant of the vacuum, respectively. However, when there is a small disturbance in the water, the obtained current and voltage is reached to 15  $\mu\text{A}$  and 110 V, respectively and could light up to 20 LEDs.

For harvesting common mechanical motions, i.e., vibrations, into electrical energy, a TENG was demonstrated by Chen *et al.* [50]. The harmonic-resonator-based TENG had a multilayered structure in which a PMMA sheet would act as the substrate material due to its low cost, good strength, decent machinability, and light weight. On top of the upper substrate, film of aluminium (Al) with a nanoporous surface would act as an electrode as well as the contact surface. A polytetrafluoroethylene (PTFE) film was deposited onto the bottom substrate with copper as another electrode. The nanowire array of PTFE was fabricated onto the PTFE surface by reactive ion etching via a top-down approach. The average length and diameter of PTFE nanowires were observed to be  $1.5\pm 0.5 \mu\text{m}$  and  $54\pm 3 \text{ nm}$ , respectively. Initially, the PTFE layer comes in contact with the thin film of Al, the positive charges are developed on the Al surface, and the PTFE surface acquires more negative triboelectric charges than Al. Therefore, electrons are injected from Al into PTFE, producing positive charges on the Al surface. To examine the performance of the harmonic-vibration-based TENG, an electrodynamic shaker was attached that delivers a sinusoidal wave, which was further used for tunable amplitude and frequency as a vibration source. The obtained  $I_{SC}$  and  $V_{OC}$  were found to be  $76.8 \mu\text{A}$  and  $287.4 \text{ V}$ , respectively, representing the resonance frequency of the TENG to be 14.5 Hz by considering a single degree of freedom vibrating system; the natural frequency is given by:

$$f_o = \frac{1}{2\pi} \sqrt{\frac{4k}{m_o}} \quad (2.6)$$

Where  $f_o$  is the natural frequency and  $k$  and  $m_o$  are the stiffness coefficient and mass of the upper substrate plus the Al film, respectively. For the harmonic vibration based TENG,  $k$  is  $112 \text{ N m}^{-1}$  and  $m_o$  was  $56.8 \text{ g}$ . Substituting these values in Equation (2.6), they find the natural frequency ( $f_o$ ) to be 14.1 Hz, which is comparable to the experimental result. The peak power is maximized, when the load resistance of  $5 \text{ M}\Omega$  was attached, which provides a peak power density of  $726.1 \text{ mW m}^{-2}$ .

Yang's group has successfully fabricated an integrated rhombic gridding based TENG [53] for enhancing the total electrical output by connecting unit cells in parallel. For the fabrication of the TENG, a PET plastic sheet with  $600 \mu\text{m}$  thickness was used. An Al thin film with nanoporous modifications was deposited on one side and it had dual functionality to act as a contact electrode and as a contact surface. On the other side, the Cu film was coated to act as a

back electrode and adhered with a layer of PTFE nanowire arrays. This rhombic gridding structure of TENG had parallel unit cells, which were electrically connected to improve the current output. Moreover, the effective contact area of TENG increased because of the structural coupling of PTFE nanowires arrays and aluminium nanopores. There are various factors on which the  $I_{SC}$  highly depends: relative velocity of separation or contact between the two plates, effective contact area, and charge density. First,  $\sigma$  is mainly affected by the difference in charge affinities of both the contact materials. From all of these materials, PTFE has more electronegative with the charge affinity of  $-190 \text{ nC J}^{-1}$  and being an electropositive material, aluminium has a charge affinity of  $10\text{-}30 \text{ nC J}^{-1}$  [141, 142]. Therefore, the large difference in charge affinity would generate a large number of triboelectric charges and hence higher amount of electric output would be given by the device. Second, surface modification of nanomaterials is also significantly enhanced the effective surface areas. The electrical outputs ( $V_{OC}$  and  $I_{SC}$ ) with peak values of 428 V and 1.395 mA, respectively at  $n = 3$  with  $30.7 \text{ W m}^{-2}$  as a peak power density. The electrical outputs depend on the value of  $n$  and are nearly constant for all the measurements, because rhombic unit cells are connected in parallel.

The instantaneous discharge (ID) TENG was fabricated by Cheng group [199]; they choose PMMA plates to build the device and Au thin film that act as the metal electrodes was deposited on the PMMA plates. For fabrication of TENG, two contact materials were selected: PDMS and  $\text{SiO}_2$  nanoparticles to act as contact materials for the lower and upper electrodes, respectively. The peak values of  $I_{SC}$  and  $V_{OC}$  were found to be  $264 \mu\text{A}$  and 285 V, respectively. Cheng and co-workers also fabricated an ID-TENGs in both in-plane sliding and rotating disk mode. The obtained instantaneous current,  $V_{OC}$  and power are found to be 57.5 mA, 115 V, and 3.3 W, respectively. When the rotating speed of the ID-TENG was increased from 10 to 400 rpm (rounds per minute), the current peaks remained  $\sim 5.2 \mu\text{A}$ , which confirmed that the speed of contact and separation among the triboelectric surfaces does not clout the current. The instantaneously maximum current peaks in the vertical contact-separation mode of ID-TENG was found to be 0.53 A, which is 5 times higher than a continuous discharging (CD)-TENG and the current density was estimated to be about  $1325 \text{ A m}^{-2}$ . The instantaneously maximum power and power density of ID-TENG were observed to be 142 W and  $3.6 \times 10^5 \text{ W m}^{-2}$ , respectively. When they combine both the vertical contact-separation and rotating disk mode of ID-TENG, the electrical output density peaks (power density and current density) were found to be  $1.4 \times 10^4 \text{ W m}^{-2}$  and  $104 \text{ A m}^{-2}$ , respectively at frequency 106.7 Hz.

Hou and co-workers used PDMS and PET as two triboelectric materials for fabricating the contact-separation mode based TENG [55]. It was observed that the spacer plays a significant role in separating both the materials for working of TENG. The authors focused on the optimization of the best spacer, which includes thickness, number, area coverage, and fabric. three different materials, that is, sports socks, T-shirt, and polyurethane (sponge), which were used as the spacer materials and it was found that the sponge spacer based TENG had better performance and showed good electric outputs, that is, the  $V_{OC}$  and short-circuit current density produced from them. They also observed the effect by increasing or decreasing the number of spacers on the output of the TENG. As the number of spacers increased, the effective contact triboelectric surface decreased and hence the output performance, that is, current density and voltage, decreased. The third parameter that was considered by the authors was the thickness of the spacers. It was found that highest peak values of voltage and current density were 135 V and  $0.8 \text{ mA cm}^{-2}$  at 3 mm thickness of spacers. The last parameter that was considered by the authors was the working frequencies, which were varied from 4 to 8 Hz. They found that as the frequency increased, the strain rate increased and as a result there was higher current output, but the charges induced on the surfaces had a constant value. By considering all the optimized parameters, the authors analyzed the output performance of the shoe insole by stepping on the top of the device and found that the current density and voltage were  $0.8 \text{ mA cm}^{-2}$  and 220 V, respectively. Furthermore, they investigated the effect of external load on the working of TENG by changing the resistor from  $10^3 - 10^8 \Omega$  and analyzed that as the load resistance increased, current decreased but voltage increased. The instantaneous maximum power value obtained was nearly 1.4 mW. The electrical outputs were estimated to be 3.0 – 3.4 V, 24 mA max, and 27,000 mcd. Moreover, TENG-based shoe insole can light up 30 white LEDs connected in series.

Zhang *et al.* have been demonstrated a TENG [200], that can detect the humidity or alcohol content in liquid as well as in gaseous phase. It was made up of a PTFE film and polyamide 6,6 (PA) film. Here, one of the electrodes was a PA thin film deposited on a copper foil, as a back electrode, and the other was a nanopore modified Al foil after deposition as the contact electrode. Therefore, according to triboelectric series, Al foil and PA film have different abilities to attract and give electrons, which results in desirable outputs [198]. There was uniform dissemination of nanopores on the Al foil surface after etching, which contained  $\text{Al}_2\text{O}_3$ . However, a thin layer of Al was deposited on it using a pulsed vapour deposition (PVD) technique to make the surface conductive after etching. The nanopore-based morphology still remained after coating the thin film and hence it helped to improve the output concert of the TENG [201]. The TENG performance was measured by using Al foil without nanopores and it was found that the output

performance increased, when using etched Al foils as electrodes. Then, the performance was measured by changing the polymers thin films, i.e., with a PTFE film and with a PA film. When using PTFE thin film, it showed opposite signals for current as well as voltage, as that of PA-TENG with same connections. This happened because of the positions of PTFE, PA, and Al in the triboelectric series; PTFE film has a greater tendency to gain electrons from the Al foil and acquire negative charge, while the PA thin film has the tendency to lose electrons to Al and acquire a positive charge. When a drop of water or ethanol was distributed on the bottom electrode of PA-TENG, the output signal decreases to zero; this implies that the TENG was used as an active sensor for detecting liquid ethanol/water, but PTFE-TENG was used only as a sensor for the detection of liquid ethanol. The principle on which the active sensors work is illustrated by considering the degree of wettability of the solid polymer surface through identifying the contact angle to ethanol and water. This TENG could be used as a self-powered active sensor for industrial manufacturing and environmental monitoring with various advantages including low cost, easy fabrication, and good performance.

A TENG was demonstrated by Fan's group in which indium tin oxide (ITO)-coated PET coated on PET film was used as a substrate material for PDMS structure [202]. The ITO-coated PET substrate act as a collector as well as an electrode. The cross linker and liquid PDMS elastomer were uniformly distributed on the insulating surface by spin coating. After thermal treatment, a uniform PDMS layer of thickness 50 to 100 nm was on the PET surface. Finally, to fabricate the device, the as prepared bilayer structure of the ITO-coated PET film was used to make a sandwich-structured device. The ITO electrode and PDMS surface were placed opposite to each other, leaving a slight gap between the two contact surfaces forming an arched structure. This arched structure was used to significantly enhance the output performance of the TENG. The electrical output performance of the transparent TENG with a size of 3 cm × 3 cm in terms of  $I_{SC}$  and  $V_{OC}$  were measured to be 7  $\mu\text{A}$  and 200 V, respectively, and it had a current density of 0.78  $\mu\text{A cm}^{-2}$  at load resistance of  $\sim 30 \text{ M}\Omega$ , which gives electrical power up to 0.45 mW. In order to avoid the inherent light scattering problem in the patterned surface, a full device was prepared using the flat PDMS film, which shows  $\sim 78\%$  transmittance. The authors also studied the influence of the ambient environment and surface modification on the performance. When the PDMS surface came in contact with UV-ozone, it became charged. Furthermore, the performance of TENG was measured in the ambient environment which contains oxygen and water as well as in argon environment and it was found that the output performance was much higher in the ambient environment. The tribo-charge generation observed was possibly caused by the bond



breaking of Si-O-Si polymers chains of PDMS; it also attributed to the surface properties and the ambient environment.

In 2015, Li and co-workers reported a cylindrical spiral TENG, in which Cu, PET, kapton, and Al were used [203]. All the layers were stacked layer-by-layer, curled up, and annealed in an oven at 70 °C to keep the layered structure. In this structure, kapton acts as the triboelectric friction material, Cu acts as an electrode, PET worked as an insulator, and Al performed a dual role as an electrode as well as a triboelectric material. Al and kapton are two triboelectric friction materials because of the high electrification when they contact each other. Al is more triboelectrically positive than kapton and hence acquires positive charge on the surface, while kapton have an equal amount of negative charge on the surface. Due to electrostatic equilibrium, there is no charge flowing in the external circuit, but when both the surfaces start to separate from each other, an electrical potential drop develops and provides an electrical output. When Al and kapton are completely separated from each other, another electrostatic equilibrium is reached by transferring all the positive charges to the Cu electrode. At the maximum speed and symmetric acceleration of  $2 \text{ m s}^{-1}$  and  $25 \text{ m s}^{-2}$ , the  $I_{SC}$  and  $V_{OC}$  were found to be  $15 \mu\text{A}$  and  $30 \text{ V}$ , respectively. Furthermore, the Spiral TENG was combined with a transparent and flexible PET film having a large area (hand-driven curly TENG). When the TENG was driven manually, both the films Al and kapton experience relative motion and come in contact with each other. When they were released, they moved in opposite direction and return to the initial curved state. Thus, the electrical outputs generated during the cyclic movement of the TENG were observed as  $250 \text{ V}$ ,  $20 \mu\text{A}$  and  $2.5 \mu\text{C}$  for  $V_{OC}$ ,  $I_{SC}$  and transferred charge quantity ( $\Delta Q$ ), respectively. This hand driven TENGs output was verified by lighting up 100 red LEDs simultaneously. Moreover, the Spiral-TENG was used in the measuring tapeline, which is commonly used in our daily life. Li *et al.* also used the same dimensions i.e.  $15 \text{ mm} \times 180 \text{ mm}$ , with same friction materials. When the films were pulled out, the electrical output was generated, which was further used to power an external screen for displaying the corresponding screen.

TENGs were usually fabricated using bio-incompatible materials and therefore have a limited use in biomedical fields. In this regard, Sun *et al.* demonstrated TENG [204] using biocompatible polymers, i.e., ethyl cellulose (EC) and poly-L-lactic acid (PLLA); this is so-called biomedical TENG. The TENG was fabricated in the arc-shaped structure and by coupling the triboelectrification and electrostatic induction to effectively accumulate charges. When both the triboelectric films come into contact with each other, by applying external forces, they generate opposite and equal tribo-charges. Because of the strong tendency of PLLA to acquire

negative charges by gaining electrons from EC, positive tribo-charges are left on the EC surface. Due to the insulating behavior of the surfaces, the triboelectric charges would be conserved on their surfaces. Further, the authors selected different biocompatibility materials, i.e., kapton, PLLA, and EC, as the friction materials. The electric outputs, i.e.,  $V_{OC}$  and  $I_{SC}$ , of EC-kapton were found to be 302.4 V and 16.7  $\mu A$ , which was greater than that of EC-PLLA 260.5 V and 12.3  $\mu A$ , respectively. Moreover, the authors tuned the thickness of the EC film from 200 to 380  $\mu m$  and further to 440  $\mu m$  and found that output voltage and current first increases and then decreases. The same trend was observed in the EC-kapton TENG. When the thickness of PLLA and EC films were 320 and 380  $\mu m$ , the maximum electrical output measurements were observed to be 310.5 V and 16.2  $\mu A$ , respectively. Furthermore, the authors demonstrated the TENG by driving several LEDs without using any rectification. Sun *et al.* also demonstrated the biomedical application of TENGs for the growth of cells by using EC and PLLA polymers. The survival rate of L929 cells of mice was stimulated by the TENG and found to be higher than that of the negatively controlled test. Furthermore, the TENG was used in the biomedical field for healing the wound and increasing the cell growth in the human body.

Ye and co-workers fabricated a TENG using kapton and polymer (poly(vinylidene fluoride-co-hexafluoropropylene), P(VDF-HFP)) layers [205]. When both layers come in contact with each other through compressive forces, charge transfer takes place between the layers; kapton which has a sturdy negative triboelectric polarity acquires negative charges and P(VDF-HFP) acquires positive charges. They investigated that the effect of surface morphology of triboelectric layer on performance of the TENG using a spin-coated P(VDF-HFP) film with ion gel P(VDF-HFP) nanofibers structure. It was observed that there was higher output in the device made up from ion gel nanofibers. For fabricating the TENG, the authors used a kapton coated Al film and Al foil as the top and bottom electrodes, respectively. On the other hand, an ion gel nanofiber mat was electrospun. The ion gel nanofibers were synthesized using diverse ionic concentrations (0, 2, 5 and 10 wt%). The diameter of nanofibers was increased with the concentration of ionic liquid, which exhibits more induction charges on the surface. The output was estimated under the force of 50 N and 5 Hz as applied frequency. The electrical outputs (current density and voltage) were observed to be 49  $\mu A cm^{-2}$  and 45 V, respectively, from the ion gel based TENG, which is higher than pristine P(VDF-HFP) based TENG (19  $\mu A cm^{-2}$  and 20 V), at 50 N compressive force. In addition, the authors observed that TENG has good stability and could light up to 15 LEDs without using any rectifier. Moreover, the TENG had many applications for powering the self-powered electronic systems and portable devices.

To improve the efficiency and electrical outputs of TENGs, Yun and co-workers fabricated a TENG [206] with base (NaOH) as surface treatment of PDMS polymer. They selected ITO as the electrode; a film of PDMS sprinkled NaOH was deposited on an ITO coated PET substrate as one electrode and ITO-coated PET as another electrode. The electrical concert i.e. output voltage, current, and charge were investigated for the bare polydimethylsiloxane (PDMS), ultraviolet-ozone (UVO) irradiated and PDMS treated with NaOH-based TENGs. During the contact-separation of the TENGs, the authors observed that surface-treated PDMS-based TENG had significantly improved electrical outputs. While comparing with the bare PDMS-based TENG and UVO-irradiated PDMS-based TENG, output voltage, current, and charge density for the NaOH-treated PDMS-based TENG were observed to be 49.3 V, 1.2  $\mu\text{A}$ , and 185.7  $\text{nA cm}^{-2}$ , respectively, and it was quite stable for at least 20,000 cycles for contact/separation. The electrical outputs increased due to the presence of Si-O bonds in the UVO-treated and NaOH-sprinkled PDMS-based TENG, whereas these Si-O bonds were not present in the fresh PDMS and were less present in the UVO-treated PDMS based TENG. These surface-treated TENGs are cost-effective, suitable for large area and used for high-power TENG applications.

Later in 2015, Huang's group introduced book shaped-TENG [207] with poly(3-hydroxybutyrate-co-3-hydroxyvalerate) (PHBV), PVDF nanofibers and PET polymer that act as a substrate material. Initially, they prepared graphene oxide (GO) and PVDF composite, which was then used for fabrication of nanofibers as one of the triboelectric materials. GO amended the surface electrification of the PVDF polymer, improving the output of the fabricated TENG. When both the triboelectric surfaces came into contact with each other, PHBV being electropositive material and PVDF being electronegative, they acquired a positive and negative charges, respectively, and hence possessed large potential difference. At a frequency of 1.8 Hz, the obtained  $V_{OC}$  and  $I_{SC}$  of the TENG made up from pure PVDF and PHBV nanofibers were observed to be 190 V and 27  $\mu\text{A}$ , respectively. When a small amount of GO (0.1%) was incorporated in the PVDF matrix, then, sharp increment in the outputs were observed to be 260 V and 55  $\mu\text{A}$ , respectively. As the concentration of GO increased in the prepared sample, electrical outputs increased and the average diameter of the PVDF nanofibers was reduced. Moreover, the highest electrical outputs (voltage and current) for 0.7% GO in the PVDF and PHBV nanofibers based TENG were observed to be 340 V and 78  $\mu\text{A}$ , respectively, and it was quite stable up to 18,000 contact separation cycles. The charge and energy generated from the PVDF/GO and PHBV nanofibers were 431.3  $\mu\text{C}$  and 42.3 mJ, respectively. Furthermore, the authors demonstrated the practicability of the book shaped-TENG by powering 113 serially

connected LEDs and driving small electronic devices. Using the composite materials would open up new possibilities for the triboelectric materials used in TENG.

Extending the concept of harvesting energy, Chen *et al.* fabricated TENG [208] that floats on a water surface and can effectively convert the energy generated from random, slow, and high-force oscillatory waves into electrical energy. An acrylic sheet was selected as the supporting material. On the top and bottom of the acrylic sheet, Al thin film with nanoporous structure and dual functionality (an electrode and a contact surface) was deposited between the nanowire structures of PTFE. Between the PET substrate and PTFE, there was one more layer, which was made up of Cu. When the surfaces come in contact with each other, PTFE is the more negative triboelectric surface and acquires negative charge while Al acquires positive charge; the electrons eject from Al and are gained by the PTFE surface. To measure the electrical outputs as voltage and current of the single unit, a metal ball of 160 g was triggered in between the centre of the top plate of the TENG at an acceleration of  $10 \text{ m s}^{-2}$ , outputs were observed to be 569.9 V and 0.93 mA, respectively. A power density of  $0.26 \text{ mW cm}^{-2}$  was observed, corresponding to the maximum load resistance of  $1 \text{ M}\Omega$ . As the number of TENG units were increased from 1 to 4, the current and power density increased while voltage remains constant. Further, the output was verified by COMSOL Multiphysics. The average power output in an ocean area of  $1 \text{ km}^2$  was expected to be 1.15 MW from a networked TENG. For a practical demonstration of the work, the authors connected four TENG units in parallel and they were made to float on the water surface of a swimming pool. An ocean emergency system had driven with the networked TENG, which was operated by a gentle wave. This TENG could be integrated with various kinds of energies to harvest energy.

For harvesting the natural vibrational energy, Zhang and colleagues fabricated a porous micro-nickel foam (PMNF) based TENG [209]. PMNF performed dual role as an electrode and as a contact surface, while Al acts as the back electrode and PDMS as the other triboelectric surface. The standard vibration shaker system was used as a vibration source for investigating the performance of the TENG, and the frequency and amplitude was adjusted. The peak values of the electrical outputs were observed to be 187.8 V for  $V_{OC}$  and  $71.9 \mu\text{A}$  for  $I_{SC}$ , at 13.9 Hz frequency. The output power density was established to be  $3.7 \text{ W m}^{-2}$ . The authors verified their results using COMSOL Multiphysics numerical analysis method. The electric outputs were measured by applying the force of a football to the TENG and observed to be 403 V and 0.34 mA. The output generated from the TENG was also efficiently used to continuously light 100 LEDs in parallel at a resonance frequency of 13.9 Hz. These results show the possibility to

harvest the vibrational energy generated from railways, highways, and tunnels in isolated mountain areas and have potential applications for driving small and portable electronic devices.

For analyzing the deformation behaviour, Seol and co-workers fabricated a TENG that operates on the contact separation principle [210]. The authors used PDMS, which is one of the triboelectric materials with pyramid array structure, and attached it onto an Au-deposited Si wafer, while Ag layer act as both the triboelectric surface and the top electrode and Au was the bottom electrode. When pressure was applied on both surfaces, they make contact with each other; PDMS has a higher tendency to attract electrons and acquire negative triboelectric charge while Ag is electron rich and can lose electrons and acquire a positive triboelectric charge. As the pressure increased from 10 to 150 kPa, the  $V_{OC}$  also increased but stabilized for 120 sec at a vibrational frequency 2 Hz when pyramid length was 2  $\mu\text{m}$ . Additionally, they made two units: an energy-harvesting unit and a pressure-sensing unit. When the change in applied pressure was recognized, the output digital signal converted from 0 to 1 in the pressure sensing unit. Moreover, the obtained results from TENG were verified using the finite element method with the aid of COMSOL software. In the low-pressure range, the nanosized pyramid structures were useful for enhancing the output power while in the case of high-pressure range, large-sized structures were useful. This interfacial structured TENG is useful in pressure-sensing applications.

Park and his co-workers used gold nanoflowers (AuNF) as one of the electrode for fabricating the TENG [211] and used triangular shaped PDMS as another electrode. When both the electrodes approach each other and come in contact, AuNF acquires positive triboelectric charges, while PDMS has negative triboelectric charges. The obtained electrical outputs of the AuNF based TENG were observed to be 110 V and 5.5  $\mu\text{A}$  as  $V_{OC}$  and  $I_{SC}$ , respectively. A maximum power of 540  $\mu\text{W}$  (i.e., 150  $\mu\text{W cm}^{-2}$ ) was observed at the load resistance of 10  $\text{M}\Omega$ , this was able to light up more than 70 LEDs directly without using a capacitor. The authors also investigated the effect of surface morphology of the thin film by considering a flat Au surface and found that the AuNF TENG had 1.5–2 times better performance. The authors extended the study by considering electrodes made of Cu and Al flat films. While comparing the output performance of the flat Cu TENG, flat Au TENG, and flat Al TENG with the AuNF-based TENG, they found that the AuNF TENG had higher electrical outputs. They also observed that Au could withstand harsh environment conditions. It could be exposed to the air that contains 90% humidity at 50  $^{\circ}\text{C}$  for 7 h and the output of the AuNF-TENG remained same as before. This TENG was effectively used in harsh conditions, where the previously reported TENGs would not be stable.

For harvesting the biomechanical energy generated from human motions, Zhu's group successfully fabricated the TENG [77]. They used a 3D spacer fabric (yarn layer) and nylon fibers coated on graphene and PTFE as upper and bottom layers, respectively. Graphene on the nylon fibers would act as the electrode for collecting the charge generated. Because nylon is more electropositive and PTFE is an electronegative material, they acquire positive and negative triboelectric charges, respectively. When they were separated and then came closer, the electrical outputs ( $V_{OC}$  and  $I_{SC}$ ) were observed to be  $3.3 \text{ V cm}^{-2}$  and  $0.2 \text{ } \mu\text{A cm}^{-2}$ . The authors also found that when increasing the frequency from 0.5 Hz to 3.0 Hz,  $V_{OC}$  remained constant but  $I_{SC}$  increased. If the TENG pixels were increased from 1 to 3,  $I_{SC}$  increased from  $0.13 \text{ } \mu\text{A cm}^{-2}$  to  $0.28 \text{ } \mu\text{A cm}^{-2}$ . If the resistance increased,  $V_{OC}$  also increased but  $I_{SC}$  decreased. When 3 TENG pixels were used, then the output was found to be  $3.0 \text{ } \mu\text{A}$  as output current and  $16 \text{ } \mu\text{W}$  for output power at  $\sim 0.6 \text{ M}\Omega$  load resistance. The authors also used the 3D spacer-fabric-based TENG to light LEDs directly with energy harvested from human walking. This could be used to sense the pressure of human motions and in self-powered tracking systems.

The PDMS and PDMS/multiwalled carbon nanotubes (MWCNTs) as triboelectric layers were used to fabricate a flexible and biocompatible TENG [111]. Here, MWCNTs were doped in PDMS to enhance the conductivity of the PDMS, while PDMS was the biocompatible polymer. When both materials periodically came in contact with each other with force and were separated, PDMS and PDMS/MWCNT acquired positive and negative triboelectric charges, respectively. Zhu reported that the electrical performance of the TENG by varying the wt% (2 and 10) of the MWCNT in the composite. The authors also investigated the output of the 2 wt% PDMS/MWCNT devices without micropillars, as well as with square and circular micropillars. A higher  $V_{OC}$  was observed in the case of circular-micropillars-based TENG. The output electrical voltage improved as the applied force increased and was found to be 25 V for 2 wt% and 30 V for 10 wt% under 3 N vertical force. The output power at 6 M $\Omega$  and 8.6 M $\Omega$  load resistances were found to be  $\sim 130 \text{ } \mu\text{W}$  and  $\sim 120 \text{ } \mu\text{W}$ , respectively. The power density and current density were observed to be  $0.1 \text{ W m}^{-2}$  and  $0.3 \text{ } \mu\text{A cm}^{-2}$ , respectively at 3 N force. Moreover, the practicability of the TENG was validated by simultaneously lighting 16 LEDs with parallel connections. The fabricated TENG was used to powering the capacitors of 1  $\mu\text{F}$  and 3.3  $\mu\text{F}$  in 60 s to 1.1 V and 0.7 V, respectively, by using full wave rectifier. Because of the high performance, the TENG have potential applications for wearable devices.

Wu and colleagues used low-cost agriculture residue (rice husk) for the fabrication of a TENG [97] in which rice husk and PTFE were selected as the positive and negative triboelectric

materials for harvesting mechanical energy. They compared the output performance obtained from three fabricated TENGs with single rice husk used to fabricate the TENG (RH-TENG), rice husk array based TENG (ARH-TENG), and  $\text{RH}_{\text{SiO}_2}$  nanoparticles transferred on the PDMS surface to fabricate the  $\text{RH}_{\text{SiO}_2}$ -TENG. The electrical output performance of all the fabricated TENGs were compared. COMSOL software was used to verify the results and results were the same as those observed in experiments. The output electrical performance of the RH-TENG was observed to be 9 V as  $V_{OC}$ , 0.05  $\mu\text{A}$  as  $I_{SC}$  and  $\sim 125$  nW as output power at  $1.6 \times 10^8 \Omega$ . It could also light a single LED. If the two and three RH-TENGs were integrated in parallel, the observed outputs were  $V_{OC}$  14.3 V and 19 V, respectively;  $I_{SC}$  also gets superimposed. The electrical output of the ARH-TENG,  $V_{OC}$  and  $I_{SC}$ , were increased up to 190 V and 1  $\mu\text{A}$ , respectively. The output power increased to  $\sim 59$   $\mu\text{W}$ , which has the ability to power commercially available LEDs for 50s. The obtained power density was found to be  $\sim 0.12$   $\text{W m}^{-2}$ . The output performance of the  $\text{RH}_{\text{SiO}_2}$ -TENG was 14  $\mu\text{A}$  as  $I_{SC}$ , 270 V as  $V_{OC}$  and 2.13 mW as the output power under  $2 \times 10^8 \Omega$  load resistance, which drive more than 150 LEDs. The power density and current density were observed to be 0.84  $\text{W m}^{-2}$  and 5.7  $\text{mA m}^{-2}$ , respectively. The fabricated TENG opens up new perspectives for green-energy applications.

In 2016, Feng *et al.* demonstrated the polypropylene (PP) nanowire array based TENG [99], in which PP and Al were selected as the triboelectric materials from the series, according to their electronegative and electropositive magnitudes. In this work, the output performance generated from flat PP thin film and PP nanowires with chemical modifications were examined. The fabricated AAO-based TENG resulted in the highest output when using flat PP as one of the triboelectric surface and AAO as the counterpart. The performance of PP with nanowires-like structure (14  $\mu\text{m}$  length) fabricated, Al-based TENG was improved four times compared to a flat PP film and Al-based TENG. The electrical output of the fabricated TENG using PP with a nanowires-like structure (14  $\mu\text{m}$  length), Al-based TENG was found to be 157 V for  $V_{OC}$  and 1.36  $\mu\text{A}$  as  $I_{SC}$ , charge and current density as 3.3  $\mu\text{C m}^{-2}$  and 0.85  $\text{mA m}^{-2}$ , respectively. The electrical outputs of the 1H,1H,2H,2H-per-fluorooctyltrichlorosilane (PFTS) modified PP nanowire-based TENG were found to be 100 times and 25 times higher than that of flat PP film and PP nanowires based TENG, respectively. The outputs were observed to be 1900 V for  $V_{OC}$  and 30  $\mu\text{A}$  for  $I_{SC}$ , with the charge and current density as 65  $\mu\text{C m}^{-2}$  and 19  $\text{mA m}^{-2}$ , respectively. The output power generated from the TENG was verified by powering 372 commercial LEDs. To test the durability of the TENG, continuous output up to 37,000 cycles was tested. The authors also demonstrated the performance of TENG by powering a simple temperature sensor.

Further elaborating the concept, Kim's group used polystyrene (PS) for the fabrication of a TENG [104] because PS glass transition quickly forms nano- and micro- morphology when heated for 60 s in an air environment. The PS substrate formed a crumpled shape at 170 °C in the uniaxial or biaxial direction. The uniaxial shrinkage was done at different time intervals 40 s, 42 s and 44 s, which resulted in 20%, 40%, and 60% shrinkage ratios, respectively. Au and PTFE film were coated as a back electrode (positive surface) and a dielectric film (negative surface), respectively. For examining the output concert of the PS-TENG, an electrodynamic shaker was used to generate the input pulses for the contact-separation actuation at 3 Hz and 65 N. The  $I_{SC}$  of the 1D -20%, -40% and -60% PS-TENG were observed to be 8, 14 and 8  $\mu\text{A}$  and  $V_{OC}$  values were 39, 83 and 42 V, respectively. For the same force and frequency, the outputs of the 2D PS-TENG were observed to be 60 V as  $V_{OC}$ , 8.4  $\mu\text{A}$  as  $I_{SC}$  and for the pristine PS-TENG were found to be 25 V as  $V_{OC}$  and 3.1  $\mu\text{A}$  as  $I_{SC}$ . The charge densities were found to be 17.88, 49.49 and 69.3  $\text{mC m}^{-2}$  for the pristine, 1D-40% and 2D PS-TENG, respectively and output power was estimated 0.7 mW with 10  $\text{M}\Omega$  as a load resistance. The power was verified by powering the 160 LEDs simultaneously. The PS-TENG have the potential to achieve high output power and improved practicability.

The elastic bellow type TENG (B-TENG) [212] was introduced by Chung *et al.* The authors used Ag for both an electrode and positive triboelectric surface and PTFE as the negative triboelectric surface, according to triboelectric series. The finite element analysis with COMSOL software was performed to understand the output generation process. To estimate the output concert of the B-TENG, a weight of 80 g was applied and the output voltage to be 5 V due to the non-contact of the triboelectric surfaces. As the applied weight reaches to 85 g, both the surface come in full contact mode and give 20 V as the output voltage, which is four times higher than that of non-contact mode. As the applied weight increases, the voltage of the B-TENG increases but the efficiency of the B-TENG distinctly decreases due to the extra weight, which can cause fracture and fatigue. The electrical output of the single cell of B-TENG at 6 Hz frequency were found to be 132 V and 22  $\mu\text{A}$  as  $V_{OC}$  and closed circuit current ( $I_{CC}$ ), respectively. An electrical power of 408  $\mu\text{W}$  at 5  $\text{M}\Omega$  load resistance was obtained. The authors also fabricated a B-TENG in the empty space present inside the bellows to make it self-packed and found values of 111 V and 20  $\mu\text{A}$  for  $V_{OC}$  and  $I_{CC}$ , respectively. The generated electrical power has ability to light up 30 commercially available LEDs. In addition, the fabricated hybrid TENG, combining the B-TENG and traditional TENG, had output of 104 V as  $V_{OC}$  for B-TENG, while  $V_{OC}$  for the traditional TENG was 118 V. The measured  $I_{CC}$  for the B-TENG was 27  $\mu\text{A}$ , while 25  $\mu\text{A}$  was measured for the traditional TENG because of the higher surface present in the B-TENG, i.e., 12.5  $\text{cm}^2$  and



6.25 cm<sup>2</sup> for TENG. Both TENGs light 30 commercial LEDs when the device was pushed. The materials used in the TENG also have the ability to produce an electrostatic discharge (ESD); each time a peak voltage of up to 66 V measure when a spark was generated.

In another study, PTFE polymer was used as triboelectric material and polypyrrole (PPy) and act as both an electrode and a triboelectric material for fabrication of a TENG [105]. The authors fabricated a simple device using PPy via a self-powered synthesis (SPS) process and also integrated the TENG with the self-charging power system (SCPS). The outputs of the single TENG were observed at a different frequency range from 2 to 10 Hz and maximum  $V_{OC}$  and surface charge density of 52 V and 90  $\mu\text{C m}^{-2}$ , respectively. The  $I_{SC}$  increased from 3 to 45 mA  $\text{m}^{-2}$  as the frequency was increased from 2 to 10 Hz; power density was observed to be 5.8 W  $\text{m}^{-2}$  at 400 M $\Omega$  load resistance. The output is generated by pressing the TENG with a human finger and this TENG had the ability to power dozens to LEDs.

Another TENG was fabricated with PTFE (50  $\mu\text{m}$ ) as the top part and metal as the bottom part after a water-assisted oxidation (WAO) process [101]. Here, the authors considered three metals such as copper (Cu), zinc (Zn), and aluminium (Al); and oxidized them at 95 °C in deionized (DI) water for various times. They observed cubic-like microstructures, needle-like nanostructures and nanograss-like structures. The top electrode was made up of gold (150 nm) and chrome (100 nm) layers were coated on the silicon wafer using a sputtering process. The WAO Al-based TENG had higher  $V_{OC}$  for the WAO process with a time of 1 h, when compared with smooth Al surface based TENG. The WAO Cu-based TENG showed unstable and random  $V_{OC}$ , because the cubic-like structures would adhere and get transferred to the PTFE surface. The WAO Zn- based TENG showed higher  $V_{OC}$  at the WAO process time of 12 h, as compared to the smooth Zn-based TENG. A relatively small improvement in the performance of WAO Cu-based TENG was observed, while WAO Al- and Zn-based TENG resulted in enhanced performance because of the enlarged surface area. Moreover, the practicability of the WAO metal based TENG was demonstrated by integrating the thin PTFE film with the vibrating membrane type and using it to effectively harvest wind energy.

Seol's group investigated the stability of TENG on mars [126]. This TENG had the capability to withstand in harsh weather conditions. The group analyzed the effects (individual as well as combined) of different environmental factors (such as temperature, atmospheric pressure, gamma and UV radiation, atmospheric composition) on the performance of the fabricated TENG. Herein, Al sheet with positive tribo-electric polarity plays dual role as top electrode and triboelectric layer, while on the other side a PDMS thin film (200  $\mu\text{m}$ ) with negative

tribo polarity act as other triboelectric layer; Al was the bottom electrode. At 28.7 kPa force,  $V_{OC}$  and  $I_{SC}$  were observed to be 130.0 V and 7.99  $\mu$ A, respectively. The  $V_{OC}$  on mars (CO<sub>2</sub>, 8 Torr) and on earth (air, 760 Torr) atmospheric environment were found to be 27.9 V and 44.0 V, respectively. The value observed for mars was 37% less as compared to that for the earth environment. The authors also studied the performance of the TENG at different temperatures, with respect to various planets such as mars and earth, as well as in UV and gamma radiation. They observed that the TENG was stable under all of these conditions.

In 2017, the comb-shaped TENG was fabricated by Yoo *et al.* to harvest bi-directional mechanical energy [130]. They used fluorinated ethylene propylene (FEP) film (25  $\mu$ m) and ITO film in comb shape (200  $\mu$ m). These act as the contact and electrode layers, respectively, and a metal mesh stamp was fixed on the top of the FEP film. When the films (latex and FEP) came in contact with each other, the latex and FEP surfaces acquired positive and negative charges, respectively, according to the triboelectric series. In the lateral contact separation mode, the micro-pattern-comb movement on the counter layer alternately meets the non-electrode and electrode region of the micro-pattern-comb. The  $I_{SC}$  and  $V_{OC}$  of the TENG were found to be 85 nA and 6.4 V, respectively. At the pressing frequency of 0.5 Hz and a force of 58.8 N, the output  $V_{OC}$  and  $I_{SC}$  were observed to be 31 V and 339 nA, respectively. A practical demonstration of the comb-shaped TENG was carried out by lighting several LEDs and charging a capacitor. This TENG also has the potential to harvest energy generated from lateral and vertical contact/separation modes, by complex real motions in daily life.

Mallineni and co-workers fabricated a TENG using PET, ITO, and kapton [133]. Here, ITO coated PET act as both the top and bottom electrodes. On one side, adhesive kapton tap was attached to the ITO and other side ITO itself act as the triboelectric surface. The two surfaces were separated by four Pyrex insulating spacers. The fabricated TENG was stable up to 20,000 cycles. The electrical outputs were observed to be 480 V and 50  $\mu$ A as  $V_{OC}$  and  $I_{SC}$ , respectively with 490  $\mu$ W cm<sup>-2</sup> of power density without any nanopatterning. At 40 M $\Omega$  load resistance and 50 N force, the authors observed a maximum peak power of ~1.7 mW. They also performed finite element analysis using COMSOL Multiphysics to estimate the maximum output voltages. The practicability of the TENG was investigated by powering electronic calculators, lighting LEDs and so on.

Wang was inspired by biological cells and reported a bioinspired stretchable and soft TENG for harvesting biomechanical energy [213]. The TENG contained interconnected cellular structures with silicone rubber and physiological saline as the triboelectric layer and electrode,

respectively. It effectively harvest energy generated from lateral and vertical motions. The TENG with honeycomb periodic configurations guaranteed the mechanical strength, fracture toughness, indentation resistance, and shock resistance. This TENG had transmittance of 62.5% and could tolerate 600% of strain. The current and instantaneous power density were found to be  $\sim 2.65 \text{ mW m}^{-2}$  and  $\sim 11.6 \text{ W m}^{-2}$ , respectively. It was found that the skin had the ability to harvest energy generated from hand motion, which was used to power an electronic watch and other personal electronics. Furthermore, the TENG was combined with a supercapacitor to make a self-charging power system. With this emerging idea, Wang presented a new way to use skin-mounted energy harvesters to powering wearable and portable electronics.

Uddin fabricated a stacked corrugated-core sandwich-structured TENG (CCS-TENG) [125] that had the ability to work under broad range of environmental conditions and used as a self-powered active sensor. PET, polyimide, and Al were used as the triboelectric surfaces in the PI-Al-PET-Al-PI corrugated core structure. The performance of a single unit of CCS-TENG varied as the orientation (lengthwise/crosswise) of the TENG was changed among the sandwich plates. At a fixed frequency of 3 Hz, the electrical outputs were observed to be high in the crosswise assembly ( $3.2\text{--}3.9 \text{ }\mu\text{A}$ ;  $142\text{--}153 \text{ V}$ ) compared with the lengthwise assembly ( $2.7\text{--}3.1 \text{ }\mu\text{A}$ ;  $107\text{--}123 \text{ V}$ ) for the CCS-TENG. It was also observed that the electrical outputs at different frequencies (3–10 Hz) and forces (3.0 – 10.1 N) were 142 V and  $8.8\text{--}9.3 \text{ }\mu\text{A}$  as  $V_{OC}$  and  $I_{SC}$ , respectively, when the core diameters were varied. This TENG was used to effectively detect  $\text{H}_2$  gas with high response time (83%) and it was used as self-powered active sensors, efficiently operate under various external impacts.

Wu *et al.* reported a TENG that scavenged low-frequency vibration energy and was based on resonance coupling [144]. Here, Cu has dual functionality as the top electrode and as the contact material. On the other hand, PTFE fixed on Al acts as triboelectric material and have negative tribo-polarity. A steel spring was the source, with which PTFE and Cu come close to each other and acquire opposite charges, and hence producing electrical output. This entire process was verified theoretically using COMSOL Multiphysics. The electrical outputs were measured at different vibration frequencies and at  $20 \text{ M}\Omega$  load resistance. The authors observed that the average power density increased as the frequency increased from 2.5 to 4.5 Hz. The performance of the TENG was evaluated by charging the capacitor.

Moon and his co-workers fabricated the portable self-retracting TENG (PSR-TENG) [95] for harvesting energy and driving portable electronics devices. To generate multiple power peaks from a single unit, retraction and extraction process were used by combining fluttering and

stacking motions in the cylindrical form. A PTFE sheet (1 m long) was used as the triboelectric material and rolled on the rotating cylinder made of acrylic material with the help of spring. The Cu (6 cm × 2 cm) act as an electrode and attached to the acrylic sheet. When the materials met each other, the higher tribo-negative material PTFE acquired negative charge, while the tribo-positive material Cu acquired positive charge. The maximum power observed was 240  $\mu$ W for the PSR-TENG. The electrical outputs were measured by varying the distance between the electrode and the sheet. The authors also observed that as the resistance increased slowly from (10 k $\Omega$  to 1 G $\Omega$ ), then power increased while current decreased gradually. Moon *et al.* also fabricated a pen type TENG, which had the capacity to light a LED array and segment LCD screen, individually, using the hand driven energy. PSR-TENG was observed to be the higher power generation design and has the potential to power portable devices in the future.

A washable, flexible, stretchable, and robust TENG was fabricated by Ahmed and colleagues [131]. This TENG was integrated into a keyboard. Silicone rubbers, urethane, and carbon nanotube (CNTs) electrodes were used to fabricating the keyboard. The mechanical energy generated by finger tapping on the keyboard would be effectively converted into electrical energy and the energy produced through self-powering mechanisms of TENG was used for wireless communication with computers. When both materials come in contact with each other, silicone acquires negative charges while urethane acquires positive charges, according to the tribo-electric series. The electrical outputs generated by the finger-tapping TENG were found to be 6.5 V, 1.5  $\mu$ A and 15 nC as maximum voltage, current, and charge, respectively. The fabricated TENG had constant electrical output even with various environmental effects such as humidity. It could also detect different typing patterns of the keyboard, which were used in security and privacy of computers. The authors also observed that the capacitor was charged up to 3 V, at 5 Hz frequency with 120 min regular typing. This TENG has various other applications for lighting displays, wearable electronics, etc.

Recently, Jin *et al.* designed and analyzed a self-powered sensor in the form of TENG [127] in which energy generated through finger motions was converted into electrical signals. They used PET as the substrate material, FEP as the triboelectric material, and Al as both the electrode and triboelectric contact surface. When they contact with each other, FEP being highly tribo-electronegative material gains negative charge while Al gains an equal amount of positive tribo-charge. The electrical output current signals generated by finger straightening and bending motions was 7.8  $\mu$ A, the transferred charge quantity of 78 nC and output voltage of 130 V at 30 M $\Omega$  of external load resistance was observed. The fabricated TENG self-powered sensor system

was attached to different joints of the finger to detect and monitor the signals. This has many potential applications in robot manufacturing, artificial intelligence systems, and other detecting applications.

For the first time, a fully self-healing TENG in which the TENG has the ability to recover its output performance even after harm by using electrodes was demonstrated by Xu and colleagues [115]. It consisted of small magnets and healable polymer materials for the fabrication of the TENG. The authors used polydimethylsiloxane-polyurethane (PDMS-PU) as the healable polymer material and small magnets were incorporated in the healable electrode. When any damage occurred in the TENG, by connecting the broken ends, magnetic-assisted electrodes and PDMS-PU were self-recovered. The electrical output performance of the TENG was found to be 20 V, 1.9  $\mu\text{A}$  and 6  $\text{mW m}^{-2}$  as the  $V_{OC}$ ,  $I_{SC}$  and maximum power density, respectively at 10  $\text{M}\Omega$  of external load resistance. After damage, the self-healing TENG had the ability to restore its output to 95% of the original device performance. This self-healing capability in a TENG offers feasible strategies for developing self-powered sensors with properties of recoverability, adaption, life span, and robustness.

Chen with his group has reported the highly flexible capillary tube TENG composed of tabular sandwich structure of PTFE capillary tube, Si rubber hermetic tube and double helix Al foil [214]. Because of Maxwell's displacement, the current generated by microfluidic flow used for the biological and chemical monitoring/detection. This TENG requires just 0.5  $\mu\text{L}$  or less than this amount of microfluid for detection/monitoring. The electrical outputs generated from this TENG were found to be 1.1 V, 130 nA and 0.9 nC as  $V_{OC}$ ,  $I_{SC}$  and  $Q_{SC}$ , respectively.

Dai *et al.* has been first time proposed the self-powered high-g acceleration based TENG [186]. The TENG is having  $14 \times 14 \times 8 \text{ mm}^3$  as total volume, which is smaller than a coin. The acceleration sensor was made up from Al foil with a beam structure, which would act as positive electrode. The PDMS functional film was coated with Cu act as negative electrode. Herein, the mechanical chucking was used for the packaging of the device. When both the material come in physical contact with each other, positive tribo-charges are acquired by Al and negative tribo-charges are acquired by PDMS polymer. The acceleration sensor can sense the acceleration with a sensing range and sensitivity of up to  $1.8 \times 10^4 \text{ g}$  and  $1.8 \text{ mV g}^{-1}$ , respectively without external power source. For measuring high-g acceleration quantitatively, as the acceleration increased from 2,600 to 16,000 g, the peak voltage also increased from 10 V to 100 V. For further clarification, the obtained results were verified through simulation using COMSOL multiphysics software. For high-g test, Machete hammer test approach was extensively used.

Dong has fabricated the flexible TENG in vertical contact-separation mode and compared the results obtained using MXene and PTFE materials as negative tribo-surfaces and acquired higher electrical outputs with MXene [119]. The TENG was fabricated using ITO coated PET as top electrode and MXene coated glass as another electrode. Four insulating spacer made up of pyrex (5 mm × 5 mm) was used to separate the electrode with an air gap of 1 mm. Cu wires were used to collect the charges in the form of electrical current and voltage from the TENG. When the operation of TENG starts, both the surfaces comes in contact with each other then, PET having positive triboelectric material acquires positive charges and MXene having –OH, –O and –F functional groups acquires negative tribo-charges. The electrical outputs i.e.  $V_{OC}$  and instantaneous power peak were obtained to be ~500 to ~650 V and ~0.5 – 0.65 mW, respectively. This TENG has the ability to light more than 60 LEDs or it can also charge the capacitor (1  $\mu$ F) up to 50 V.

### 2.1.2 Single electrode mode

In this mode of TENG, one of the electrode is made ground and motion of the surfaces is in vertical direction [67–69]. If the TENG has limited size, the contact and separation of both the electrodes would alter the local electrical field distribution so the electrons would exchange between the ground and the bottom electrode to maintain the potential difference between the electrodes. The single electrode mode was used to harvest energy, which could be generated from turning the book pages [70], air flow [71], rain drop [69], and rotating tire [72]. The fabricated TENG was used in various sensors like in visualized touch sensors [84], self-powered displacement vector sensors [67], velocity sensors [215,216], active tactile sensors [217,218], biosensors [219], sensors for healthcare monitoring [220], self-powered distress signal emitters [221], angle measurement sensors [221], pressure sensors [222], water/ethanol sensors [200], and self-powered identification systems [223].

Single electrode based sliding TENG [67] was demonstrated by Yang's group. In which, both separation and periodic overlapping among the Al electrode and PTFE by relative sliding is present, here the inner surfaces of the two plates make intimate contact between them. The authors reported the sliding TENG, in which both the plates slid with short-edges against each other by the mechanical motion. The PTFE surface was dry-etched using ICP and uniform distribution of nanoparticle-like morphology with mean diameter of 200 nm, and the triboelectric charge density increased. When PTFE and Al came in contact with each other, the electrons were ejected from Al to PTFE because PTFE is a much more negative triboelectric material as compare to Al, according to triboelectric series. The negative charge produced on the surface would be

conserved for a long time because of the insulating behavior of PTFE [224]. The process of generating an output voltage and current were carried out by sliding both the surfaces inward and outward, respectively. The numerical simulation technique, COMSOL, was used to verify the charge transfer among Al and ground, and the electric potential distribution in the sliding TENG. The output performance in terms of  $V_{OC}$  and  $J_{SC}$  were observed to be 1100 V and 6 mA m<sup>-2</sup>, respectively. Additionally, the obtained electrical output signals generated by the sliding TENG were confirmed by lighting up the 100 green LEDs. If the thickness of the PTFE film were to be increased, the lifespan of the fabricated TENG would be increased up to several years. Moreover, this type of TENG was used for observing the speed as self-powered displacement sensors and as self-powered sensor systems.

Further on elaborating this work, Yang with co-workers demonstrated an arc-shaped single electrode based TENG [68], that was based on PA/PTFE and Al as electrodes. The contact-separation among the finite size of PA/PTFE film and Al foil may affect the charge transfer between the ground and Al foil to sustain the equal potential boundary conditions; cycled contact and separation of the PA/PTFE films results in electric current/voltage. The energy generated from this type of TENG could directly light tens of serially connected green LEDs. Because of the kapton film, the TENG has arc-shaped structure which is useful for the effective contact separation between the PA/PTFE thin film and Al foil. Using mechanical force from a finger (touching), PA thin film and Al foil come close to each other; PA is more electropositive than Al and acquires positive surface charge; Al foil acquires negative surface charge. The generated electrical outputs (current and voltage) by mechanical energy (through finger touching) were found to be 10  $\mu$ A and 150 V, respectively. When the TENG experienced compressive force, it contributed positive voltage/current and force was released, giving negative voltage/current. By replacing PA with PTFE, the polarity of the obtained output current/voltage was found to be reversed because PTFE is a more electronegative material than Al and acquires negative tribo-charge, while Al is an electropositive material and acquires positive tribo-charge. To better understand the single electrode TENG, numerical simulations based on COMSOL were used to verify the charge transfer between the Al foil, ground, and electric potential distribution in the TENG. Yang also examined the output of the two TENGs, individually and when connected in parallel. The authors found that the total output increased and was almost equal to the sum of the distinct electrical outputs (current and voltage). This was further verified by lighting tens the LEDs directly with the TENG. Additionally, 16 TENGs were arranged in a 4×4 matrix and fabricated the sensor, which was used to measure the applied pressure and to sense the motion route of the output voltage signals.

For harvesting the energy generated from streaming water, Liang successfully fabricated a transparent TENG (T-TENG) [69]. The mechanical energy generated from the motion of the streaming water and the electrostatic energy harvested from the tribo-charges through the contact electrification method by air or any other materials. Here, glass was selected as the substrate material for the fabrication of the T-TENG. Fluorine-doped tin oxide (FTO) was selected as one of the electrode and a PTFE film was the other. The principle of an antireflection coating is intrusion of the reflected light from the coating-air and substrate-coating interfaces. It is necessary to have the refractive index of the coatings between the air and that of the substrate. There are two conditions (Equation 2.7) and (2.8) that must be fulfilled for an ideal antireflection coating to have single layer [225], i.e.;

$$n_1 = \sqrt{n_0 n_2} \quad (2.7)$$

$$d = \frac{(2k+1)\lambda}{4n_1} \quad (2.8)$$

where  $\lambda$  is the wavelength of the incident light,  $n_0$ ,  $n_1$ , and  $n_2$  are the refractive indices of air, the PTFE film, and FTO, respectively (they are equal to 1, 1.35, and 1.8, respectively), and  $k$  is a constant equal to 0, 1, 2 and 3. The T-TENG working was explained by considering streaming tap water from a household faucet and based on the single electrode mode. The water drop becomes charged when it travels through an insulating tube or falls from the sky, and therefore triboelectricity generated. To understand how the energy is generated, we considered the positively charged water drop. When the PTFE film approaches the positively charged water drop, a positive potential difference is developed between the ground and the FTO electrode, and when water drop leaves the film, a negative potential difference is developed. Here, the streaming water comes and leaves the T-TENG sporadically, and constant outputs are received. Considering the flow rate of tap water to be  $93 \text{ mL s}^{-1}$ , the electrical outputs were found to be 10 V,  $2 \text{ mA cm}^{-2}$  and  $11.56 \text{ mW m}^{-2}$  for  $V_{OC}$ , current density and power density, respectively, with a load resistor of  $0.5 \text{ M}\Omega$ . The T-TENG with PTFE film (1 mm) showed better transmittance of 87.41%, which is larger than that of glass substrate (83.41%). With the above mentioned features, the fabricated T-TENG has the capability to be incorporated with the solar cells, car glass, building glass and can also harvest the energy from water present in the ambient environment.

Chu *et al.* used PET ( $<0.9 \text{ }\mu\text{m}$ ), PDMS ( $<1.5 \text{ }\mu\text{m}$ ) and thin graphene ( $<1 \text{ nm}$ ) as the substrate, electrification layer and electrode, respectively, for the fabrication of a conformal graphene-based TENG [78]. The total thickness of the fabricated TENG was observed to be  $\sim 2.4$



$\mu\text{m}$  and had conformal contact with human skin. For increasing the electronegativity of the PDMS polymer, conformal adhesion of fluorine was done on the surface of PDMS. Furthermore, the authors compared with the outputs of TENGs made from the as-prepared surface (AP) without any surface treatment, nanostructure surface (NS), functionalized surface (FS), and nanostructured and functionalized surface (NFS). They observed that the AP-TENG had low  $V_{OC}$  (3.5 V) and  $I_{SC}$  ( $\sim 0.65 \mu\text{A}$ ), while NFS-TENG exhibited higher  $V_{OC}$  (47.1 V) and  $I_{SC}$  ( $7 \mu\text{A}$ ). The NFS-based TENG gives a maximum output power of  $130 \mu\text{W}$  at  $20 \text{ M}\Omega$  load resistance. The NS-TENG showed good stability even after 2 weeks, while NFS- and FS- based TENGs showed systematic degradation of  $V_{OC}$  (28%) and  $I_{SC}$  (18%) after 4 days; after 6 days, further degradation in the outputs was not observed, i.e., they showed good output performance with  $V_{OC}$  of 35.1 V and 27.1 V with  $I_{SC}$  of  $5.6 \mu\text{A}$  and  $4.1 \mu\text{A}$ , respectively. The electrical performance of the TENG was explored by integrating it on human skin with different types of fabrics including silk, latex, nylon, and cotton. Higher  $V_{OC}$  and  $I_{SC}$  were observed in the case of latex. The authors also studied the performance by changing the contact pressure (30 – 40 kPa) with one, two and three fingers and observed 4.1, 8.3 and 12.5 V, respectively. This work could inspire establishment of the interface between human and machine and in assistive devices.

Dhakar and co-workers developed a flexible TENG [80] that could detect human finger motions as well as can harvest the biomechanical energy and convert it into electrical energy. This was done by using micropatterned PDMS, and a gold electrode at the top and bottom were directly attached to the polyimide substrate. Other side, the epidermis layer was attached on the skin. This is observed that because of finger movement, the joint angle increases and the flexible device would be removed from the epidermis. Due to the conductive nature of epidermis and large surface area, it was considered that ground and charges are redistributed. As the distance decreases, the gap increases between the PDMS film and epidermis. The capacitance varied from  $6.9 \text{ pF}$  to  $1.2 \text{ pF}$  as the angle increases from  $60^\circ$  to  $180^\circ$ , respectively, and sensitivity also increased. When there was a decrement in joint angle, the capacitance among the gold electrode and epidermis decreased, which led to a further decrease in capacitance coupling. The electrical measurements were observed to be  $70 \text{ V}$  as output voltage and  $2.7 \mu\text{A cm}^{-2}$  as current area density at  $5 \text{ M}\Omega$  load resistance. The output generated from the flexible TENG was verified by powering commercial LEDs. This flexible TENG has many applications in powering small wearable devices and self-powered sensors, as well as in robotics for electronic skin applications.

To elaborate on the concept and improve the output of the TENG, Dhakar used a patterned PET film and a Cu film as the negative and positive triboelectric surfaces for fabricating a large

scale TENG (LS-TENG) [110]. The patterned PET film, which consisted of roll-to-roll UV embossing acts as an electrode in the LS-TENG. The authors fabricated different embossing patterns that contained three types of square-shaped patterns and two types of line patterns of the contact surface. The measured electrical outputs for the fabricated LS-TENG were  $344.63 \pm 1.37$  V and  $18.12 \pm 0.13$   $\mu$ A for  $V_{OC}$  and  $I_{SC}$ , respectively, and peak power density was  $62.5$  mW m<sup>-2</sup> by palm taping. The authors replaced Cu with ITO and measured the outputs as  $315.10 \pm 16.69$  V and  $17.66 \pm 0.33$   $\mu$ A for  $V_{OC}$  and  $I_{SC}$ , respectively, and output power density was found to be  $53.82$  mW m<sup>-2</sup>. While comparing the electrical outputs of the LS-TENGs, the TENG with Cu film and patterned PET film had higher electrical output performance. The power of the Cu-based LS-TENG was demonstrated by directly powering 90 commercial LEDs by palm tapping. A commercial three-axis accelerometer was attached to the back of the chair and the electrical outputs generated from the LS-TENG in three positions of the subject were observed: high, low, and no activity positions were observed, with 85 V as  $V_{OC}$  and 0.75  $\mu$ A as  $I_{SC}$  for high activity region and 35 V as  $V_{OC}$  and 0.3  $\mu$ A as  $I_{SC}$  for low activity region. The LS-TENG is used in the sensor arrays for electronic skin, motion tracking, posture monitoring, tactile sensing, and many other applications. Additionally, TENG has also applications in the motion tracking over the array of a cylindrical object rolling and for posture monitoring.

In 2017, the flexible (transparent and non-transparent) TENG was fabricated by Chen [164]; it could harvest mechanical energy and be used as force sensor. The non-transparent TENG consisted of three layers, i.e., PTFE, Al, and PET as the triboelectric layer, electrode layer, and substrate layer, respectively. While the transparent TENG also had three layers: fluorinated ethylene propylene (FEP), an indium tin oxide (ITO) layer, and a polypropylene (PP) layer as the tribo-electric surface, electrode layer, and substrate layer, respectively. When the TENG was pressed by latex-glove-covered human palm, the peak output current and voltage were observed to be 78  $\mu$ A and 340 V, respectively, and had the capacity to light up 70 LEDs. When TENG acts as a force sensor, it had a detection sensitivity of  $0.947$   $\mu$ A MPa<sup>-1</sup>. Due to the simple, light weight and flexible structure, the TENG has potential for many applications in the fabrication of sensing systems and wearable electronics.

Ma *et al.* presented a smart floor tracking system by using single electrode TENG [226], in which polyvinyl chloride (PVC) flooring was coupled with a thin copper film. When rubber (latex) and PVC come in contact with each other, the positive triboelectric charges were acquired by rubber and, to balance the charge, an equal number of negative charges were acquired by PVC. A Cu electrode was used to collect the charges. When force increased from 110 N to 310

N, electrical outputs are observed to be increased;  $I_{SC}$  increases from 1.7 to 12.2  $\mu\text{A}$ ,  $V_{OC}$  showed a similar trend, increasing from 85 to 220 V, and power density was found to be 0.76  $\text{W m}^{-2}$ , which could drive at least 250 green LEDs. This TENG also had the ability to analyze the movement and track footstep patterns. TENG worked as a self-driven smart floor and also has diverse multifunctional applications (such as patient monitoring, entertainment, security surveillance, asset tracking), making it useful for future applications.

Xu and co-workers reported an aeroelastic flutter based TENG (AF-TENG) [227] that could effectively scavenge wind energy and work as a wind speed sensor. The AF-TENG consisted of a membrane in a cuboid acrylic channel and two copper layers. The authors studied the effect of different membrane materials (FEP, PTFE, and kapton (PI)), humidity, length of membrane, and speed of inlet wind on the output performance of the TENG. When wind flowed through the channel, the membrane between the copper surfaces moved up and down, resulting in the electrical outputs of the AF-TENG. As the humidity in the environment increased, the output voltage and current decreased drastically. The peak voltage was found to increase when the wind speed increased from 3.1 to 9.2  $\text{m s}^{-1}$ ; on further increasing the wind speed from 9.2 to 10.8  $\text{m s}^{-1}$ , peak voltage decreased. The analyzing frequency of the voltage was measured and it was almost same as that of commercial wind speed sensor; speed sensitivity was found to be 7.7  $\text{Hz/m s}^{-1}$  of 0.13 ( $\text{m s}^{-1}$ )  $\text{Hz}^{-1}$ . Even in a high humidity environment, the fabricated AF-TENG has various applications in wireless environmental monitoring.

A leaf-molded transparent TENG based on consistent contact/separation among the patterned PDMS and human skin was fabricated by Sun *et al.* [147]. A PDMS film was combined with a long silver nanowires network that was used as an electrode. The charges from the patterned PDMS film were collected through silver nanowires. The texture of patterned PDMS thin film resembled a ramified leaf pattern. When the PDMS film was pressed with the skin of a human hand, PDMS acquired negative triboelectric charges, while human skin became positive, according to triboelectric series. The electrical outputs generated from TENG were found to 56 V and 3.1  $\mu\text{A}$  as  $V_{OC}$  and  $I_{SC}$ , respectively. The fabricated TENG showed amazing transparency of 88%, due to which it was integrated with electrochromic device (ECD) to form user interactive self-powered wearable device. This smart device had the ability to detect changes via relative interactions between the color of an electronic facial mask and dynamic frictions (produced by body motion). If a heart-beat or pulse was used to drive a TENG, healthcare and entertainment was combined into a smart device that could lead to an enjoyable and healthy life.

Liang *et al.* reported the recyclable TENG [154] for harvesting ambient mechanical energy (such as heart beating, vibration, etc.) into electrical signals. For the fabrication of the TENG, sodium alginate film (SA (<500 nm thick)) and polyvinyl alcohol (PVA) act as the contact triboelectric materials while aluminium (Al) and lithium (Li) were used as current collectors. The electrical outputs were found to be 3.9 nA, 1.47 V and 3.8 mW m<sup>-2</sup> as output current, voltage, and instantaneous power density, respectively. To use the TENG as a self-powered nanosensor and as self-powered tracking system, it was integrated with a PMMA tube and a steel ball used to stimulate a moving object. The TENG was also used to monitor and track the action of the heart or lung and a moving object, respectively. This recyclable and soluble TENG offers new possibilities for biomedical implants, secure electronics, and environmental monitoring.

This TENG offers many applications such as wireless sensors for automobiles and self-powered electronic systems. The comparative study based on various modes of TENGs is illustrated in **Table 2.1**.



**Table 2.1.** Comparative study for different modes of fabricated TENGs

Modes of operation	S. No.	Authors	Structure of TENG	Open Circuit Voltage (Voc) (V)	Short Circuit Current (Isc) ( $\mu$ A)	Current Density (A m <sup>-2</sup> ) and Power Density (W m <sup>-3</sup> or W m <sup>-2</sup> ) / Power (W)	Load Resistance (M $\Omega$ )	Reference
Vertical Contact separation mode	1.	Fan <i>et al.</i>	Au/Au-Pd/PET/kapton/Au-Pd/Au	3.3	0.6	$\sim 10.4 \times 10^3$ W m <sup>-3</sup>	-	[47]
	2.	Chen <i>et al.</i>	Acrylic/Cu/PTFE/Al/Acrylic	287.4	76.8	$726.1 \times 10^{-3}$ W m <sup>-2</sup>	5	[50]
	3.	Zhong <i>et al.</i>	PET/Ag/PTFE/Cu/electrode	407	$\sim 33$	$\sim 4.125 \times 10^{-3}$ W	$3 \times 10^2$	[51]
	4.	Yang <i>et al.</i>	PET/Cu/PTFE/Al/PET	428	$1.395 \times 10^3$	$30.7$ W m <sup>-2</sup>	2	[53]
	5.	Hou <i>et al.</i>	PDMS/Cu/Spacer/ITO/PET	3.0–3.4	$24 \times 10^3$	$8$ A m <sup>-2</sup>	$10^3$ – $10^2$	[55]
	6.	Zhu <i>et al.</i>	Yarn/graphene coated nylon nanofibers /spacer /PTFE coated nylon nanofibers /yarn	3	0.3	$16 \times 10^{-6}$ W	0.6	[77]
	7.	Zhu <i>et al.</i>	Glass/Al/PMMA/spacer/kapton nanowires/kapton/Al	110	6	$31.2 \times 10^3$ W m <sup>-3</sup>	-	[191]
	8.	Wang <i>et al.</i>	Al/PDMS/kapton/SiO <sub>2</sub> /electrode	230	94	$128 \times 10^3$ W m <sup>-3</sup>	$5 \times 10^2$	[195]
	9.	Zhu <i>et al.</i>	PMMA/Au/PDMS/spring/Au nanoparticles/Au/PMMA	$\sim 1200$	$2 \times 10^3$	$313$ W m <sup>-2</sup>	1	[196]
	10.	Hu <i>et al.</i>	Acrylic/Al coated AAO/ spacer/ plasma etched kapton/ kapton film/ Cu film	110	15	$2.76$ W m <sup>-2</sup>	6	[197]
	11.	Cheng <i>et al.</i>	CD	PMMA/Au thin film/PDMS/ SiO <sub>2</sub> nanoparticles/ Au thin film/PMMA	285	264	$1325$ A m <sup>-2</sup> and $3.6 \times 10^5$ W m <sup>-2</sup>	$5 \times 10^{-4}$
	ID		115		5.2	$104$ A m <sup>-2</sup> and $1.4 \times 10^4$ W m <sup>-2</sup>		

12.	Zhang <i>et al.</i>	Al/PA or PTFE/Cu	57	6	-	-	[200]
13.	Fan <i>et al.</i>	ITO/PET/PDMS/spacer/ITO/PET	200	7	$0.78 \times 10^{-6} \text{ A m}^{-2}$	~30	[202]
14.	Li <i>et al.</i>	Al/PET/Cu/kapton	40	30	$\sim 2.5 \times 10^{-3} \text{ A m}^{-2}$	-	[203]
15.	Sun <i>et al.</i>	Kapton/ Ag paste/ EC/ PLLA/ Ag paste/ kapton	310.5	16.2	-	-	[204]
16.	Ye <i>et al.</i>	Al/ P(VDF-HFP) nanofibers/ spacer/ kapton/ Al film	45	-	$49 \times 10^{-10} \text{ A m}^{-2}$ , $0.37 \times 10^{-3} \text{ W}$	$10^2$	[205]
17.	Yun <i>et al.</i>	Acrylic/ITO/PET/PDMS/NaOH sparkling/PET/Acrylic	49.3	1.16	$185.7 \times 10^{-13} \text{ A m}^{-2}$	-	[206]
18.	Huang <i>et al.</i>	PET/ Al/ PHBV nanofibers/ PVDF-GO nanofibers/Al/PET	340	78	$2.3 \text{ W m}^{-2}$	8	[207]
19.	Chen <i>et al.</i>	PET /Cu /PTFE nanowires/ Al/ Acrylic/ Al/ PTFE nanowires/ Cu/ PET	180	50	$0.26 \times 10^{-7} \text{ W m}^{-2}$	1	[208]
20.	Zhang <i>et al.</i>	PMMA/Al/PMNF/ spacer/ PDMS/ Al/ PMMA	187.8	71.9	$3.7 \text{ W m}^{-2}$	3	[209]
21.	Seol <i>et al.</i>	Acrylic/ Cr or Au/ PDMS/ spacer/ Ag/ Acrylic	5	30	-	-	[210]
22.	Park <i>et al.</i>	Si wafer/ Cr/ Au/ Au nanoflowers/ spacer/ PDMS/ Au/ Cr/ Si wafer	110	5.5	$150 \times 10^{-10} \text{ W m}^{-2}$	10	[211]
23.	Zhu <i>et al.</i>	Al/ PDMS/ spacer/ PDMS-MWCNTs/ Al	30	3.3	$0.3 \times 10^{-10} \text{ A m}^{-2}$ and $\sim 130 \times 10^{-6} \text{ W}$	6	[111]
24.	Wu <i>et al.</i>	Cu/PET/PDMS/Rice husk/spacer/PTFE/Cu	270	14	$5.7 \times 10^{-3} \text{ A m}^{-2}$ and $0.84 \text{ W m}^{-2}$	$2 \times 10^2$	[97]
25.	Feng <i>et al.</i>	PET/Al/ spacer/PP/Cu/PET	157	1.36	$0.85 \text{ mA m}^{-2}$	-	[99]
26.	Kim <i>et al.</i>	PS/Au/spacer/PTFE/Au	25	3.1	-	10	[104]
27.	Chung <i>et al.</i>	Paper/ Ag/ spacer/ PTFE/ Ag/ Paper	132	22	-	5	[212]

	28.	Wang <i>et al.</i>	Acrylic/ PPy/ kapton(spacer) / PTFE/ PPy/ Acrylic	52	-	$45 \times 10^{-3} \text{ A m}^{-2}$ and $5.8 \text{ W m}^{-2}$	$4 \times 10^2$	[105]
	29.	Park <i>et al.</i>	Au/ Zn/ Zn nanowires or Cu nanoparticles or Al nanostructures/ spacer / PTFE/ Au	200	~10	-	-	[101]
	30.	Seol <i>et al.</i>	Al/spacer/PDMS/Al	130	7.99	-	-	[126]
	31.	Mallineni <i>et al.</i>	PET/ITO/spacer/kapton/ITO/PET	480	50	$\sim 490 \times 10^{-2} \text{ W m}^{-2}$	40	[133]
	32.	Uddin <i>et al.</i>	PET/Al/MC/PI-Al-PET-Al-PI/MC/Al/PET	142–153	3.2–3.9	-	-	[125]
	33.	Ahmed <i>et al.</i>	Silicone/electrode/silicone/spacer/urethane/electrode/urethane	6.5	1.5	-	40	[131]
	34.	Jin <i>et al.</i>	PET/Al/FEP/spacer/Al/PET	130	7.8	-	30	[127]
	35.	Xu <i>et al.</i>	PDMS-PU/magnetic top electrode/ spacer/ magnetic bottom electrode	20	1.9	$6 \times 10^{-3} \text{ W m}^{-2}$	10	[115]
	36.	Chen <i>et al.</i>	Micro-liquid/PTFE/Al/Silicon rubber	1.1	0.13	-	-	[214]
	37.	Dai <i>et al.</i>	Al/PDMS/Cu	10 to 100	-	-	-	[186]
	38.	Dong <i>et al.</i>	Glass/MXene/spacer/PET/ITO	~500 to ~650	6.3 to 7.5	~ 0.5–0.65 mW	-	[119]
<b>Single electrode mode</b>	39.	Yang <i>et al.</i>	Al/ slider/ PTFE	1100	-	$6 \times 10^{-3} \text{ A m}^{-2}$ and $350 \times 10^{-3} \text{ W m}^{-2}$	$10^2$	[67]
	40.	Yang <i>et al.</i>	Kapton/PA or PTFE/ spacer/ Al/ PMMA / Al/ spacer/ PA or PTFE/ kapton	150	10	-	$10^2$	[68]
	41.	Liang <i>et al.</i>	Glass/ FTO/ PTFE/ water drops	10	-	$2 \times 10^{-2} \text{ A m}^{-2}$ and $11.56 \times 10^{-3} \text{ W m}^{-2}$	0.5	[69]
	42.	Dhakar <i>et al.</i>	Si/ Epidermis layer/ PDMS/ Polyimide/ Gold	70	-	$2.7 \times 10^{-10} \text{ A m}^{-2}$	5	[80]

43.	Chu <i>et al.</i>	Cloth/Skin/ PET substrate/ graphene electrode / NFS-PDMS / skin/ cloth	47.1	7	-	20	[78]
44.	Dhakar <i>et al.</i>	PET/ spacer/ copper/ liquid crystal polymer	85	0.75	$62.5 \times 10^{-3} \text{ W m}^{-2}$	10	[110]
45.	Chen <i>et al.</i>	Nylon/spacer/PTFE/Al	340	78	$8.58 \times 10^{-3} \text{ W}$	6	[164]
46.	Ma <i>et al.</i>	PVC flooring/ spacer/ Cu film/ Cu electrode	220	12.2	$0.76 \text{ W m}^{-2}$	30	[226]
47.	Sun <i>et al.</i>	Human skin/ spacer/ patterned PDMS/ Ag nanowires	56	3.1	-	-	[147]
48.	Liang <i>et al.</i>	Al electrode/ alginate sodium/ patterned PVA/ Li electrode	1.47	$3.9 \times 10^{-3}$	$3.8 \times 10^{-3} \text{ W m}^{-2}$	-	[154]



## 2.2 Key challenges

The key challenges for researchers in the field of TENGs are as follows:

1. TENGs operate on four basic modes, but the operating conditions and structural designs are very different, so it is very important to quantify a parameter which is used to measure the performance; the  $ZT$  factor and power conversion efficiency are used for thermoelectrics and solar cells, respectively. Each mode has a different energy conversion efficiency, whereas the materials used are the same but depend on the geometry design and triggering conditions.
2. The typical features of TENGs are low output current and high output voltage. However, portable electronic devices require few volts to operate. It is therefore essential to develop a lower output voltage without sacrificing the output power. This can be achieved by attaching a perfect transformer to lower the output voltage and maximize the power transfer efficiency. To apply TENGs in practical applications, the used triboelectric materials should be exhibited high durability at high frequency.
3. The outputs generated by TENGs through energy harvesting in diverse environments are different. The outputs are unstable, time-dependent, and unpredictable; whereas for driving the electronics, fixed power, and input voltage is required. It is therefore necessary that the generated energy be stored in a capacitor or battery, and this stored energy is then used in a regulated manner to power the portable electronic devices.

## 2.3 Factors responsible for the output of TENG

The output of the TENG is mainly depends on the three main reasons.

1. The contact materials are having some morphological structures like nanofibers, nanoparticles, nanopillars, etc. These nanostructures has the ability to attain maximum charges on the surfaces.
2. Due to elastic behaviour of the polymers have proper contact between the surfaces. These polymers can smoothly deform by applying low pressure on the surfaces and it will fill the empty spaces, which will come in the fabrication defects. This can be possibly enhances surface contact area.

3. Accordingly the triboelectric series, that materials has to be selected, which have large gap between the materials and enhances the triboelectric charges while contacting, leading to the largely improved surface charge density, and hence exhibit larger electrical outputs.

## 2.4 Identified Research Gaps

- ❖ In the last decade, the TENGs are fabricated using different polymers having different morphologies. But the composite polymer matrixes are not used in the fabrication process. So, in this regard, carbon based nanofillers (like reduced graphene oxide nanoribbons (rGONRs), fluorinated – graphene nanoribbons) are used as composite material with polymer for enhancing the charge trapping phenomenon.
- ❖ This has been proved that the carbon based nanofillers exhibit negative charge on the surface due to the presence of numerous electronegative groups like oxygen containing groups such as hydroxyl (OH) group on basal plane, carboxyl (-COOH) group on sheet edges, epoxy (C-O-C) groups joining to adjacent carbon atoms with single bond and fluorine (-F) group present on the basal planes. Therefore, the amount of negative surface charge highly depends on the oxygen atoms. When the carbon based nanofiller is combined with the higher tribo-negative material i.e. polymer, then it enhances the tribo-negativity of the resulting material, which will be a good impact for output performance of TENG.

## 2.5 Research Plan

- (i) Synthesis of the reduced graphene oxide nanoribbons (rGONRs) through unzipping of MWCNTs using various chemicals like  $H_2SO_4$ ,  $HNO_3$  and  $KMnO_4$ . Then prepare the rGONRs incorporated PVDF solution for fabrication of thin film. Various characterizations are performed to analysis the surface morphology, crystallographic information, presence of various functional groups, filler incorporation in PVDF matrix and so on.
- (ii) Further, this thin film is used in the fabrication of the TENG. Herein, thin film act as negative triboelectric material in the TENG and other side is Al act as positive triboelectric material as well as electrode for the collecting the charges. After fabrication of the TENG, characterizations of the TENG are carried out.

- (iii) Functionalization (i.e. Fluorination) of the synthesized rGONRs by using hydrofluoric (HF) acid and obtained fluorinated graphene nanoribbons (F-GNRs) are characterized.
- (iv) Then composite is prepared using F-GNRs and PVDF polymer matrix, which is further used for the nanofibers fabrication. The nanofibers fabricated using composite material are considered to act as negative triboelectric material, as PVDF lies in the higher electronegative side of the triboelectric series and F-GNRs also enhances the electronegativity of the resulting material. On the other hand, nylon polymer is selected as electropositive material from the triboelectric series. Nylon nanofibers are fabricated using electro-spinning process and further used in the fabrication process of the TENG. Then the fabrication of the TENG is carried out and TENG characterizations are performed.







## Chapter 3

### EXPERIMENTAL DETAILS

---



### 3.1 Materials and Chemicals used

Multiwalled carbon nanotubes (MWCNTs) were purchased from Hanwha Nanotech Co. (Republic of Korea). The length and outer diameter of MWCNTs were found to be 10–20  $\mu\text{m}$  and 10–30 nm, respectively with average purities more than 95%. Poly (methyl methacrylate) (PMMA-IG 840), polyvinylidene fluoride (PVDF-6008/001 Solef), Nylon 6,6 (A-305) were purchased from LG Chemicals; Solvay; and Lanxess, India, respectively. Kapton tape was purchased from Jay Industries, Mumbai, India; concentrated sulphuric acid ( $\text{H}_2\text{SO}_4$ ) of 98% purity, ether of 98% purity, dichloromethane (DCM) of 99% purity, acetone, dimethylacetamide (DMAc) of 99% purity were purchased from Himedia laboratories Pvt. Ltd. Mumbai, India; potassium permanganate ( $\text{KMnO}_4$ ) of 99% purity, hydrogen peroxide ( $\text{H}_2\text{O}_2$ ) of 30% purity, formic acid, and hydrofluoric acid (HF) were purchased from Rankem, RFCL Ltd. New Delhi, India; dimethylformamide (DMF) of 99% purity was purchased from Avantor, Maharashtra, India and Al membrane was purchased from local market. All the analytical grade chemicals are used without any further purification.

### 3.2 Synthesis of various nanofillers

#### 3.2.1 Reduced oxidized graphene nanoribbons (rGONRs)

Reduced oxidized graphene nanoribbons (rGONRs) were synthesized by longitudinal unzipping of MWCNTs [228]. Generally, 150 mg of MWCNTs were steadily added in concentrated 150 ml of  $\text{H}_2\text{SO}_4$  and stirrer for 24 h, tailed by the addition of 750 mg of  $\text{KMnO}_4$  with stirring in oil bath, after this, a solution of 60 ml of 30%  $\text{H}_2\text{O}_2$  and 300 ml deionized water (DI) was added. Achieved mixture was washed with 60 ml of 10% HCl solution, and then filtered. Ensuing product was dissolved in 50 ml of ethanol and followed by ultra-sonication (750 W) for one hour. For exfoliation of obtained black dispersion mixture was washed several times with 50 ml diethyl ether. Resulting product was washed with distilled water to obtain neutral pH and desiccate in oven at 60  $^\circ\text{C}$  for 20 h without air. Moreover, synthesis process of oxidized graphene nanoribbons was shown in **Figure 3.1**.

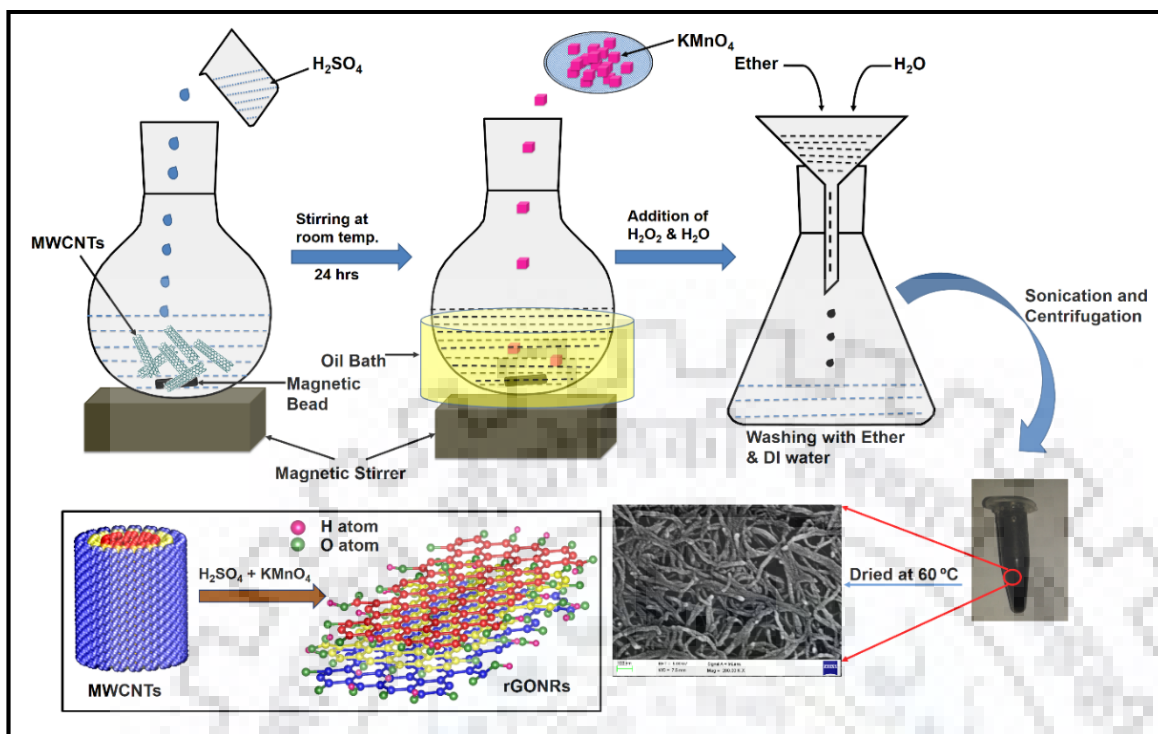


**Figure 3.1.** Schematic diagram of synthesis process for rGONRs from unzipping of MWCNTs through chemical treatment

### 3.2.2 Fluorinated – Graphene Nanoribbons

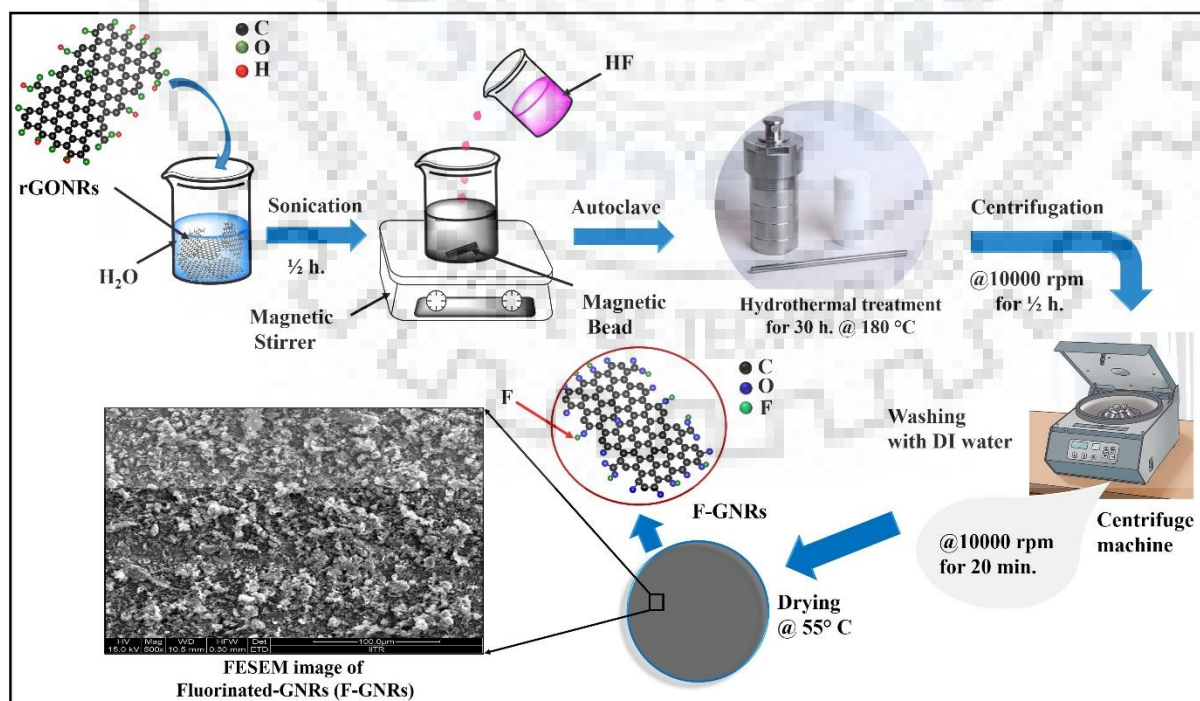


**Figure 3.2.** Schematic diagram of synthesis process for F-GNRs through chemical route



The synthesis procedure as indicated in **Figure 3.2** of fluorinated-graphene nanoribbons (F-GNRs) is discussed in brief. A certain amount of rGONRs are dispersed in 100 ml of deionized (DI) water by probe sonication for 30 min. A black coloured homogeneous solution is prepared. Then, 1 ml hydrofluoric acid (HF) is gradually added under vigorous stirring. The obtained solution is transfer into Teflon lined container and followed by hydrothermal treatment at 180 °C for 30 h. Thereafter homogeneous mixture is separated through centrifugation at 10000 rpm for 30 min. After that, sediment is washed with DI water several times through centrifuge at 10000 rpm for 20 min at room temperature. Finally, a black coloured precipitate is collected in petridish followed by vacuum drying in oven at 55 °C for 24 h before using further.

### 3.3 Fabrication of thin film

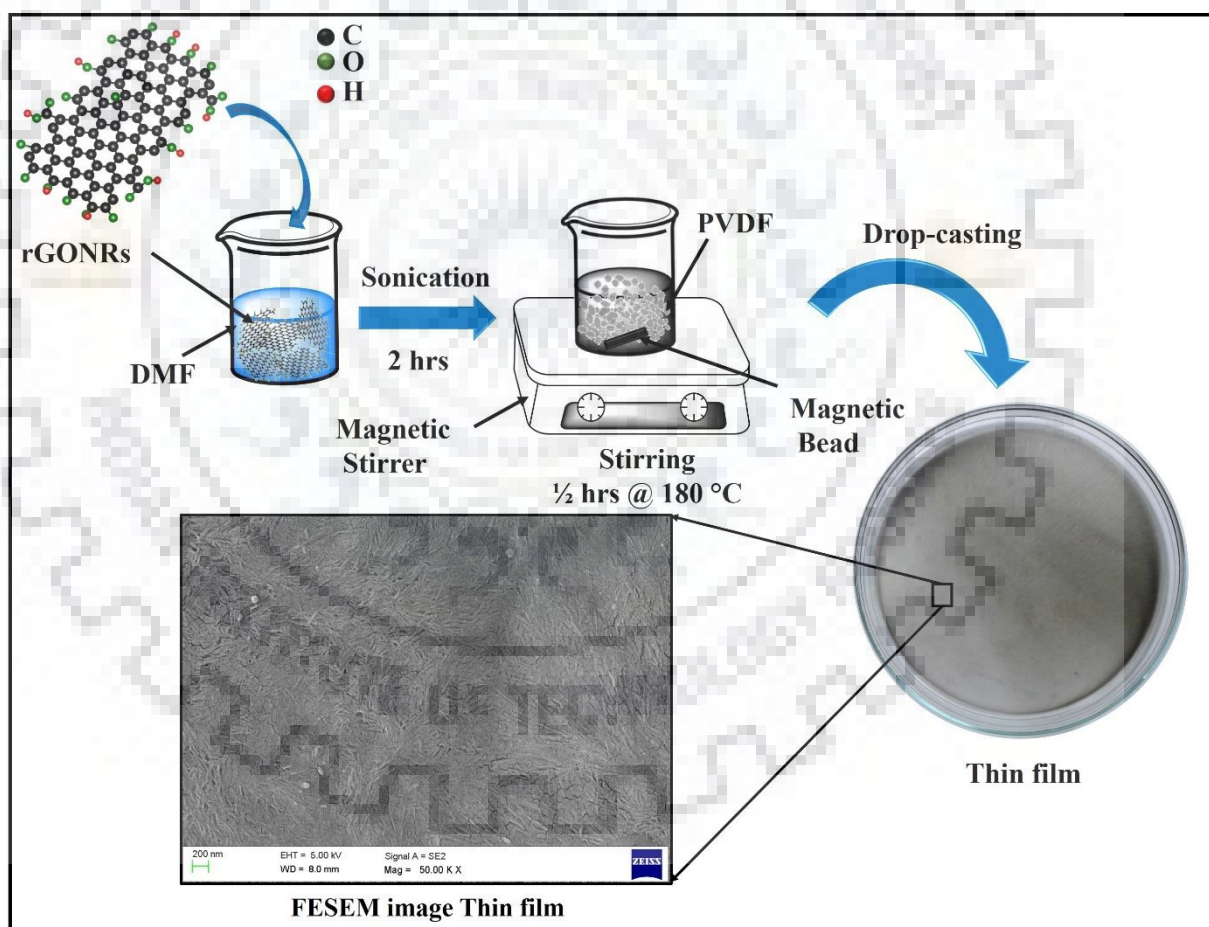


**Figure 3.3.** Schematic diagram of fabrication process for rGONRs/PVDF thin film

The thin film of rGONRs/PVDF was obtained by taking 97 wt% of rGONRs, which were dispersed in DMF through ultra-sonicator for 2 h and say solution P1. On the other hand, 3 wt% of PVDF polymer as a binder was dissolved in organic solvent (DMF) solution at 150 °C and stirred for 30 minutes and followed by the gradually addition of solution P1. Resulting mixture was used for preparation of thin film through drop casting technique and the thin film was prepared as shown in **Figure 3.3**.

### 3.4 Fabrications of nanofibers

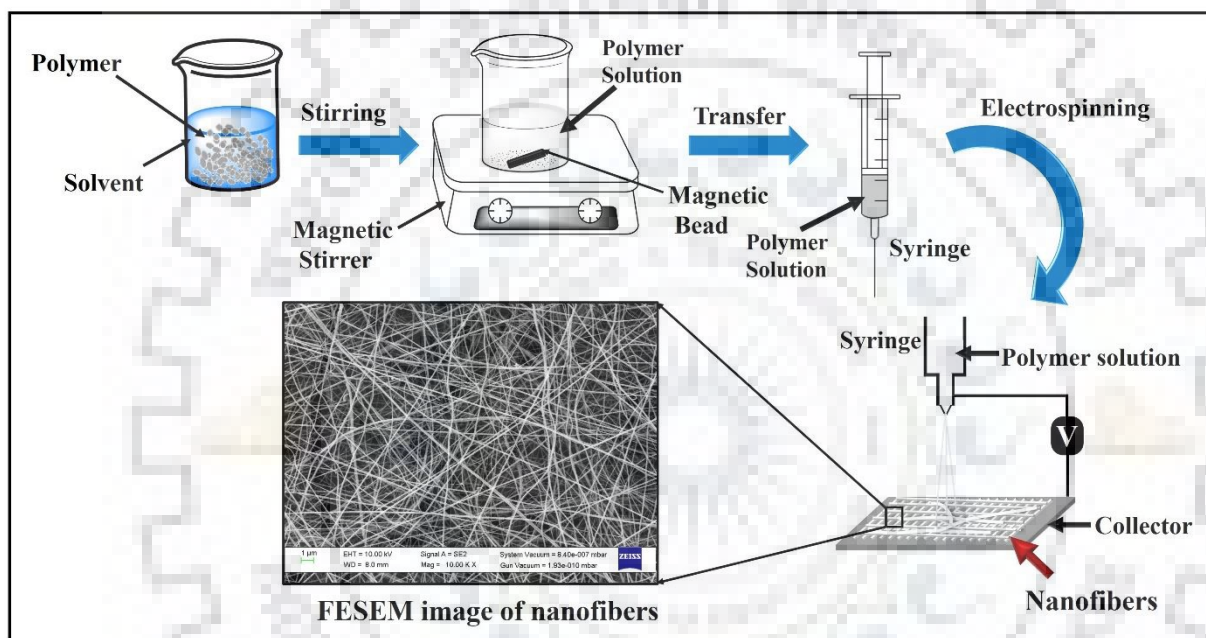


**Figure 3.4.** Schematic diagram of fabrication process of nanofibers

#### 3.4.1 Polyamide 6,6 (nylon) nanofibers

The certain amount of nylon granules was added in 10 ml of formic acid during vigorous stirring for 4 hrs at room temperature to obtain white coloured homogenous mixture. The prepared viscous solution was electro-spun through a metal needle of 2 ml syringe using electro-spinning with distance of 20 cm between tip and collector (TCD). By varying the feeding rate of solution with 20 KV as voltage between the grounded collector and the needle tip, we have optimized the parameters for fabrication of nylon nanofibers. The optimized parameters are shown in the **Table 3.1**. Finally, nylon nanofibers mat is collected on an aluminium foil as displayed in **Figure 3.4**.

**Table 3.1.** Various used electrospinning parameters for optimization of nylon nanofibers fabrication

S. No.	Polymer (Nylon) (in grams)	Feed Rate (ml h <sup>-1</sup> )	Tip-to-collector distance (TCD) (cm)	Voltage (KV)	Results
1.	2.20	0.5	20	20	Broken and non-uniform nanofibers ( <b>Figure 3.5</b> )
2.	2.70	0.4	20	20	Nanofibers with almost uniform thickness ( <b>Figure 3.6</b> )

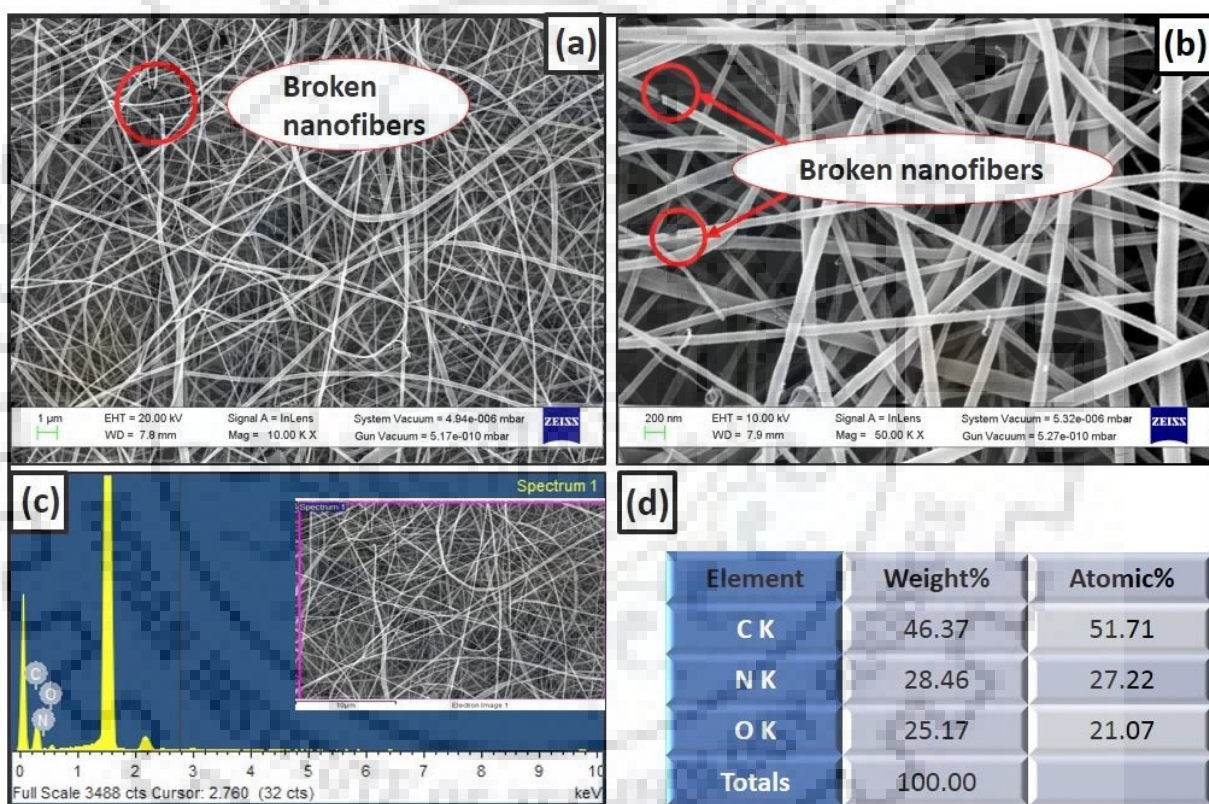


**Figure 3.5.** (a & b) FESEM images of nylon nanofibers with optimization parameters (feed rate = 0.5 ml h<sup>-1</sup>, TCD = 20 cm, voltage = 20 KV) at low and high magnifications, respectively (c) EDAX analysis of inset nylon nanofibers (d) Composition of the various elements (C, N, O) present in nylon nanofibers.

As we have mentioned the optimization parameters in Table 3.1, the quantity of nylon granules is 2.20 grams, feed rate is 0.5 ml h<sup>-1</sup>, TCD is 20 cm and Voltage is 20 KV. By

considering all these parameters, nylon nanofibers have been fabricated, but the obtained nanofibers are broken and non-uniform as shown in the obtained FESEM images (**Figure 3.5 (a) and (b)**). From Figure 3.5, it is clearly revealed that fabricated nanofibers are broken and have non-uniform thickness, which are not considered in further fabrication of TENG. **Figure 3.5 (c) and (d)** show the EDAX analysis and composition of different elements existing in the nylon nanofibers, respectively.

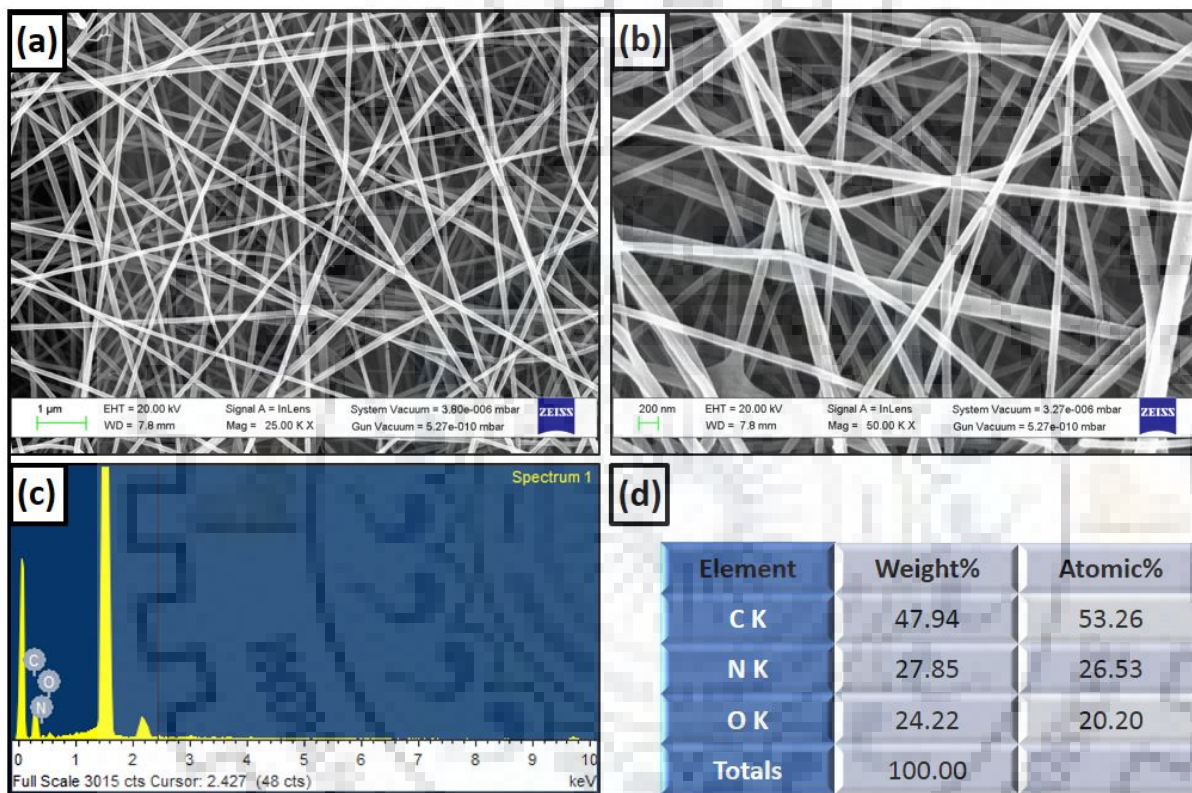


**Figure 3.6.** (a & b) FESEM images of nylon nanofibers with optimization parameters (feed rate = 0.4 ml h<sup>-1</sup>, TCD = 20 cm, voltage = 20 KV), at low and high resolutions, respectively (c) EDAX analysis (d) Composition of the various elements (C, N, O) present in Nylon nanofibers.

Further, by varying the quantity of nylon granules (2.70 grams) and feed rate (0.4 ml h<sup>-1</sup>) are considered, other parameters are same as before, then obtained nylon nanofibers are of uniform thickness as depicted in obtained FESEM images (**Figure 3.6 (a) and (b)**). **Figure 3.6 (c)** shows the EDAX of the nylon nanofibers and **Figure 3.6 (d)** displays the composition of various elements present in the fabricated nylon nanofibers.

### 3.4.2 PVDF nanofibers

For preparation of PVDF homogeneous solution, 1g PVDF was added in the mixture solution of acetone and DMAc (2:3) during vigorous stirring at 120 °C for 12 hrs. Then, electrospinning of the as-prepared viscous solution was performed using 2 ml syringe with a metal needle and varying distance between tip and collector, feeding rate and voltage between the needle tip and grounded collector as shown in **Table 3.2**. The fabricated PVDF nanofibers are collected on an aluminium foil.

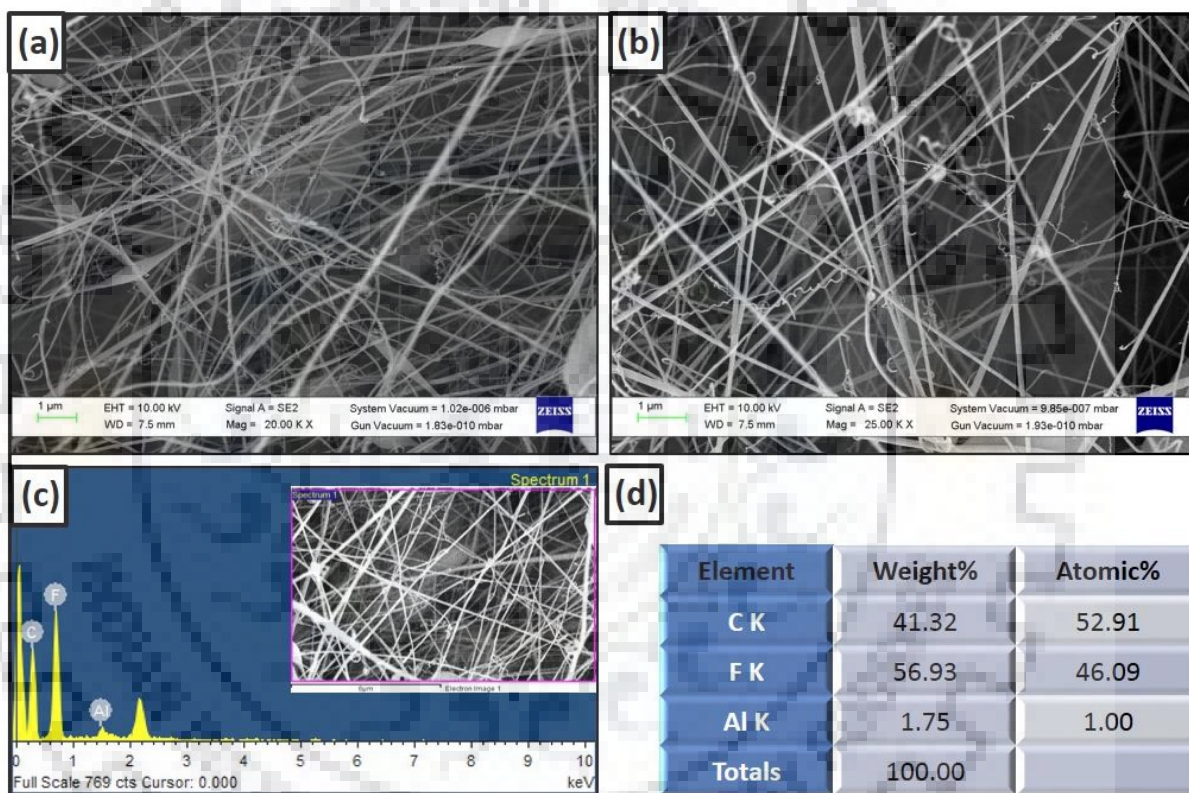


**Figure 3.7.** (a & b) FESEM images of PVDF nanofibers with optimization parameters (feed rate = 0.5 ml h<sup>-1</sup>, TCD = 15 cm, voltage = 11 KV) (c) EDAX analysis corresponding to inset PVDF nanofibers (d) Composition of the various elements (C, F, Al) present in PVDF nanofibers, here Al is present due to aluminium foil substrate, which was used to collect nanofibers during electrospinning.

Table 3.2 shows the different parameters considered for the fabrication of PVDF nanofibers. Herein, the quantity of PVDF granules is fixed to be 1 gram, but the feed rate is considered to be 0.5 ml h<sup>-1</sup>, TCD is 15 cm and Voltage is 11 KV. By taking all these parameters,

PVDF nanofibers have been fabricated, but the obtained nanofibers are non-uniform as confirmed from the obtained surface morphology (**Figure 3.7**). **Figure 3.7 (a) and (b)** shows the obtained FESEM images of fabricated PVDF nanofibers, respectively. **Figure 3.7 (c) and (d)** shows the EDAX analysis composition of various element presence corresponding inset micrograph, respectively.

Further, by varying the parameters like feed rate to  $0.8 \text{ ml h}^{-1}$ , TCD to 10 cm and Voltage to 12 KV, the nanofibers with almost uniform thickness are fabricated as revealed from the obtained FESEM image (**Figure 3.8**). The FESEM images of fabricated PVDF nanofibers at high magnification are shown in **Figure 3.8 (a) and (b)**, respectively. The EDAX and composition of various elements of the PVDF nanofibers are depicted in **Figure 3.8 (c) and (d)**, respectively.

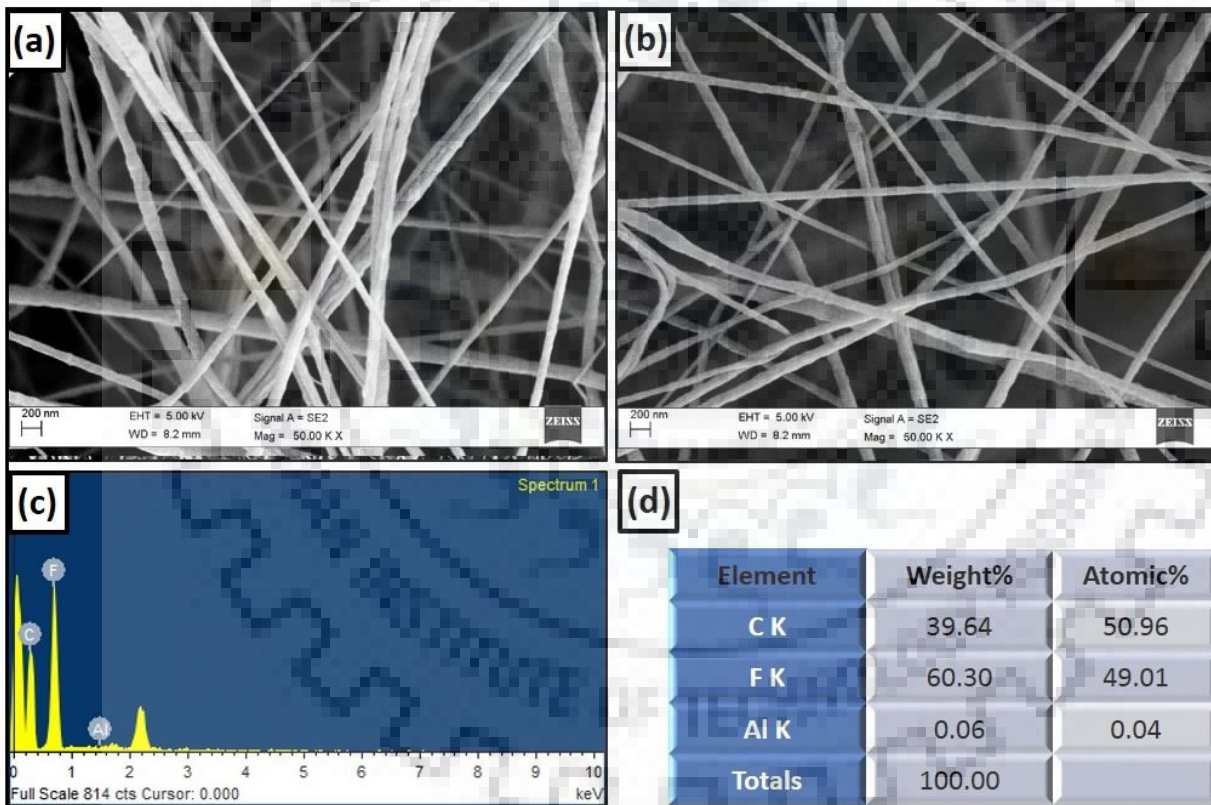


**Figure 3.8.** (a & b) FESEM images of PVDF nanofibers with optimization parameters (feed rate =  $0.8 \text{ ml h}^{-1}$ , TCD = 10 cm, voltage = 12 KV) at high resolutions, (c) EDAX analysis (d) Composition of the various elements (C, F, Al) present in PVDF nanofibers, here Al foil is used to collect nanofibers during electrospinning

**Table 3.2.** Various optimization parameters for the fabrication of PVDF nanofibers

S. No.	Feed Rate (ml h <sup>-1</sup> )	Tip-to-collector distance (TCD) (cm)	Voltage (KV)	Results
1.	0.5	15	11	Non-uniform nanofibers ( <b>Figure 3.7</b> )
2.	0.8	10	12	Nanofibers with almost uniform thickness ( <b>Figure 3.8</b> )

### 3.4.3 PVDF/F-GNRs composite nanofibers

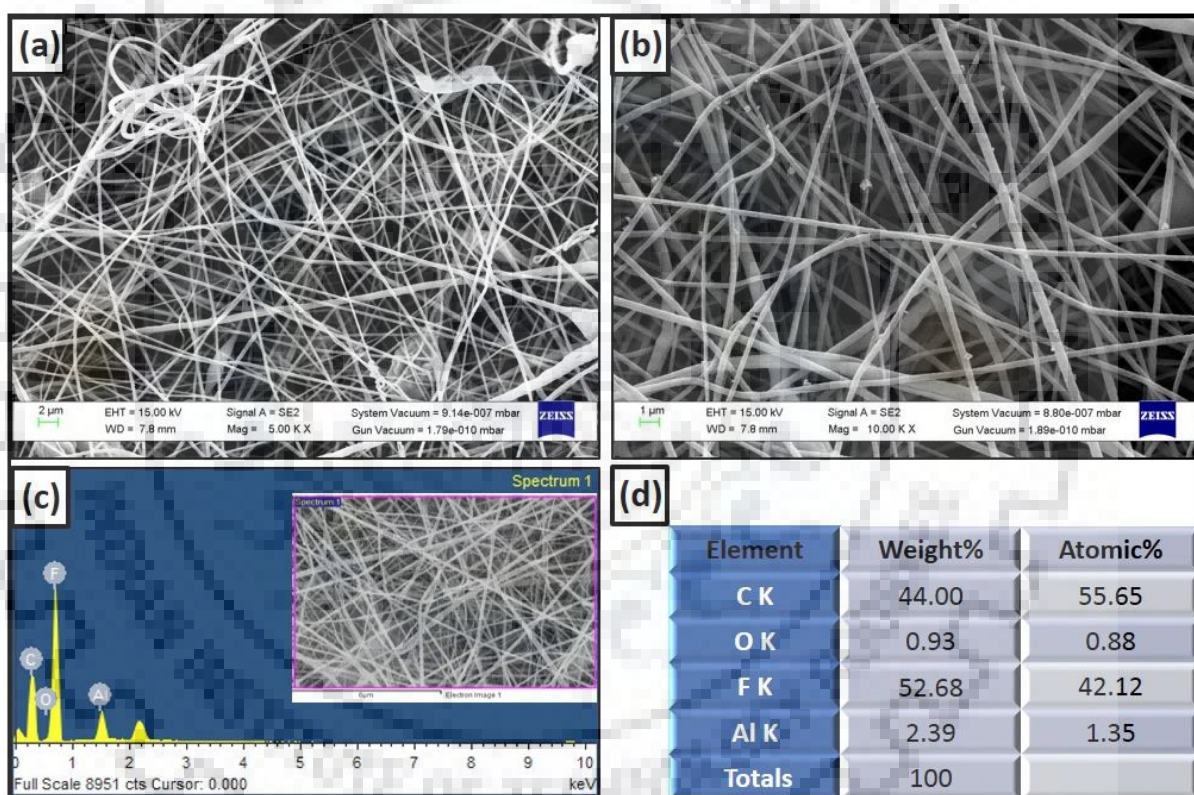


**Figure 3.9.** (a & b) FESEM images of PVDF/F-GNRs nanofibers with optimization parameters (feed rate = 0.8 ml h<sup>-1</sup>, TCD = 10 cm, voltage = 12 KV) at low and high resolutions, respectively (c) EDAX analysis corresponding to inset of PVDF/F-GNRs nanofibers (d) Composition of the various elements (C, F, O, Al) present in PVDF/F-GNRs nanofibers, here Al foil is used to collect nanofibers during electrospinning.

For fabricating the PVDF/F-GNRs composite nanofibers, 0.1 wt% of F-GNRs (1 mg) was dispersed in mixture solution (10 ml) of acetone and DMAc (2:3) using probe sonicator for 20 min at room temperature. Thereafter, certain amount (1 g) of PVDF was added in the prepared solution and followed by magnetic stirring at 120°C for 12 hrs. The obtained black coloured homogenous viscous solution obtained, which was further used in electro-spinning process. Fabrication of PVDF/F-GNRs nanofibers were performed by varying feed rate at 15 KV of voltage between the needle tip and ground collector of 10 cm as shown in **Table 3.3** Finally, fabricated mat of PVDF/F-GNRs nanofibers are collected on an aluminium foil.

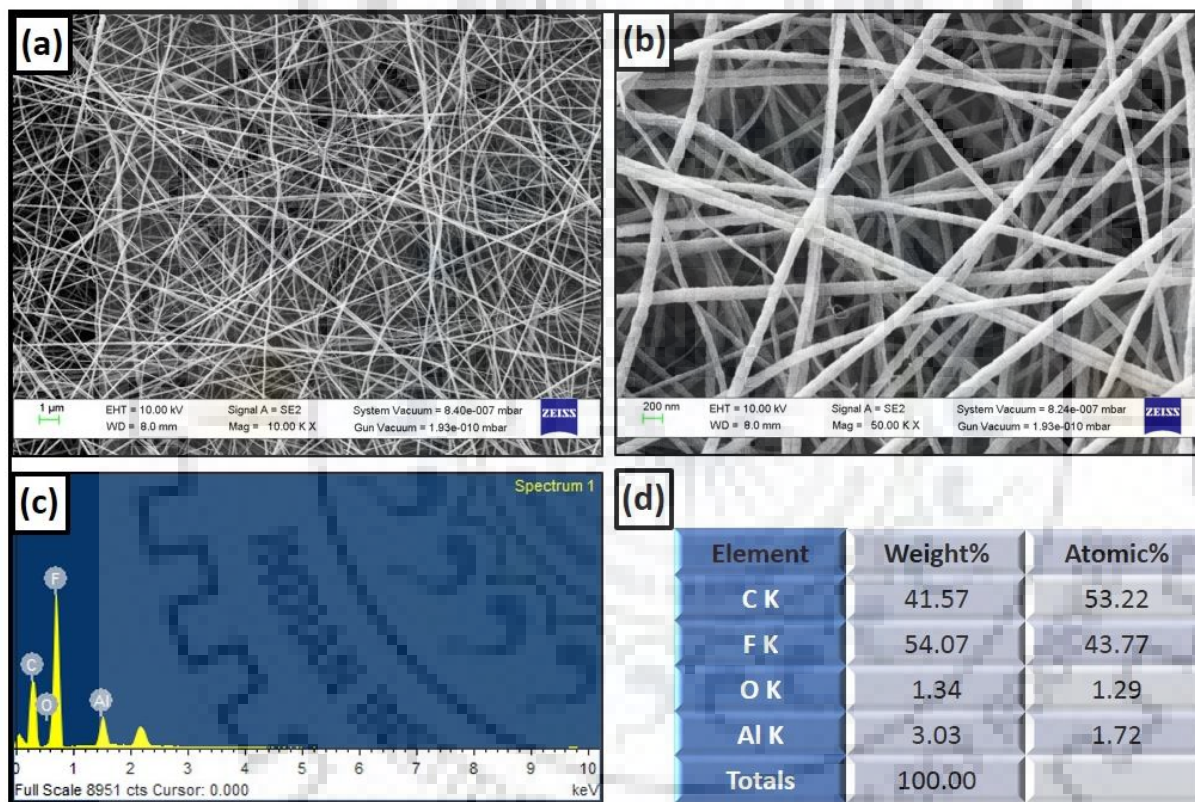


**Figure 3.10.** (a & b) FESEM images of PVDF/F-GNRs nanofibers with optimization parameters (feed rate = 0.3 ml h<sup>-1</sup>, TCD = 10 cm, voltage = 15 KV) low and high resolutions, respectively (c) EDAX analysis (d) Composition of the various elements (C, F, O, and Al) present in PVDF/F-GNRs nanofibers, here Al foil was used to collect nanofibers during electrospinning

When the feed rate is fixed to be 0.6 ml h<sup>-1</sup>, and other parameters such as voltage and TCD to be 15 KV and 10 cm, respectively are considered, the fabricated PVDF/F-GNRs nanofibers with non-uniform thickness and beads were confirmed from the obtained FESEM



images (**Figure 3.9 (a) and (b)**). **Figure 3.9 (c) and (d)** show EDAX analysis composition of various element presence corresponding inset micrograph, respectively.

Further, we have changed feed rate to be  $0.3 \text{ ml h}^{-1}$  and kept other parameters including TCD and voltage are same, fabricated PVDF/F-GNRs nanofibers are of uniform thickness as shown in the obtained FESEM images (**Figure 3.10 (a) and (b)**), respectively. The EDAX and composition of various elements of the PVDF/F-GNRs nanofibers are displayed in **Figure 3.10 (c) and (d)**, respectively.

**Table 3.3.** Various optimization parameters for the fabrication of PVDF/F-GNRs nanofibers

S. No.	Feed Rate ( $\text{ml h}^{-1}$ )	Tip-to-collector distance (TCD) (cm)	Voltage (KV)	Results
1.	0.6	10	15	Clusters of nanofibers formed and non-uniform ( <b>Figure 3.9</b> )
2.	0.3	10	15	Nanofibers with uniform thickness ( <b>Figure 3.10</b> )

### 3.5 Characterization Techniques and Instruments

#### 3.5.1 Material Characterizations

The synthesized materials are explored with diverse powerful characterization techniques such as: Diffraction patterns of the synthesized samples and composites are obtained in the range of  $10^\circ$  to  $80^\circ$  (scan rate =  $0.2^\circ/\text{min}$ ) using Bruker AXS Diffractometer D8 advance Cu  $K\alpha$  radiation ( $\lambda = 1.54 \text{ \AA}$ ). The morphological analysis of prepared samples with EDAX analysis and corresponding elemental mapping are done using Field Emission Scanning Electron Microscope (FE-SEM, Zeiss-Ultra Plus Gemini Co.). Further for examining the internal structure of the nanofillers, high-resolution transmission electron microscopy (HRTEM, TECNAI G2 20 S-TWIN (FEI Netherlands)), which is operated at 200 kV as an accelerating voltage. The Various functional groups present in the synthesized materials are examined with Fourier Transformation Infrared Spectrophotometer (FTIR, Thermo Scientific Nicolet 6700). The samples are prepared by mixing the small amount of sample in KBr and making pellet using bolt press. Then place that pellet in the FTIR instrument to obtain spectra. Raman spectrum is found using Invia Renishaw

Raman spectrophotometer with argon ion laser (Excitation wavelength = 514 nm). For three dimensional topographical image of the synthesised samples, Atomic force microscopy (AFM, NT-MDT NTEGRA) is done in contact mode. For potentiodynamic electrochemical measurements, cyclic voltammetry (CV, EC epsilon) is performed.

### 3.5.2 Nanogenerator Characterization

The electrical measurements such as open circuit voltage ( $V_{OC}$ ) and short circuit current ( $I_{SC}$ ) of the fabricated triboelectric nanogenerator are measured using digital multimeter and picoammeter, respectively as shown in **Figure 3.11**. Moreover, applied pressure on TENG is measured using pressure sensor.

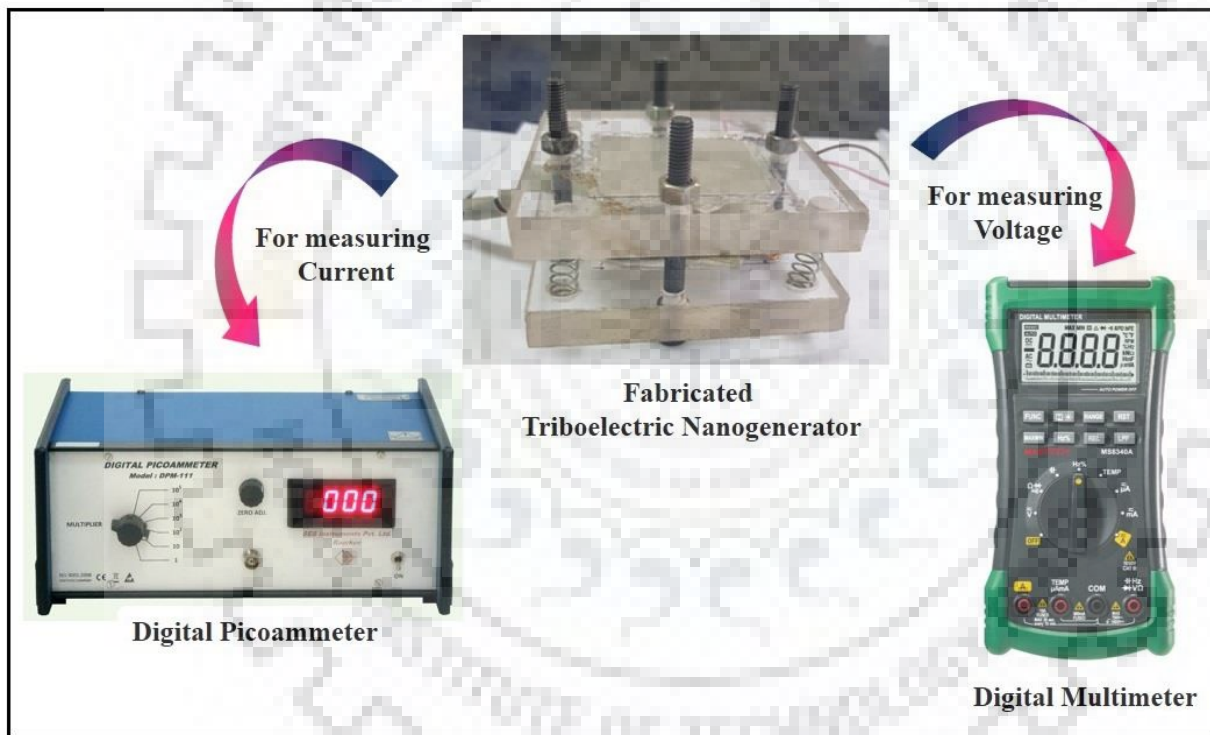


**Figure 3.11.** Electrical outputs (Current and Voltage) of fabricated TENG in initial position or without hand pressing.



## Chapter 4

# RESULTS AND DISCUSSION

---



## Section 4.1

### Effective energy harvesting from a single electrode based triboelectric nanogenerator

---

rGONRs were synthesized as discussed in the methods and schematic diagram of the synthesis process was illustrated in **Figure. 3.1** (Chapter 3).

#### 4.1.1 X-ray diffraction (XRD) Analysis

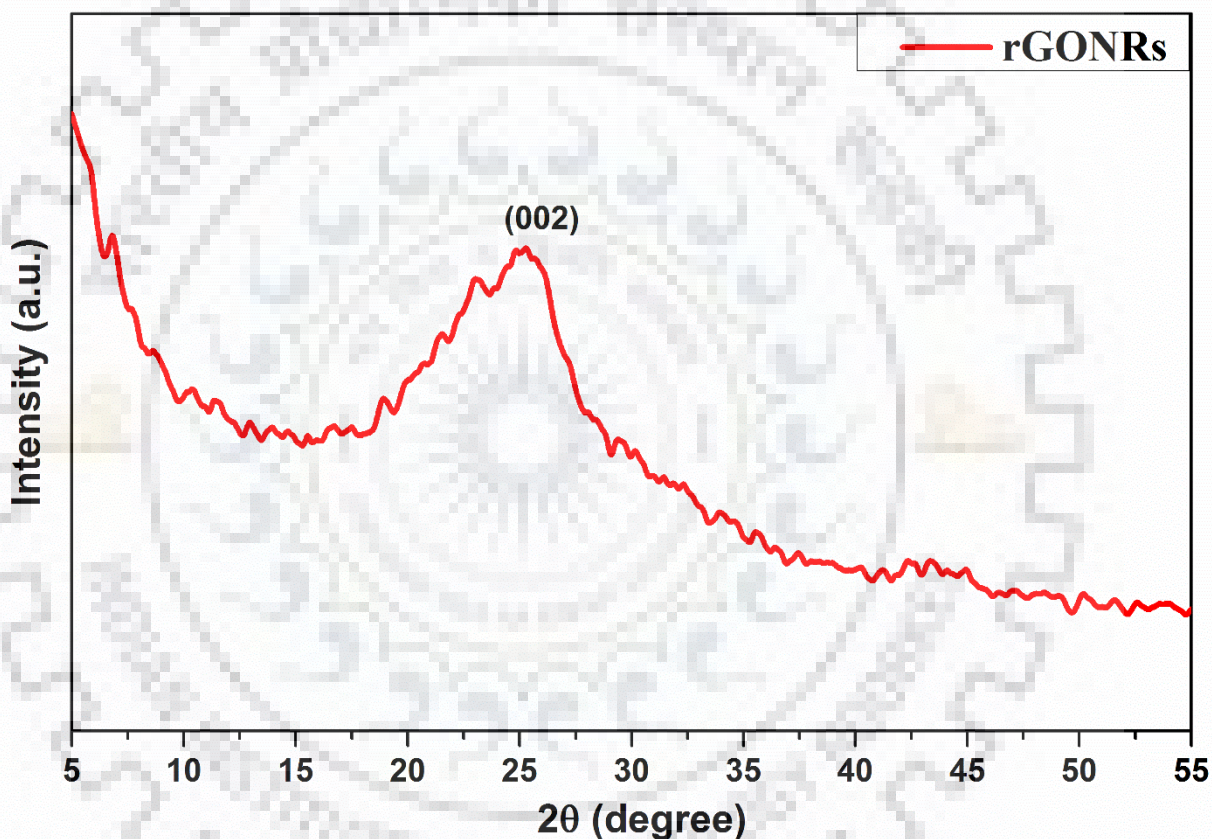


**Figure 4.1.1.** Diffraction pattern of rGONRs

X-ray diffraction (XRD) analysis was performed for the rGONRs and rGONRs/PVDF composite thin film prepared by as illustrated in **Figure 4.1.1** and **Figure 4.1.2**, respectively. The peak around  $26^\circ$  corresponding to (002) planes, confirms the presence of reduced graphene oxide nanoribbons in both the figures. Figure 4.1.2 reveals that the characteristic peaks of PVDF polymer are present around  $17.2^\circ$ ,  $18.3^\circ$ ,  $19.6^\circ$ ,  $38.5^\circ$  and  $44.69^\circ$ , analogous to (100), (020), (110), (131) and (112) planes, respectively, which are in good agreement with the reported

literature [JCPDS No. 42-1650]. In addition, the existence of all individual peaks of both elements indicates that they exist in their original phases and there is no direct interaction which changes the phase of overall product. Therefore, we have considered the combination of these elements as rGONRs/PVDF composite material.

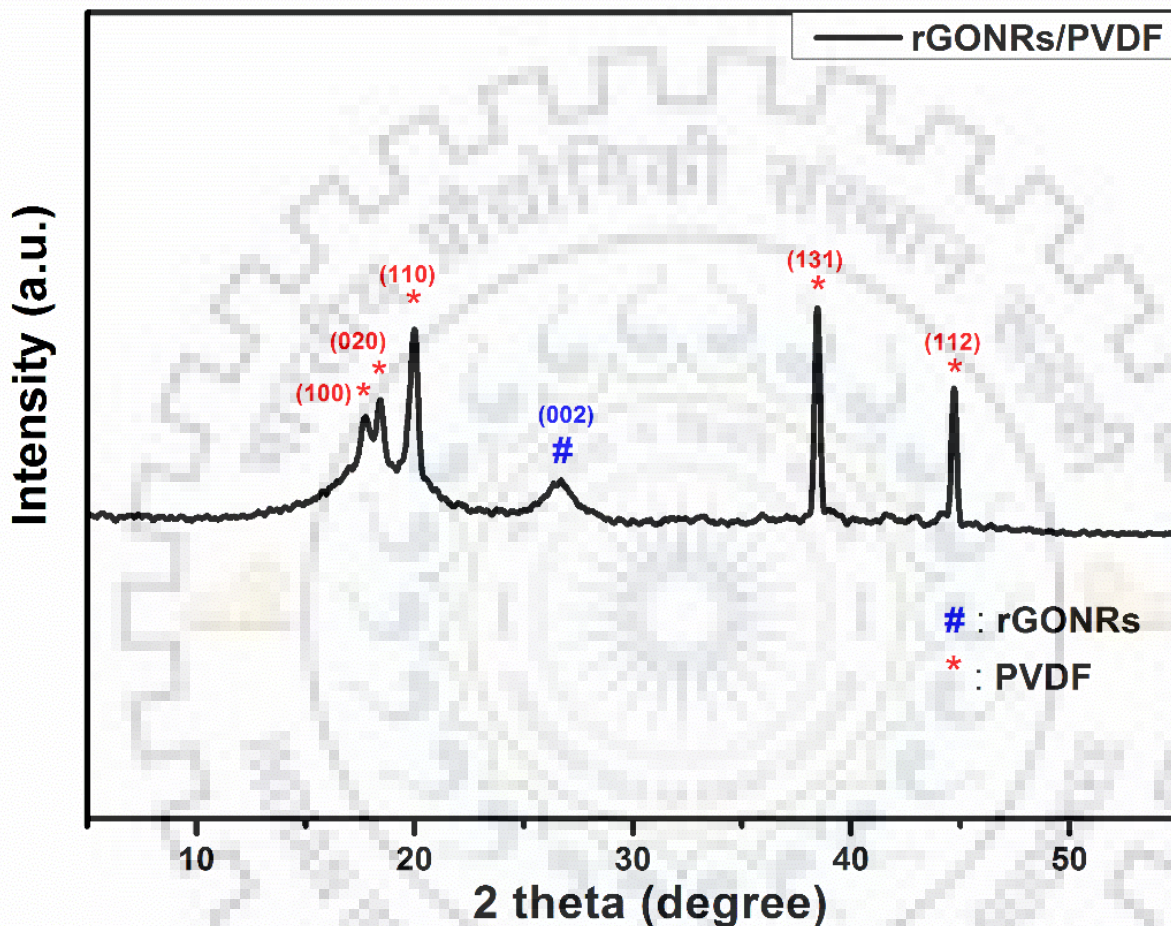
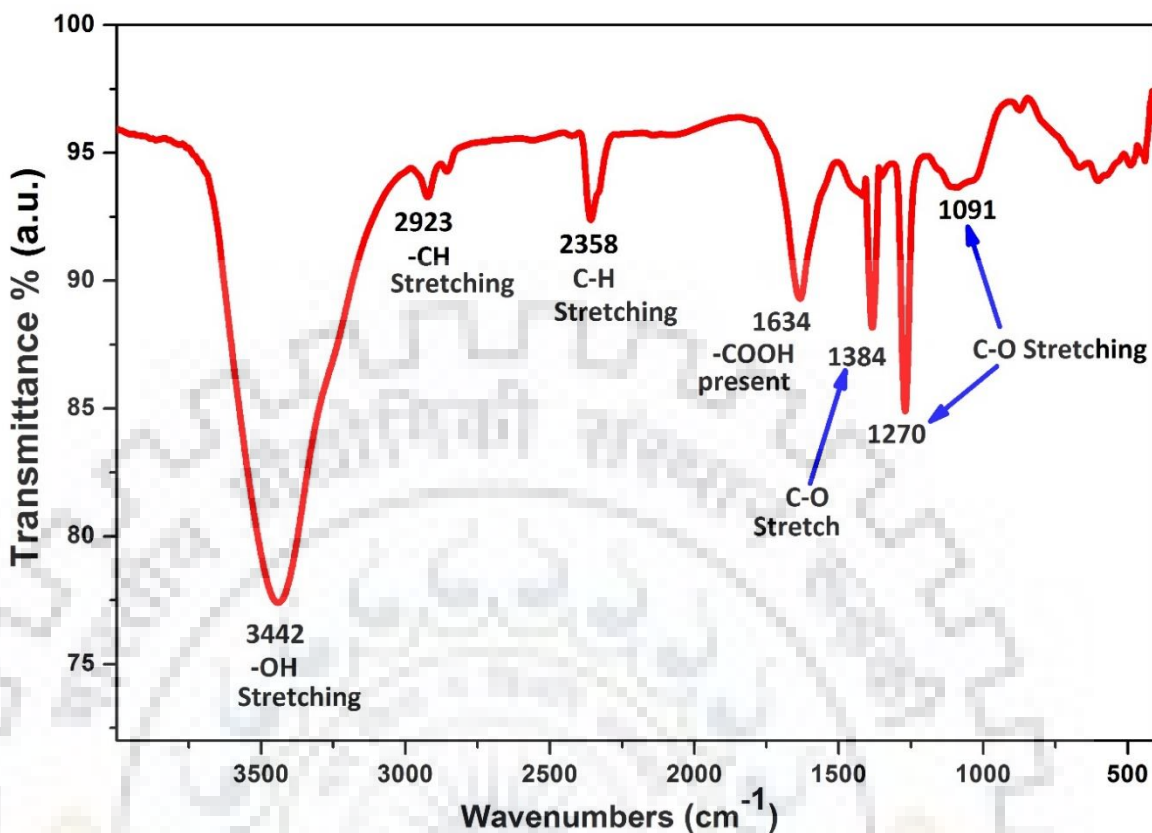


Figure 4.1.2. Diffraction pattern of rGONRs/PVDF thin film

#### 4.1.2 Fourier Transformation Infrared (FTIR) Spectroscopy

The degree of oxidation of graphene nanoribbons from MWCNTs was further illustrated by FTIR Spectroscopy. FTIR spectroscopy (Figure 4.1.3) shows that the -OH stretching was present at  $3442\text{ cm}^{-1}$  in the high frequency range, -CH stretching was confirmed due to  $2923\text{ cm}^{-1}$ ,  $2358\text{ cm}^{-1}$  and carboxylic group (-COOH) existence was verified from  $1634\text{ cm}^{-1}$ . Moreover, -CO stretching would be verified at  $1384$ ,  $1270$  and  $1091\text{ cm}^{-1}$  [229,230].



**Figure 4.1.3.** Fourier transform infrared (FTIR) spectroscopy of rGONRs

#### 4.1.3 Morphological Analysis

Field Emission-Scanning Electron Microscope (FE-SEM) and Transmission Electron Microscope (TEM) images of rGONRs are shown in **Figure 4.1.4 (a)** and **(b)**. These figures demonstrated that CNTs were unzipped completely in the form of oxidized graphene nanoribbons, having ~45 nm width. The elemental analysis is obtained using energy dispersive X-ray analysis (EDAX) of the prepared rGONRs, which confirms the composition by weight% of carbon and oxygen are found 66.20% and 33.80%, respectively (**Figure 4.1.4 (c)**).

#### 4.1.4 Raman Spectroscopy Analysis

Raman spectroscopy of rGONRs/PVDF composite has been shown in **Figure 4.1.5**. The presence of D-band at around 1360 cm<sup>-1</sup> proves the presence of certain defects in the structures of rGONRs. These defects must be due to the presence some vacancies in the hexagonal structure created during opening of MWCNTs. Further, the observed value of I<sub>2D</sub>/I<sub>G</sub> from the Raman spectrum indicates the presence of 2–3 layers stacked together [231].

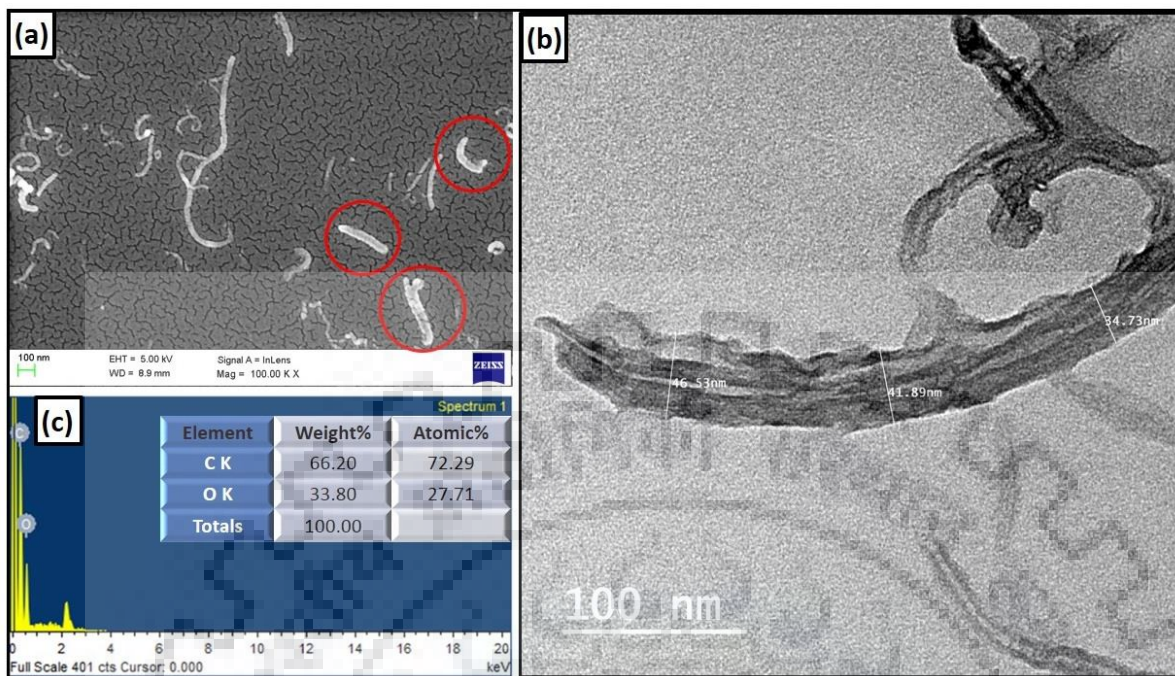


**Figure 4.1.4.** (a) FE-SEM image and (b) TEM image of rGONRs (c) Elemental analysis using energy dispersive X-ray analysis (EDAX) of the prepared rGONRs and the composition of C and O as shown in the inset

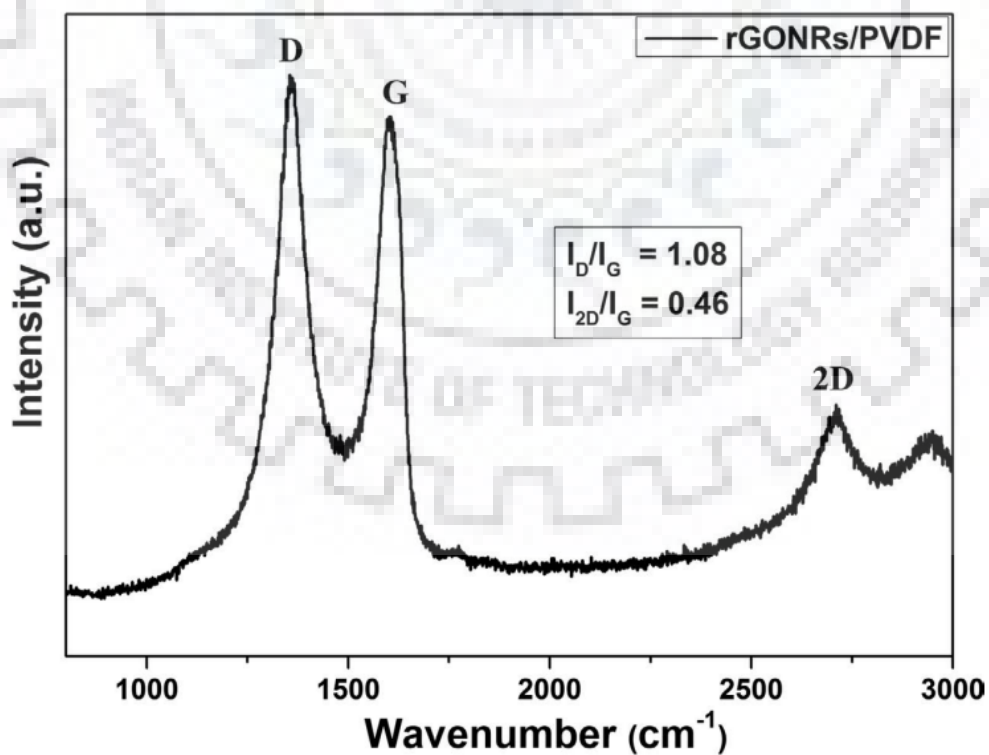


**Figure 4.1.5.** Raman spectra of rGONRs/PVDF thin film



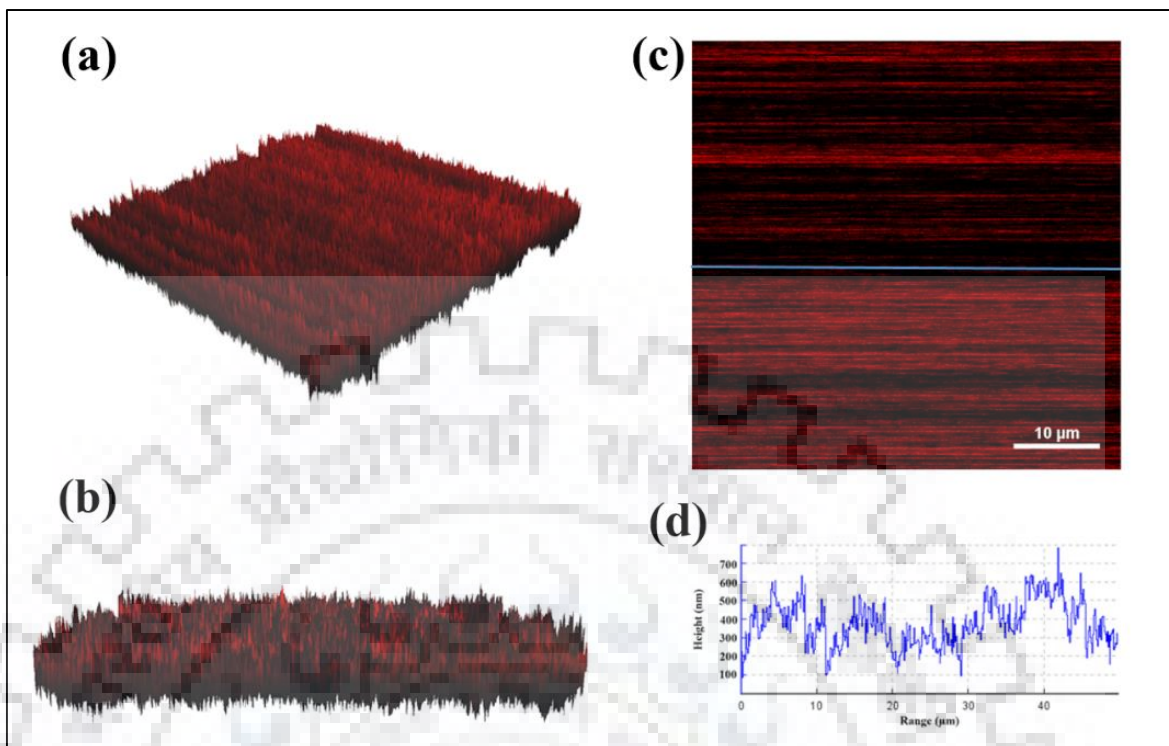


**Figure 4.1.6.** 3D-AFM image of the rGONRs/PVDF thin film (a & b) Side view. (c) Top view. (d) Height profile of thin film

#### 4.1.5 Atomic force microscopy (AFM)

Atomic Force Microscopy (AFM) images of rGONRs/PVDF thin film was shown in **Figure 4.1.6**. In this analysis, we can observe the orientation and 3D topographical information about the sample surface. **Figure 4.1.7** shows the surface profilometry of the pristine rGONRs thin film as well as the rGONRs/PVDF thin film. From Figure 4.1.6, it has been clearly observed that, average surface roughness of rGONRs/PVDF thin film ( $2.21 \mu\text{m}$ ) is higher than rGONRs film ( $2.16 \mu\text{m}$ ). The average surface roughness play vital role to trap charge and enhance charge storage capacity of materials.

#### 4.1.6 Electrochemical Measurements

To extend our investigation, we had also examined the contact resistance by using two - probe resistivity measurement method. **Figure 4.1.8** shows the current voltage (I-V) curve in which the contact resistance for pristine rGONRs have been found  $6.11 \Omega \mu\text{m}^{-2}$ . While,

composite was prepared using PVDF as binder, contact resistance increases upto  $9.32 \Omega \mu\text{m}^{-2}$  because of the presence of functional groups in rGONRs/PVDF composite.

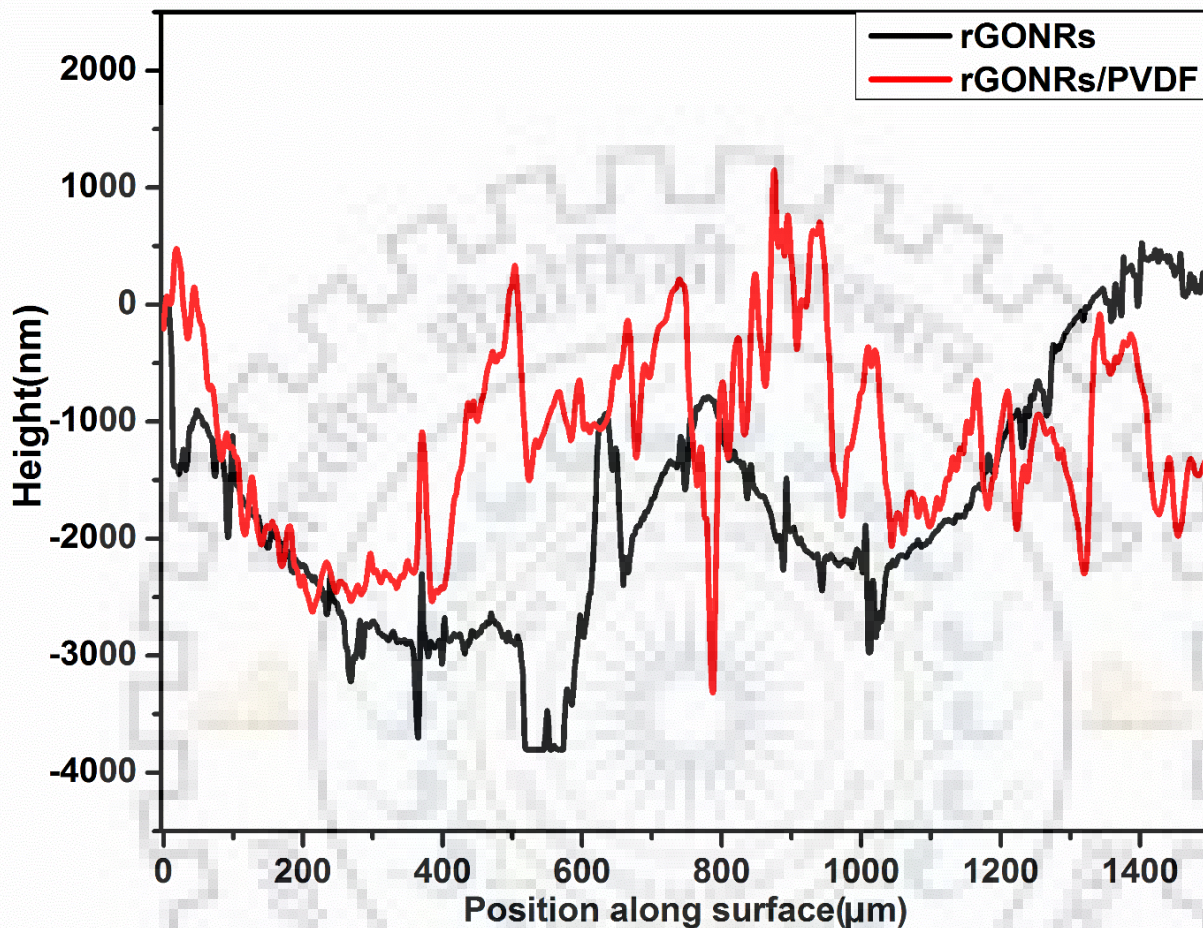


**Figure 4.1.7.** Surface Profilometry analysis has been performed to analyze the surface morphology of the rGONRs thin film and rGONRs/PVDF thin film

The Cyclic Voltammetry (CV) analysis was performed to examine electrochemical performance of the electrodes. CV curve (**Figure 4.1.9**) of prepared sample measured at scan rate of  $100 \text{ mV s}^{-1}$  in 1M DMF with in potential range from -1.5 to +1.5 V. The redox peaks were identified more in rGONRs/PVDF composite in comparison to the pristine rGONRs, which confirm better charge transport of rGONRs/PVDF composite. Moreover, area under the CV curve of rGONRs/PVDF is larger than the pristine rGONRs, so that the charge storage capability of this material is good in comparison to pristine rGONRs, this results are in good agreement with the literature [232].

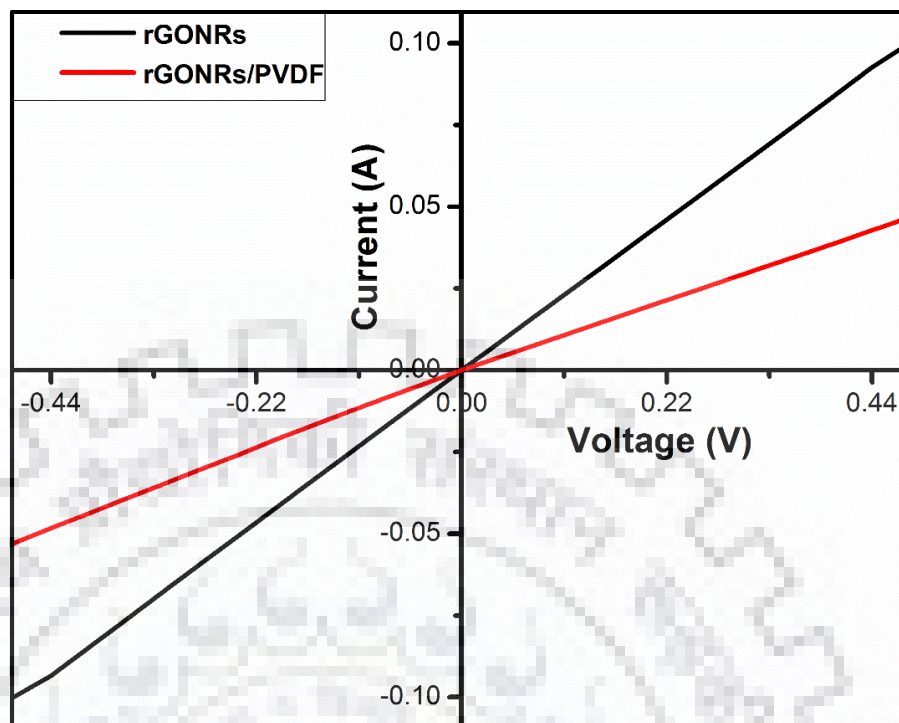


**Figure 4.1.8.** Two probe I-V characteristic measurement of the pristine rGONRs and rGONRs/PVDF composite

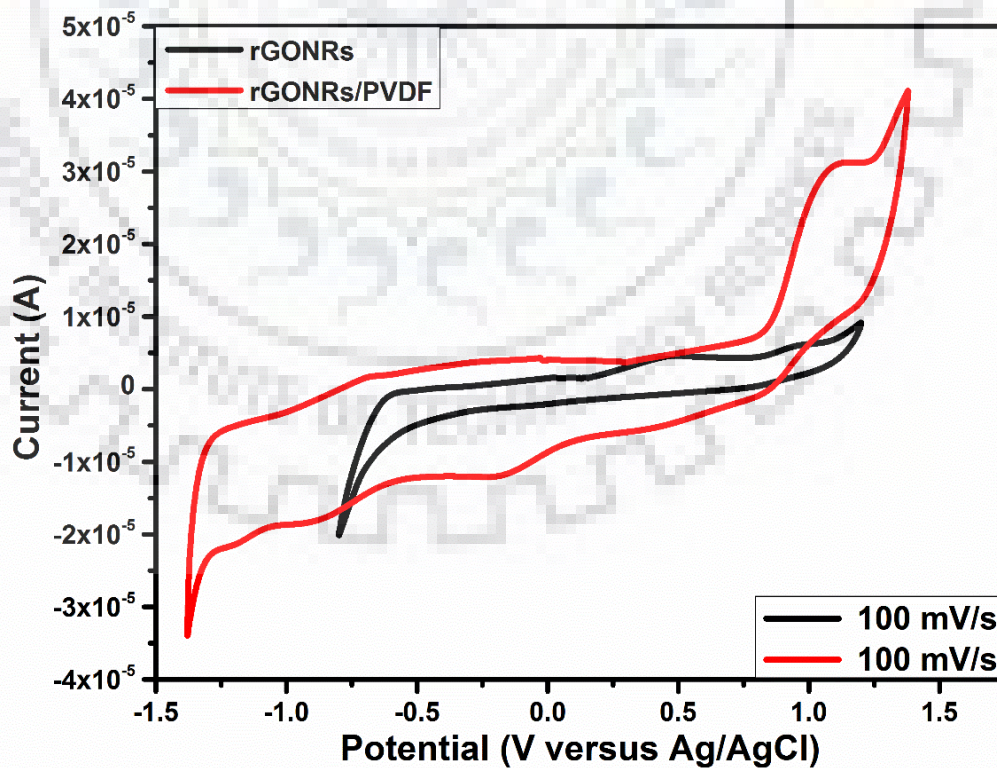


**Figure 4.1.9.** Cyclic voltammetry of the pristine rGONRs and rGONRs/PVDF composite

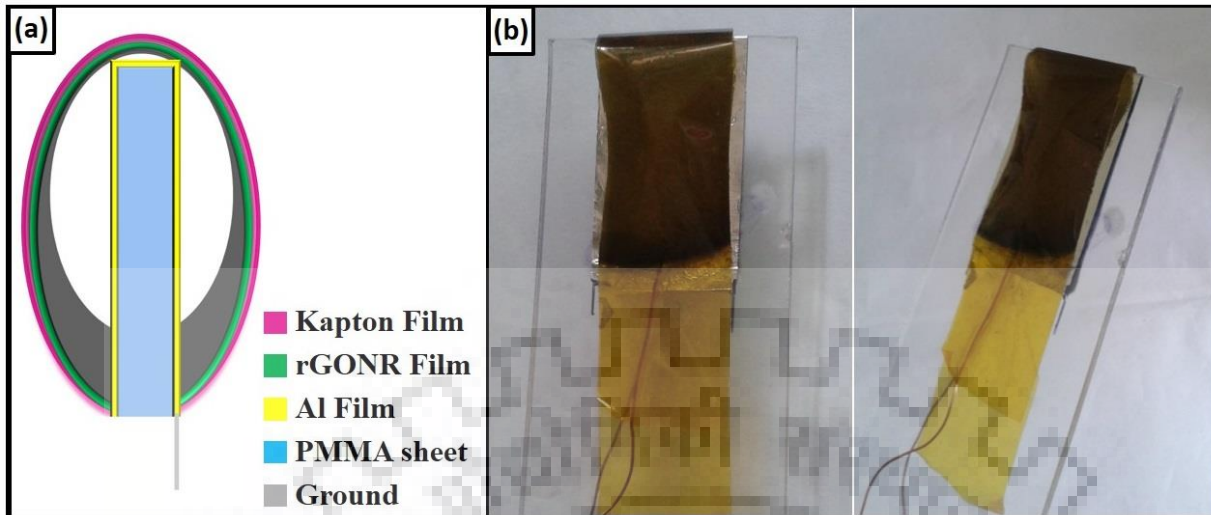


**Figure 4.1.10.** (a) Schematic view of the rGONRs/PVDF based triboelectric nanogenerator (b) Optical images of triboelectric nanogenerator

#### 4.1.7 TENG Fabrication

The schematic diagram of rGONRs/PVDF based triboelectric nanogenerator as shown in **Figure 4.1.10 (a)**. We are using PMMA sheet of 4.5 cm×6 cm as substrate because of its good strength, light weight and acrylic material. The aluminium (Al) membrane of 2.5 cm×4.5 cm was fixed on both sides of substrate which acts as electrode as well as triboelectric surface. A triboelectric thin film of rGONRs/PVDF (1.5 μm) was fixed on kapton film (125 μm). The kapton film was then bent in the arch shape around Al membrane and kapton tape was used to fix it on the PMMA sheet. Herein, TENG was having arch-shaped structure due to which both the films i.e. Al and rGONRs/PVDF thin film were having effective separation between them. **Figure 4.1.10 (b)** shows the optical images of fabricated rGONRs/PVDF based TENG, where one electrode is made ground and from the other we get voltage. These optical images clearly show the arch-shaped structure of TENG. The surface of thin film with uniformly distributed nanoribbons as shown in the optical image (**Figure 4.1.11 (a)**) and the distribution is clearly visible in the FE-SEM image of thin film as shown in **Figure 4.1.11 (b)**.

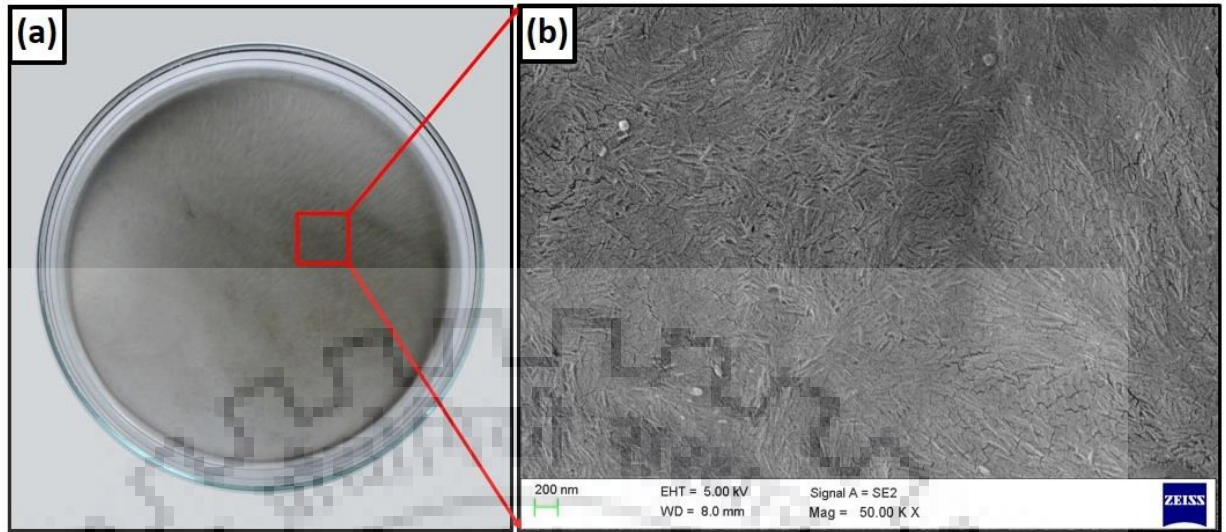


**Figure 4.1.11.** (a) Optical image of rGONRs/PVDF thin film (b) FE-SEM image of thin film of rGONRs/PVDF composite

The obtained rough surface of the thin film would enhance the surface area of the device and due to this the device would give effective output [81]. The rGONRs should be negatively charged because graphene oxide is negative charged as reported [233]. The charge on the rGONRs/PVDF thin film is fixed and confined by kapton tape. The total negative charge ( $Q_{\text{rGONRs}}$ ) of rGONRs/PVDF thin film could induce positive charge in the Al foil. The fabricated device as flat panel capacitor, the capacitance ( $C$ ) of capacitor could be written as  $C = \epsilon S/d$ , where  $\epsilon$ ,  $S$ ,  $d$  and represents dielectric constant of air, surface area of rGONRs/PVDF film and separation distance between rGONRs/PVDF film and Al foil. The output current and voltage could be based on relation as:

$$I(t) = \frac{dQ}{dt} \quad (4.1.1)$$

$$Q = CV \quad (4.1.2)$$

The triboelectric charge density could be increased by having the oxidized graphene nanoribbons on the surface, due to which the effective surface area has been enhanced. Figure 4.1.11 (b) illustrates that the surface of the rGONRs/PVDF thin film was having the uniformly distributed nanoribbons structures.

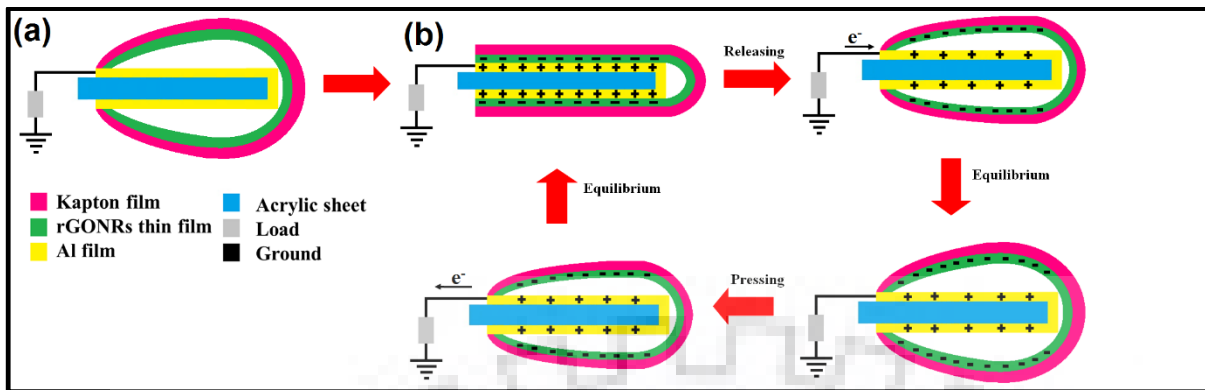


**Figure 4.1.12.** (a) Shows the schematic view of rGONRs/PVDF based single electrode TENG (b) In contact and separation mode, how the electricity is produced by TENG

The working of the rGONRs/PVDF based TENG was performed by applying a mechanical force on the nanogenerator, therefore rGONRs/PVDF thin film and the Al foil can come in contact and released from each other. One of the electrode i.e. Al foil was connected to load resistance of 100 M $\Omega$  and was made ground. Once released, the rGONRs/PVDF thin film and Al would get apart from each other because of the elasticity stored in the kapton film, then come back in its original shape. The rGONRs/PVDF thin film surface was having negative surface electric potential can be upto 0.35 V by persistent contact-separation between the rGONRs/PVDF thin film and Al foil as illustrated in **Figure 4.1.12 (a)**. For measuring the voltage, TENG was connected to low noise voltage pre-amplifier. The output of the rGONRs/PVDF based single electrode TENG by applying the mechanical energy induced by finger touching was having highest voltage as 0.35 V. Moreover, we have removed rGONRs/PVDF thin film from kapton. Now, kapton is a contact surface in the fabricated TENG, corresponding electrical output voltage was found to be 0.16 V. When the compressive force was applied, the TENG would give positive voltage. While, compressive force was released it gave negative voltage, which is clearly depicted in **Figure 4.1.13**.

The mechanism of the rGONRs/PVDF based TENG was schematically depicted as shown in Figure 4.1.12. At the original state, no contact between Al foil and rGONRs/PVDF thin film, there was no electric output and hence no charge transfer across them. Once the Al foil and rGONRs/PVDF thin film surface came in contact with each other, electrons were injected from Al foil into rGONRs/PVDF thin film due to the presence of negative charge on itself. According

to the triboelectric series, Al is having more propensity to loss electrons and hence according to electrostatic phenomena more tribo-electrically positive than rGONRs/PVDF thin film [198].

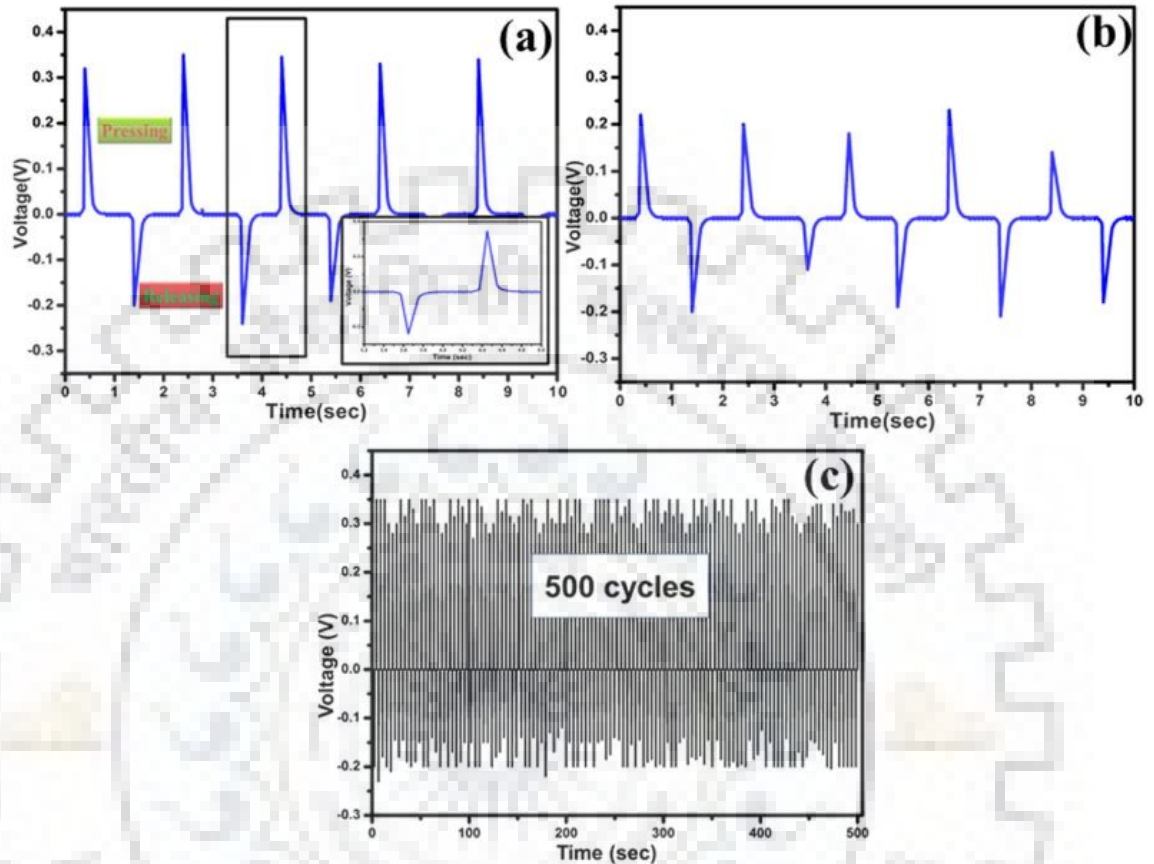


**Figure 4.1.13.** (a) Output voltage of the rGONRs/PVDF based triboelectric nanogenerator (b) Output voltage of kapton tape TENG (c) Shows that the rGONRs/PVDF based TENG was quite stable up to 500 cycles

If the size of the rGONRs/PVDF thin film and Al foil was definite then the positive triboelectric charges, which were generated on the Al foil may drift to the ground through external load, giving electric field leakage. By releasing the mechanical force, TENG would instantly come back to its initial shape because of the flexibility present in the kapton tape. As the gap formed between the rGONRs/PVDF thin film and Al with definite size would be increasing, the triboelectric positive charge formed on the Al film was decreasing, which offers the flow of electrons from Al film to the ground. However, when the mechanical energy is applied again on the TENG to come in contact with each other i.e. Al and rGONRs/PVDF thin film, then induced triboelectric negative charges on the rGONRs/PVDF thin film would be increasing to

balance the triboelectric positive charges on the Al foil and hence electrons would flow from ground into the Al foil. The full contact-separation cycle of electricity generation would be shown in Figure 4.1.12 (b).

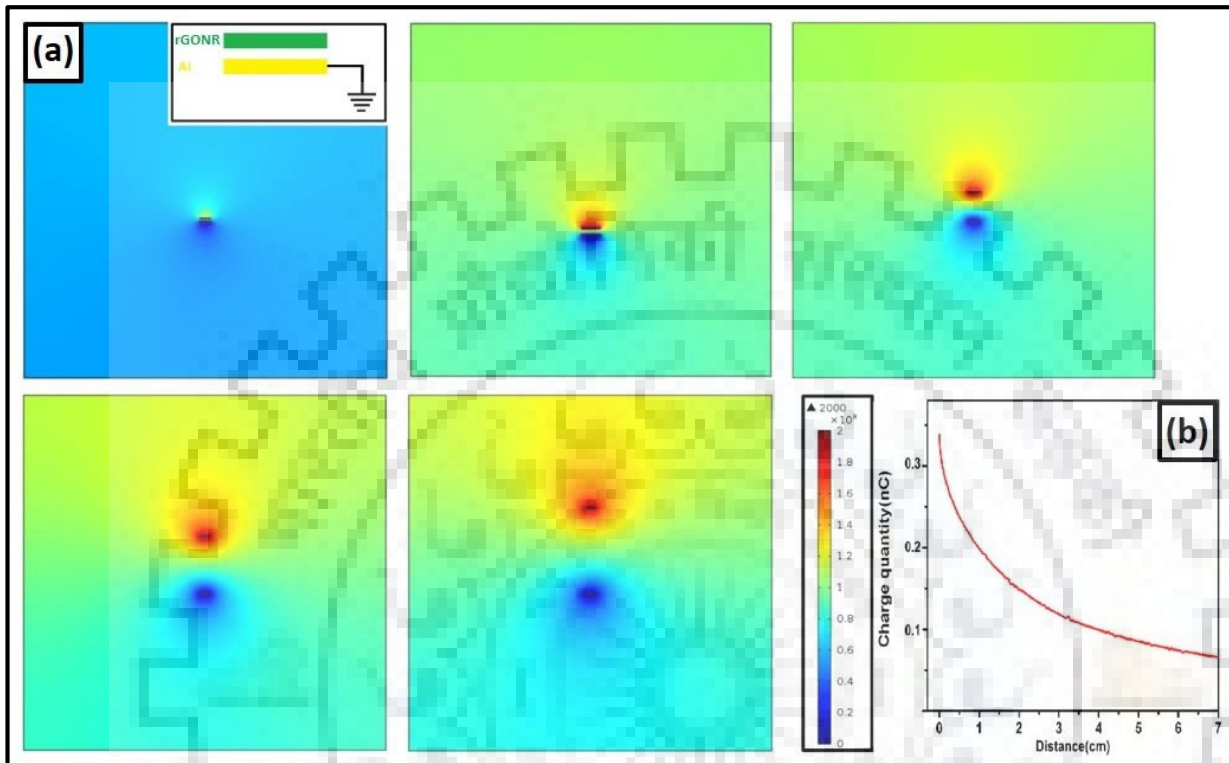


**Figure 4.1.14.** (a) COMSOL simulations for potential distribution at different gap distances 0.2, 3, 6, 9 and 12 cm, respectively between rGONRs/PVDF thin film and Al foil. The inset shows the model for the calculation (b) Charges produced on the Al foil are decreasing by increasing the gap distance between rGONRs/PVDF film and Al foil

In order to further understand the working principle of the as prepared rGONRs/PVDF based single electrode TENG, numerical analysis was investigated through numerical simulation based on COMSOL Multiphysics as shown in **Figure 4.1.14 (a)**. The model was constructed same as prepared experimentally, which based on Al foil and rGONRs/PVDF thin film with same size of  $3 \times 4.5 \times 0.05 \text{ cm}^3$ . **Figure 4.1.14 (b)** illustrates the calculations, which were performed and results in the electric potential distribution with the distance of 0.2, 3, 6, 9 and 12 cm, respectively between rGONRs/PVDF and Al foil. However, when the gap distance is increasing, the potential difference between the Al foil and rGONRs/PVDF thin film can increase upto 2000 V. As the gap distance between rGONRs/PVDF film and Al increases the amount of charges present on Al



foil decreases, which indicates electrons were transferred from ground to Al foil as the gap distance is increasing. The principle behind the working of the as prepared TENG could be explained on the basis of transfer of charge among ground and Al foil, by varying the gap distance in the rGONRs/PVDF film and the Al foil due to the leakage field present at the edges of the thin films having definite size. The distance which was made between the rGONRs/PVDF thin film and Al foil must not be small while comparing it with the dimensions of the rGONRs/PVDF film or Al foil. If the gap distance between the rGONRs/PVDF thin film and Al foil is very less than the sizes of Al foil or the size of both the materials are approximately much large, then the charge transfer among the ground and Al might be very less. If this could be done, then the as prepared device might not work properly.

It is noted that our fabricated TENG performance is low as compared to reported literature elsewhere [67–69]. In this research, we are trying to explore our research on other low-cost materials, which is easily available and easy to synthesis.

In the literature, researchers are measuring the electrical outputs of TENG using Keithley instrument by applying force thorough hydraulic pressing system at consistent frequency. Moreover, they have also used noise amplifier to amplify the electrical outputs. However, in case of our research work, electrical outputs (voltage and current) are measured using digital multimeter and pico-ammeter by hand pressing of TENGs as displayed in Figure 3.11 (Chapter 3). In hand pressing of TENG, we can't apply identical force in each pressing, which affects the surface morphology of fabricated thin film as well as output of the TENG. Also, time interval between successive pressings of TENG can't be same in hand pressing process. Both these factors play crucial role to obtain good output results of fabricated TENG. Additionally, the contact surface area between the triboelectric layers during working of TENG also plays serious role to obtained output performance. Higher output performance was observed in literature with larger contact surface area. For instance, Fan *et al.* has fabricated TENG with contact surface area of  $4.5 \times 1.2 \text{ cm}^2$  and found the electrical output voltage as 3.3 V [47]. On the other hand, Mallineni *et al.* fabricated U-TENG (low-cost and ultra-simple TENGs) with  $14 \text{ cm} \times 14 \text{ cm}$  as contact surface area has the ability to power  $\sim 200$  LEDs and with  $20 \text{ cm} \times 28 \text{ cm}$  (as contact surface area) U-TENG was used in passive vehicle/pedestrian monitoring applications with highest output voltage as  $\sim 480 \text{ V}$  [133]. Therefore, from above literature study, it is clearly revealed that output performance of TENG is also related to contact surface area of triboelectric

surfaces. Moreover, we also did not use any amplifier circuit during the measurement of electrical outputs of TENG. Because, amplifier plays key role to improve or amplify the input signals, or we can say that it is convert low input voltage signal into higher voltage output signal. Thus, our fabricated TENG output results are low as compared to reported literature.



## Section 4.2

### Fabrication of triboelectric nanogenerator using fluorinated-graphene nanoribbons and poly(vinylidene fluoride) composite nanofibers

#### 4.2.1 Fabrication of TENG

**Figure 4.2.1(a-d)** displays the fabrication of TENG. In brief, take two substrates of PMMA sheet ( $3\frac{1}{2} \times 3\frac{1}{2} \times \frac{1}{2}$  inches<sup>3</sup>) (**Figure 4.2.1(a)**) and fix Al sheet ( $5 \times 5 \times 0.5$  cm<sup>3</sup>) in the middle part of both PMMA sheets as shown in **Figure 4.2.1(b)**. Then, make four half holes on the four corners of PMMA sheets for fitting the springs and four complete holes on the middle of the sides of the PMMA sheets to fix the screw. Herein, Al would act as electrode for collecting the charges. Then, PVDF/F-GNRs composite nanofibers are fabricated on one side of Al fixed PMMA substrate and nylon nanofibers are deposited on other Al fixed PMMA sheet substrate using electro-spinning (**Figure 4.2.1(c)**).

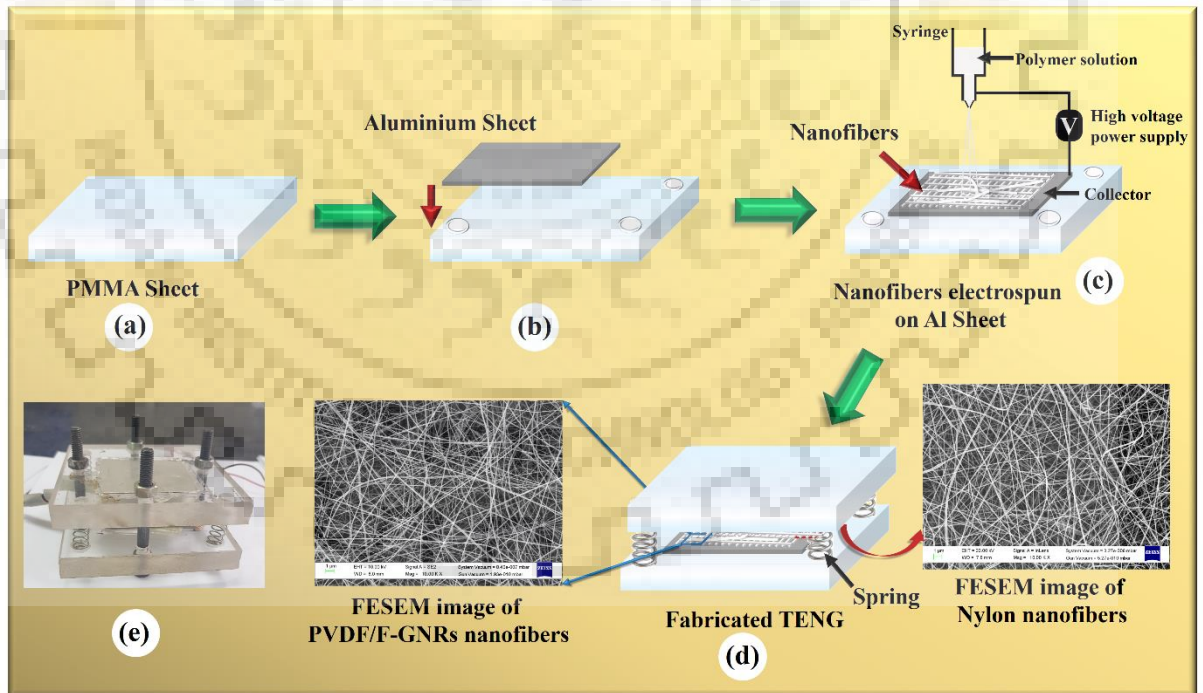


**Figure 4.2.1.** Fabrication of the TENG (a) PMMA sheet as substrate material (b) Aluminium (Al) is fixed in the middle part of the PMMA sheet and made four half drilled holes on the four

corners (c) Nanofibers via electro-spinning method are fabricated on the Al sheet (d) Both the substrates are assembled, where springs are used for maintaining the gap distance between them (e) Optical image of the fabricated TENG

The PVDF/F-GNRs nanofibers decorated Al fix PMMA substrate and nylon nanofibers coated PMMA substrate act as negative and positive tribo-electric surfaces, respectively. The fabrication of TENG is completed by assembling both the surfaces (nanofibers surfaces facing each other) using springs and tightening the bolts with keeping the distance of 5 mm between the surfaces as shown in optical image of **Figure 4.2.1(e)**. Finally, Cu wires are soldered with Al electrodes to collect the generated electrical outputs.

### 4.2.2 Morphological Analysis

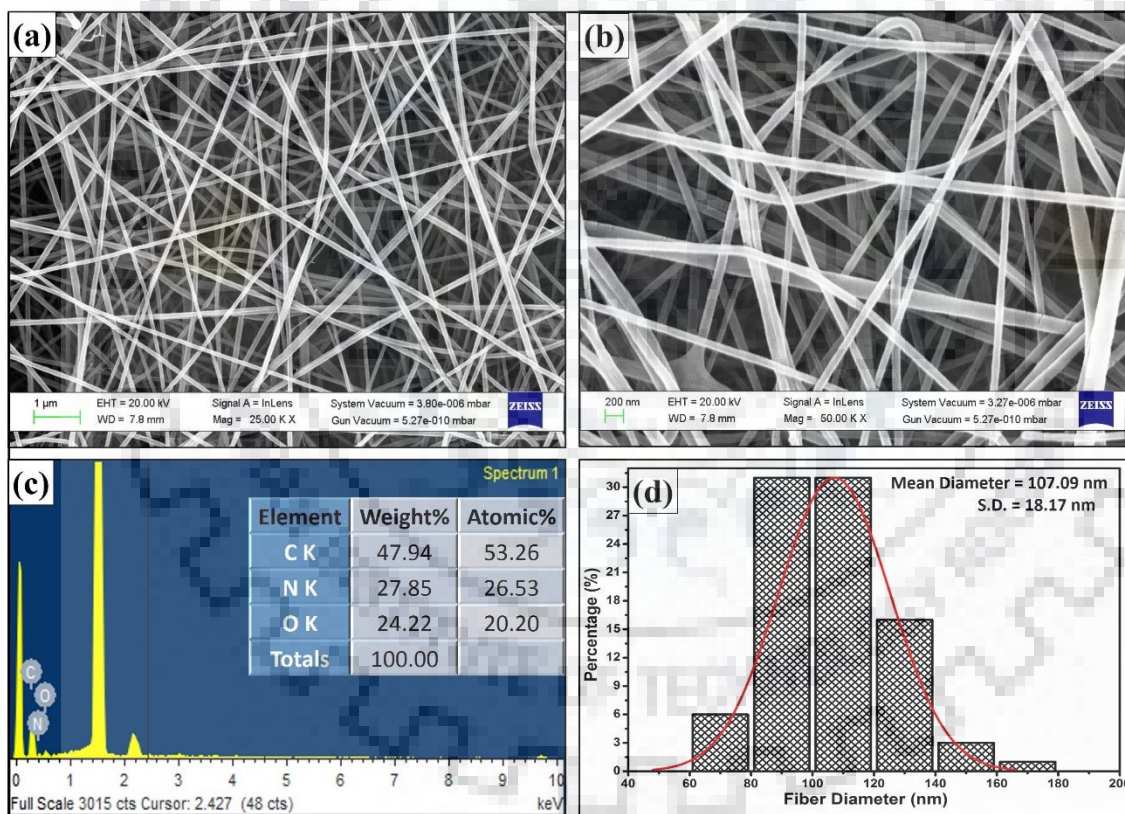


**Figure 4.2.2.** (a) FE-SEM analysis of the nylon nanofibers at low resolution and (b) Highly magnified image of the nylon nanofibers (c) EDAX analysis with weight% and atomic% corresponding to various elements present (d) Diameter distribution histogram of the nylon nanofibers

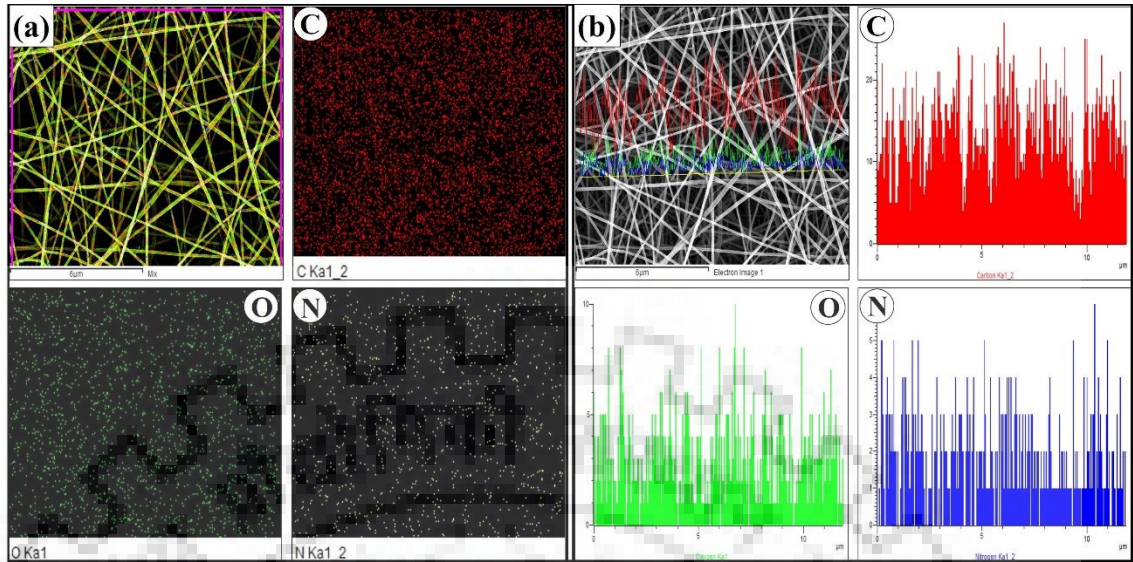


**Figure 4.2.3.** (a) Elemental mapping of the nylon nanofibers (b) EDAX line frequency maps of the elements present in the nylon nanofibers

For analysis the surface morphology, elemental distribution and weight% of the elements present in the fabricated nanofibers, FESEM, and EDAX analysis, respectively, are carried out. **Figure 4.2.2 (a)** at low magnification and **Figure 4.2.2 (b)** at high magnification show surface morphology of fabricated nylon nanofibers, which displays nanofibers are well decorated, bead free and having almost uniform thickness. Moreover, EDAX analysis examined the weight% of various elements present in the nanofibers i.e. 47.94%, 27.85% and 24.22% for C, N and O, respectively as depicted in **Figure 4.2.2 (c)**. The mean diameter and S.D. of the nanofibers are calculated using diameter distribution histogram (**Figure 4.2.2 (d)**) of the nanofibers as 107.09 nm and 18.17 nm, respectively. Further, the elemental mapping and line scanning are confirmed the presence of various elements such as C, O and N in the fabricated nylon nanofibers as shown in **Figure 4.2.3 (a)** and **(b)**.

**Figure 4.2.4 (a)** and **(b)** display the surface morphology of fabricated PVDF nanofibers at high magnifications. The weight% of C and F found to be 39.64% and 60.36% respectively using EDAX analysis (as illustrated in **Figure 4.2.4 (c)**). **Figure 4.2.4 (d)** indicates the diameter distribution histogram of fabricated PVDF nanofibers with mean diameter and S. D. are found to be 128.71 nm and 29.78 nm, respectively. The elemental mapping and line scanning reveal the presence of C and F in the fabricated PVDF nanofiber as shown in **Figure 4.2.5 (a)** and **(b)**, respectively.

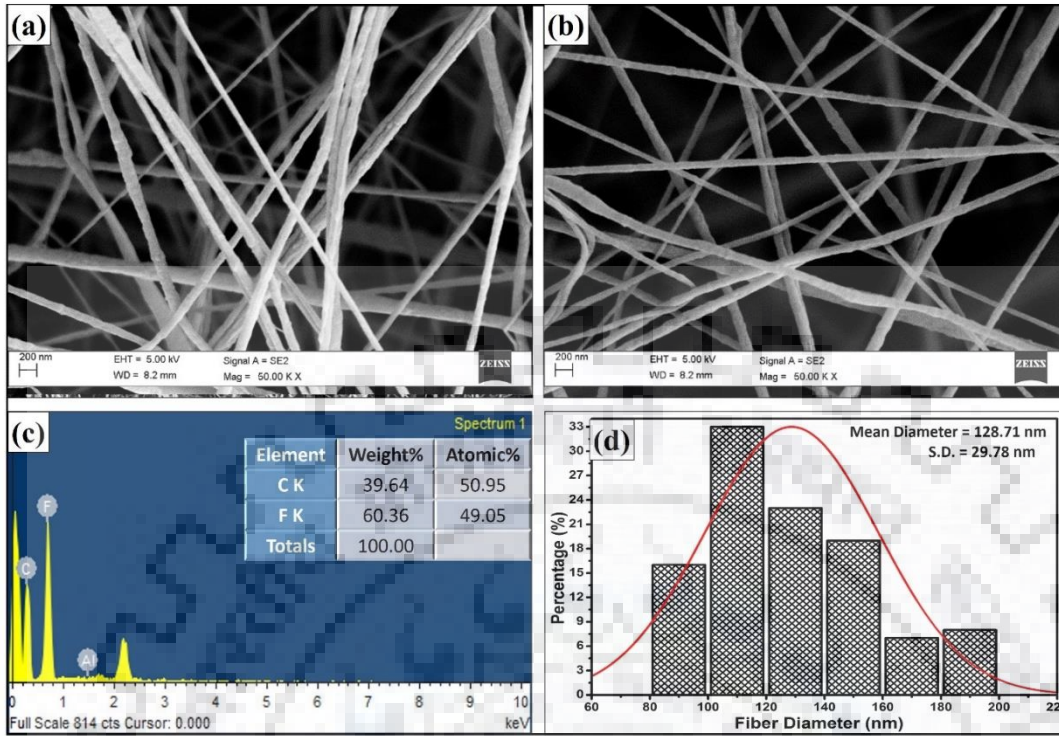


**Figure 4.2.4.** (a) & (b) FE-SEM analysis at high magnification of the PVDF nanofibers (c) EDAX analysis for various elements present in the PVDF nanofibers (d) Diameter distribution histogram of the PVDF nanofibers

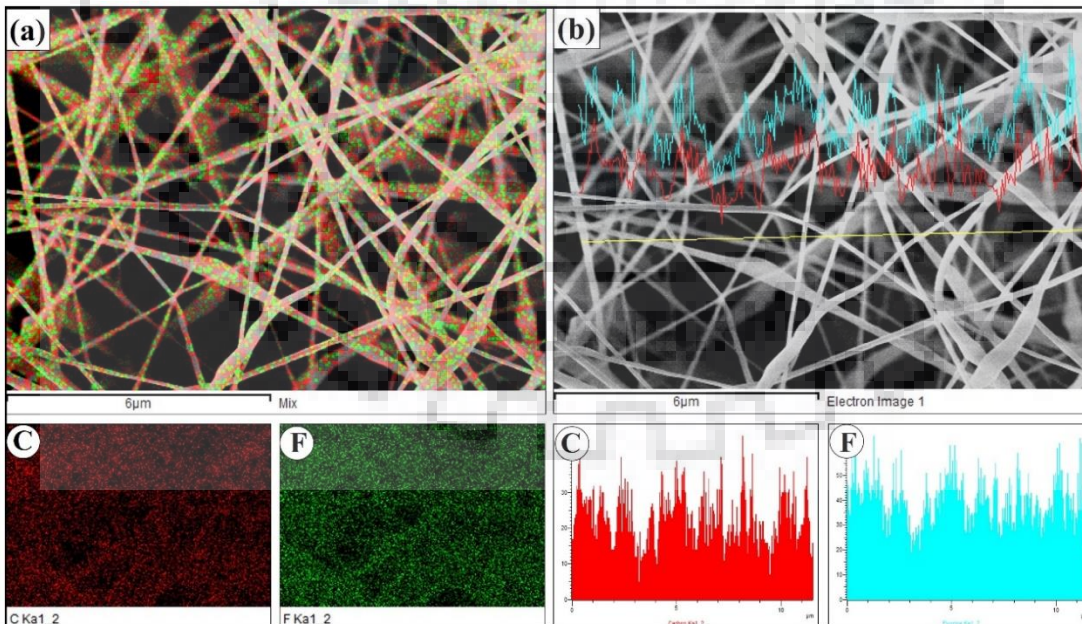


**Figure 4.2.5.** (a) Elemental mapping and (b) EDAX line frequency maps scan of the PVDF nanofibers

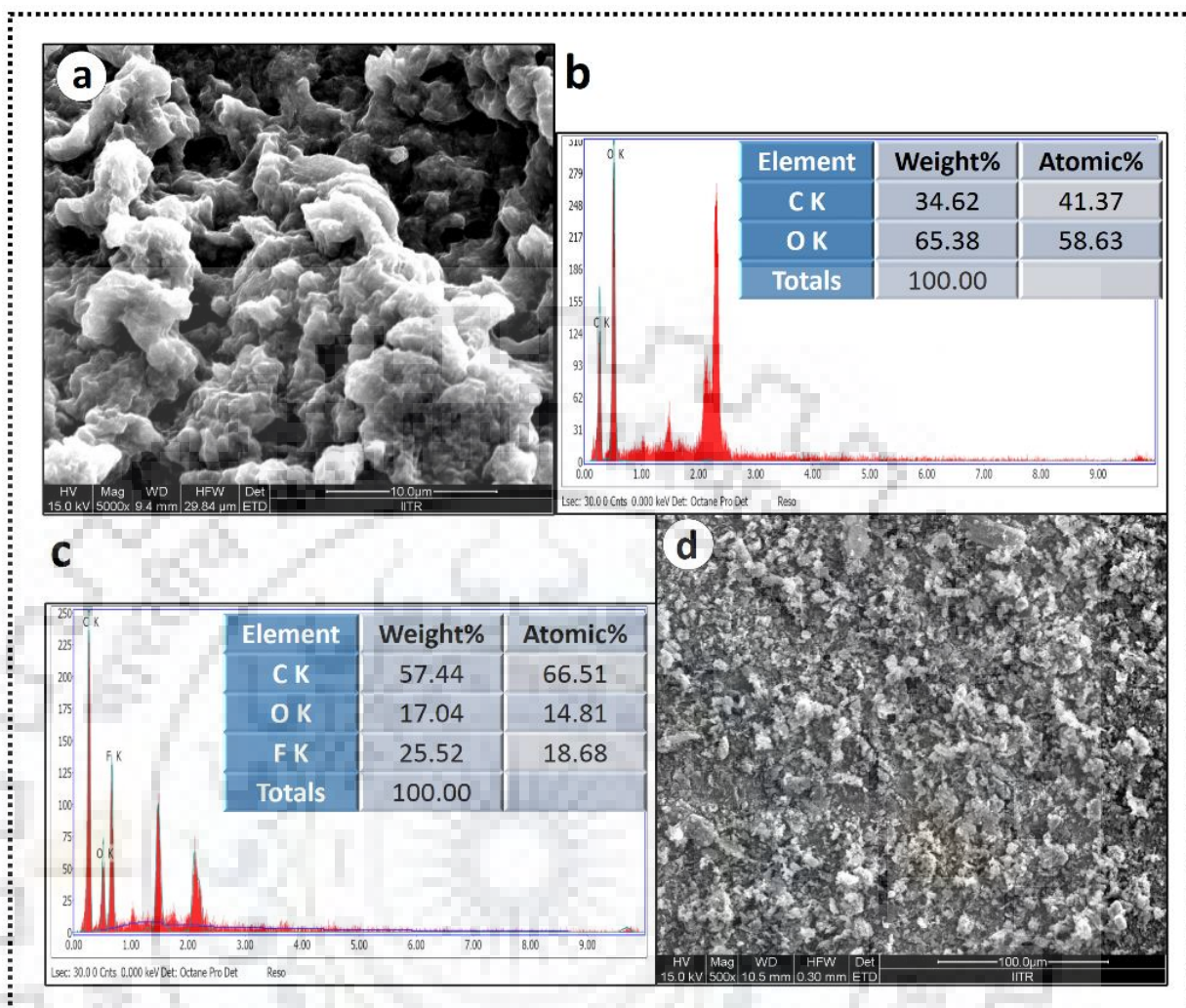


**Figure 4.2.6.** (a) SEM image of the synthesised rGONRs through unzipping of Multiwalled-CNTs (b) EDAX analysis shows the weight% of the elements exists in the rGONRs (c) EDAX analysis shows the weight% of the elements exists in the fluorinated-GNRs (F-GNRs) (d) SEM image of the synthesised F-GNRs from rGONRs through HF acid treatment

In order to examine the surface morphology and EDAX analysis of the fillers, SEM is carried out for rGONRs and F-GNRs as shown in **Figure 4.2.6**. EDAX reveals that after fluorination of rGONRs, the oxygen content is lesser as compare to the pristine rGONRs. Moreover, the amount of fluorine is found to be 25.52 weight% in the synthesized F-GNRs using EDAX analysis.

**Figure 4.2.7** (a) and (b) depicts the beautiful surface morphology of as fabricated PVDF/F-GNRs nanofibers at low and high magnification, respectively, which inform nanofibers

are bead free and almost uniform thickness. From EDAX analysis, we can examine the weight% of the elements present in the nanofibers (C, F, O and Al are 41.57%, 54.07%, 1.34% and 3.03% respectively) are as shown in **Figure 4.2.7 (c)**. However, a low amount of Al weight% is detected in the nanofiber EDAX analysis due to the Al sheet, which used as substrate for collecting the nanofibers. The diameter of the nanofibers is measured using ImageJ software and prepared diameter distribution histogram of the composite nanofibers as indicated in **Figure 4.2.7 (d)** with mean diameter and standard deviation (S.D.) of 118.23 nm and 23.62 nm, respectively. The elemental mapping and line scanning confirm the presence of C, F, O and Al in the fabricated PVDF/F-GNRs nanofibers as illustrated in **Figure 4.2.8 (a)** and **(b)**, respectively.

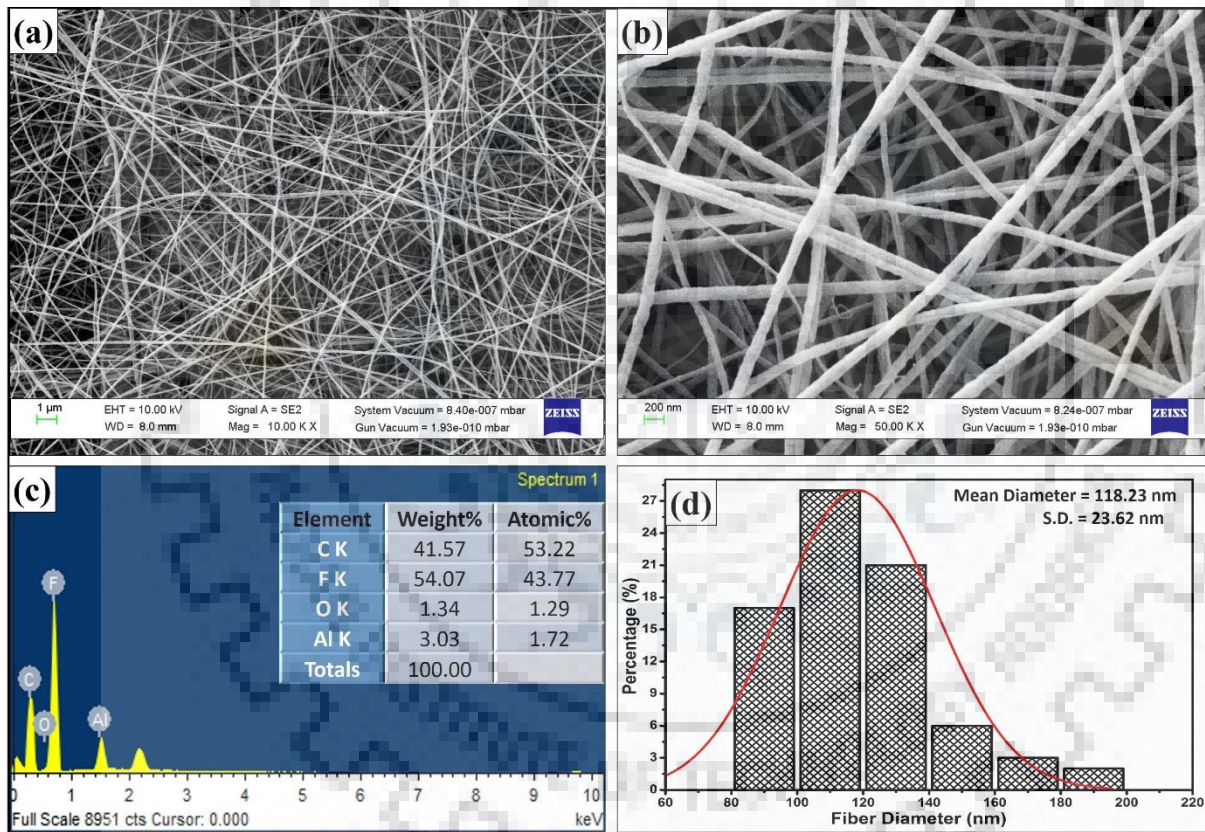


**Figure 4.2.7.** (a) FE-SEM image of the PVDF/F-GNRs nanofibers (b) Highly magnified image of the composite (PVDF/F-GNRs) nanofibers (c) EDAX analysis of composite nanofibers (d) Diameter distribution histogram of the composite nanofibers



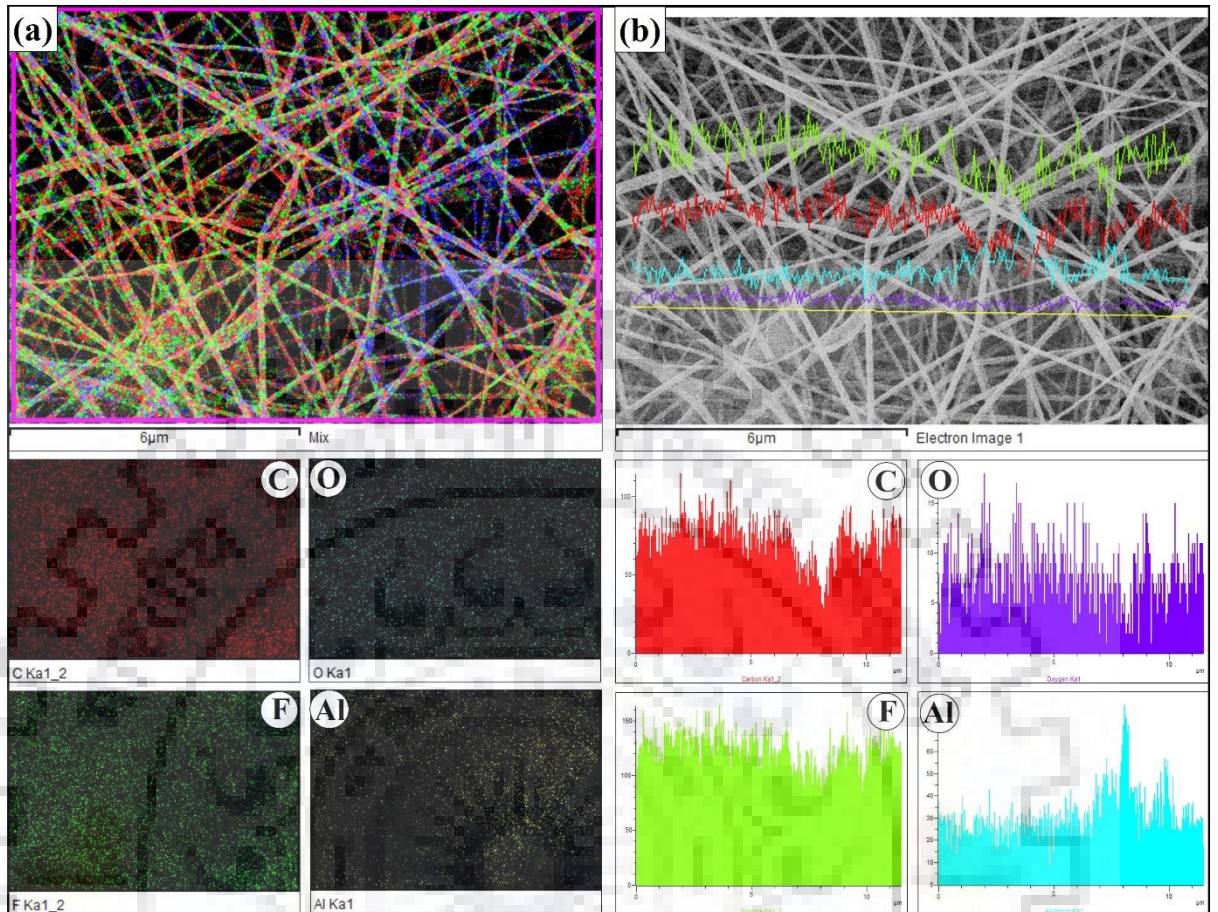


**Figure 4.2.8.** (a) Elemental mapping distribution for various elements exist in the sample (b) EDAX line frequency maps of the elements present in the composite nanofibers

### 4.2.3 X-ray diffraction Analysis

The crystal structure and phase composition of the pristine PVDF, PVDF/F-GNRs composite, and nylon nanofibers are measured using X-ray Diffraction patterns (**Figure 4.2.10**). The sharp characteristic peak observed in both PVDF and PVDF/F-GNRs composite at  $2\theta = 20.0^\circ$  is due to strong  $\alpha$ -phase crystalline signal with (110) plane and having interlayer space (d-spacing) of 0.44 nm, which gives the reflection that it possess very high fluorine level (JCPDS card no. 38-1638) [234–236]. The intense peak present at  $2\theta = 20.6^\circ$  in PVDF/F-GNRs composite is may be due to the strong  $\beta$  crystalline phase with (200) plane [234]. The fraction of  $\beta$ -phase is observed in the PVDF/F-GNRs composite nanofibers sample because as the applied electric field is increased to the polymer jet, which leads to mechanical stretching in fabricated nanofibers. Therefore, PVDF/F-GNRs composite nanofibers exhibited strong  $\beta$ -phase due to higher

electrospinning voltage as compare to pristine PVDF nanofibers [234,237]. Furthermore, the characteristic peaks observed in F-GNRs (**Figure 4.2.9 (a)**) diffraction patterns at  $2\theta = 15.8^\circ$  is may be due to the presence of high level fluorine groups, which is invisible in rGONRs. One diffracted peak (Figure 4.2.9) detected at  $2\theta = \sim 25.6^\circ$  with (002) plane, confirms the presence of  $sp^2$  C and also may be due to the various functional groups (like  $-\text{CO}$ ,  $-\text{COOH}$ ,  $-\text{OH}$ , etc.) (JCPDS card no. 41-1487), which is absent in the PVDF/F-GNRs sample may be due to less amount of filler used. Some other characteristic peak observed at  $2\theta = 28.72^\circ$  and  $46.85^\circ$  assigned to (111) and (220) plane, respectively, which confirm the presence of fluorine groups in the as synthesised sample (JCPDS card no. 27-0725 and 35-0816) as indicated in **Figure 4.2.10**.

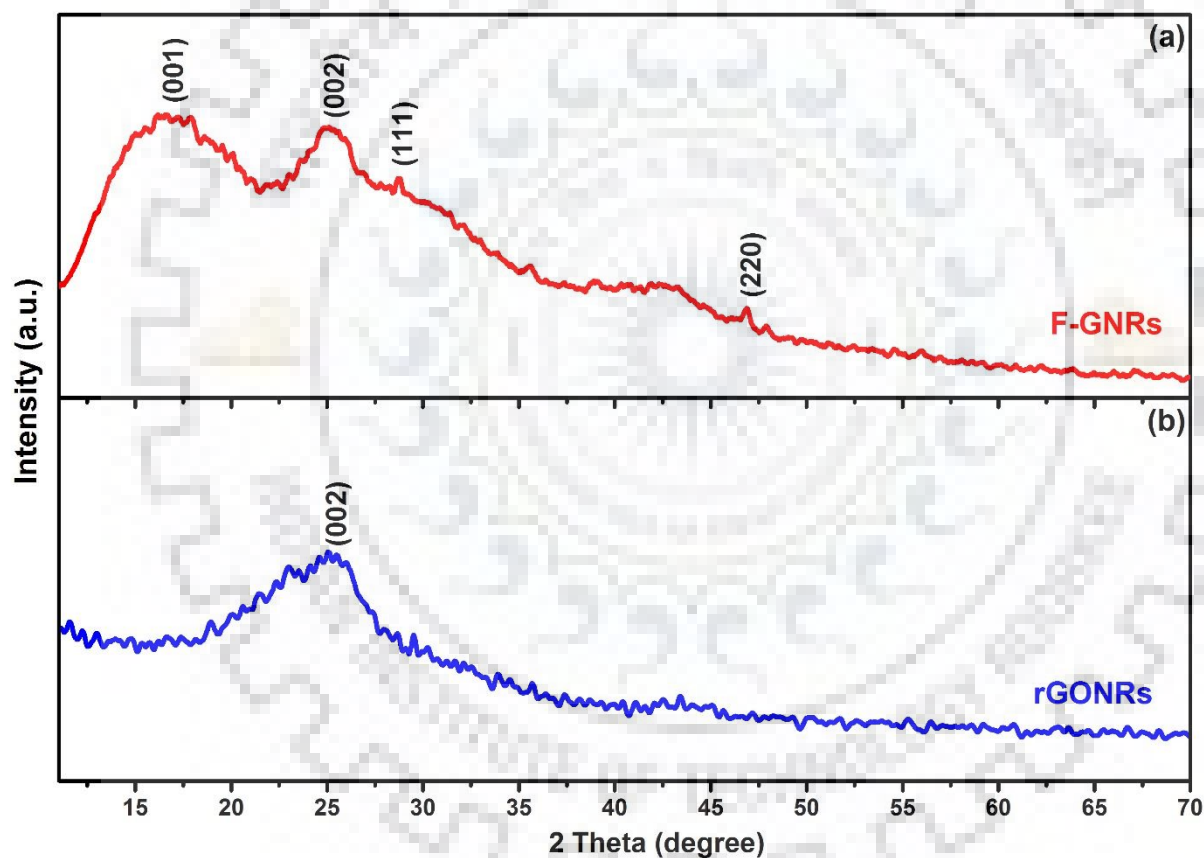


**Figure 4.2.9.** X-ray Diffraction pattern of (a) fluorinated-GNRs (F-GNRs) (b) rGONRs

The two intense characteristic peaks are observed in the XRD pattern of nylon 6,6 (as shown in Figure 4.2.10 (c)) at  $2\theta = 20.27^\circ$  and  $23.8^\circ$  corresponding to (100) and (010) planes, respectively, which indicate the presence of  $\alpha$ -phase [238,239]. Due to inter polymer hydrogen bonding, these peaks are showing crystalline packing [240]. The thermodynamically stable  $\alpha$ -

phase consist sheets of hydrogen bonded chains, which are packed in anti-parallel manner[238]. The obtained diffraction patterns are almost similar as reported elsewhere [239,241].

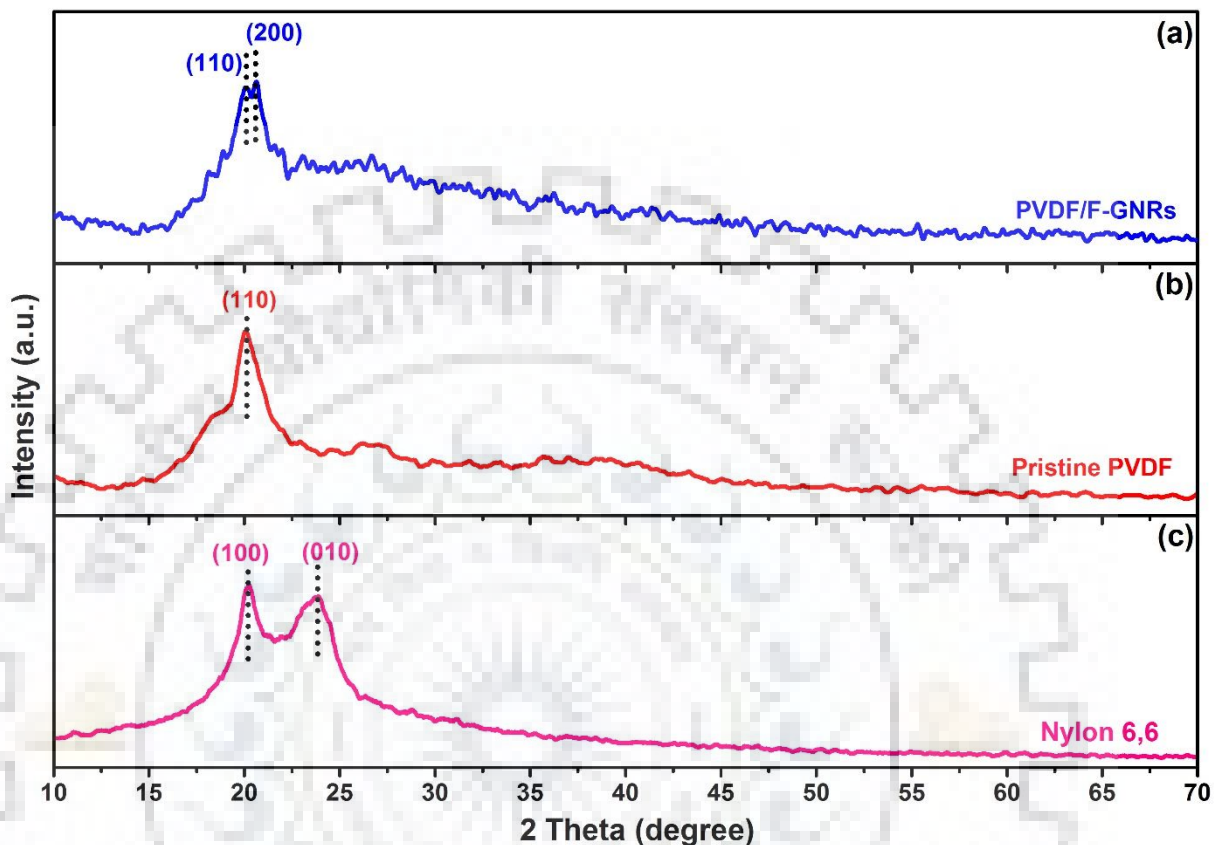


**Figure 4.2.10.** XRD patterns of (a) PVDF/F-GNRs composite nanofibers (b) Pristine PVDF nanofibers and (c) Nylon 6,6 nanofibers

#### 4.2.4 Fourier Transformation Infrared (FTIR) Spectroscopy

For probing the presence of various functional groups in the prepared samples, FTIR analysis is carried out and observed several characteristic peaks in the spectrum of pristine PVDF nanofibers, PVDF/F-GNRs composite nanofibers, nylon nanofibers, rGONRs and F-GNRs. The strong and broad spectra near to  $\sim 3400\text{ cm}^{-1}$  is found, which confirms the presence of hydroxyl group (O-H stretching vibrations) in all the synthesised samples except nylon nanofibers. The broad spectra in the range from  $3300\text{-}3500\text{ cm}^{-1}$  is due to the presence of N-H stretching (secondary amines) in the nylon nanofibers. The bands corresponding to the range from  $\sim 2850\text{-}3000\text{ cm}^{-1}$  are may be due to the C-H stretching vibration in all the samples. The characteristic peaks at  $2136\text{ cm}^{-1}$  represent C-C stretching due to alkynyl bonds present in the nylon, PVDF

and PVDF/F-GNRs samples as shown in **Figure 4.2.11**. The adsorption peaks near to  $\sim 1740\text{ cm}^{-1}$  and  $\sim 1630\text{ cm}^{-1}$  are confirming the presence of carbonyl and alkenyl groups, respectively in the synthesized samples.

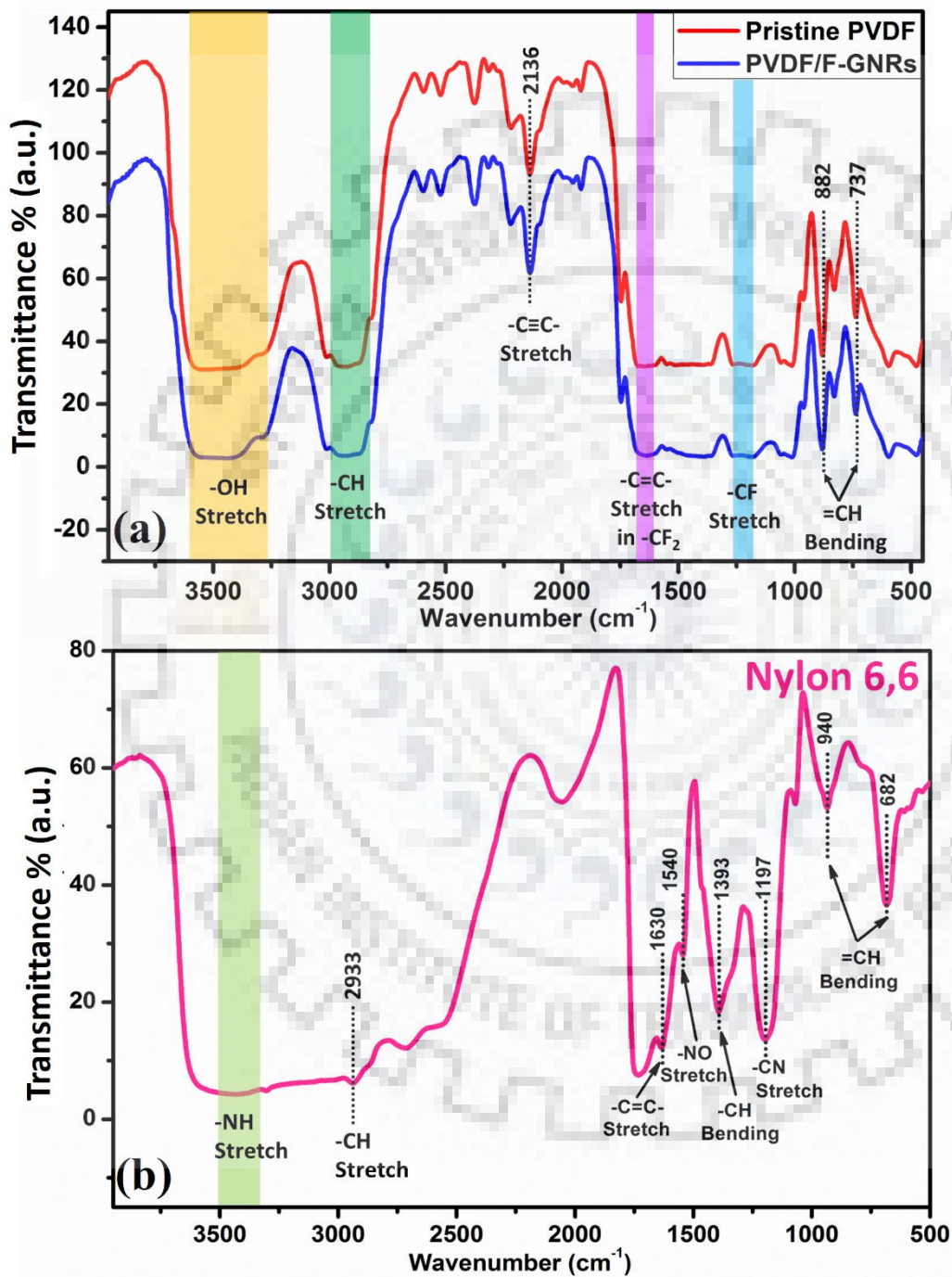


**Figure 4.2.11.** Fourier Transformer infrared (FTIR) spectrum of (a) Pristine PVDF nanofibers and PVDF/F-GNRs composite nanofibers (b) Nylon 6,6 nanofibers

The prominent peaks in the range 1000–1400  $\text{cm}^{-1}$  correspond to the  $-\text{CF}_2$  stretching present in the PVDF, PVDF/F-GNRs and F-GNRs samples, confirm the presence of fluorine group, which are absent in Nylon 6,6 and rGONRs as depicted **Figure 4.2.11 (b)** and **Figure 4.2.12** [242,243]. The adsorption band present at 1197  $\text{cm}^{-1}$  and 1540  $\text{cm}^{-1}$ , gives the signal that C-N vibrations and N-O stretching, respectively are present in the nylon nanofibers as illustrated in **Figure 4.2.11(a)**. Other peaks from 940 to 680  $\text{cm}^{-1}$ , are indicating  $=\text{CH}$  bending vibrations present in the synthesized samples [234,244,245].

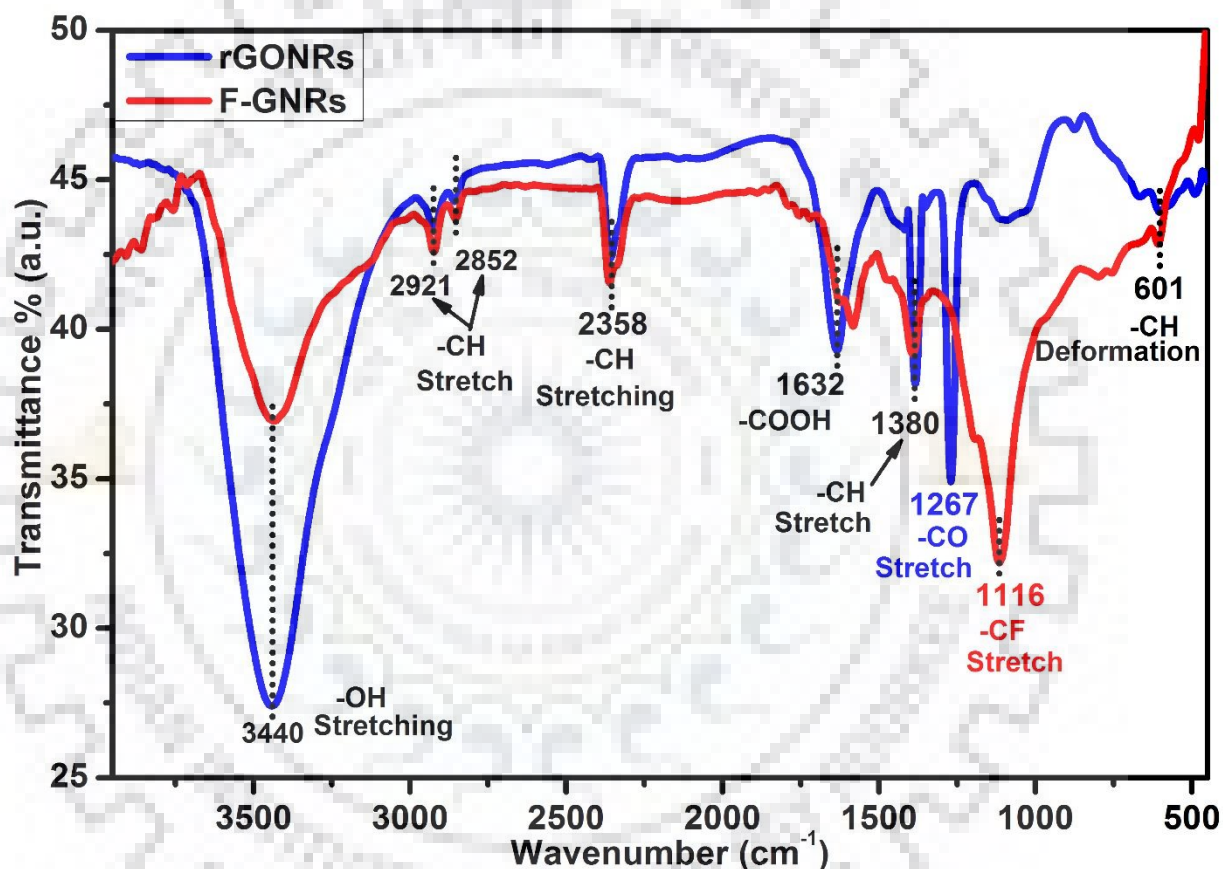


**Figure 4.2.12.** Fourier Transformer infrared (FTIR) spectrum of rGONRs and fluorinated-GNRs (F-GNRs)

#### 4.2.5 Raman Spectroscopy Analysis

Raman spectroscopy is an influential tool to differentiate various types of bonds like  $\text{sp}^3$ - and  $\text{sp}^2$ -hybridized carbons. Generally, G and D band intensities are assigned to  $\text{E}_{2g}$  phonon of  $\text{sp}^2$ -hybridised carbon atoms and degree of defects ( $\text{A}_{1g}$  symmetry of k-point phonons) in the carbon nanostructures, respectively [246]. The characteristic peaks at 1343 and 1583  $\text{cm}^{-1}$  are

corresponding to D and G bands, respectively in the rGONRs and F-GNRs as shown in **Figure 4.2.13**. The other peak at  $2715\text{ cm}^{-1}$  represents the 2D band. From Raman spectra (Figure 4.2.13),  $I_D/I_G$  ratios for rGONRs and F-GNRs are found to be 1.07 and 1.06, respectively. The enhanced  $I_D/I_G$  ratio of F-GNRs is probably due to the functionalization (attachment of fluorine group), which induce defects in the pristine structure (rGONRs) [247].

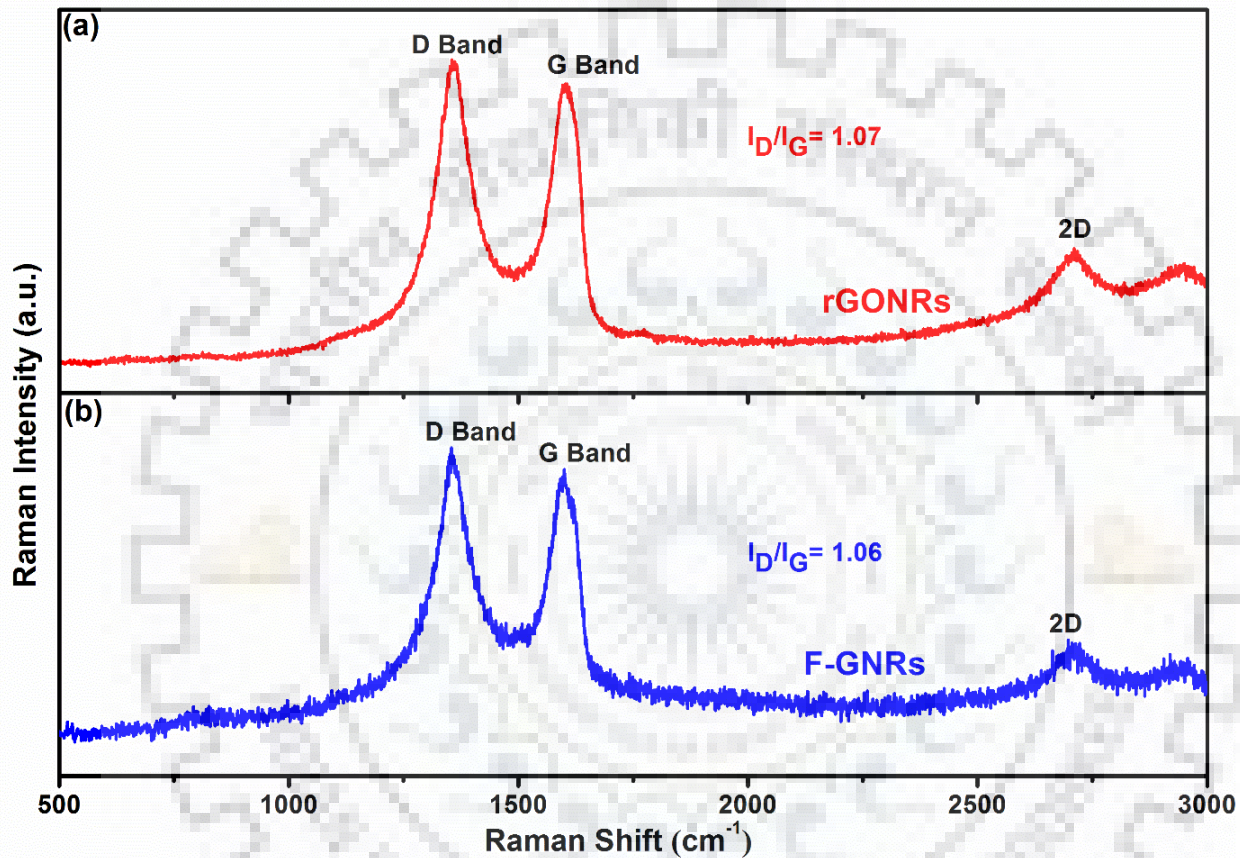


**Figure 4.2.13.** RAMAN Spectroscopy of (a) rGONRs and (b) fluorinated-GNRs (F-GNRs)

#### 4.2.6 Mechanism behind the working of TENG

For fabrication of TENG, PMMA is chosen as the substrate materials due to the light weight, cheap, strength and easy availability. Then, Aluminium (Al) sheet is fixed in the middle part of both substrates, which acts as an electrode for collecting the charges. The fabricated PVDF/F-GNRs and nylon nanofibers are individually electro-spun on Al fixed part of both substrates as shown in **Figure 4.2.1 (c)**. The diameter and beautiful morphology of fabricated nanofibers are already discussed in the FESEM analysis. Thereafter, PVDF/F-GNRs and nylon

nanofibers deposited substrates are put at upper and lower positions, respectively, and assembled them by using springs and tightening the bolts as shown in optical image (**Figure 4.2.1 (e)**).

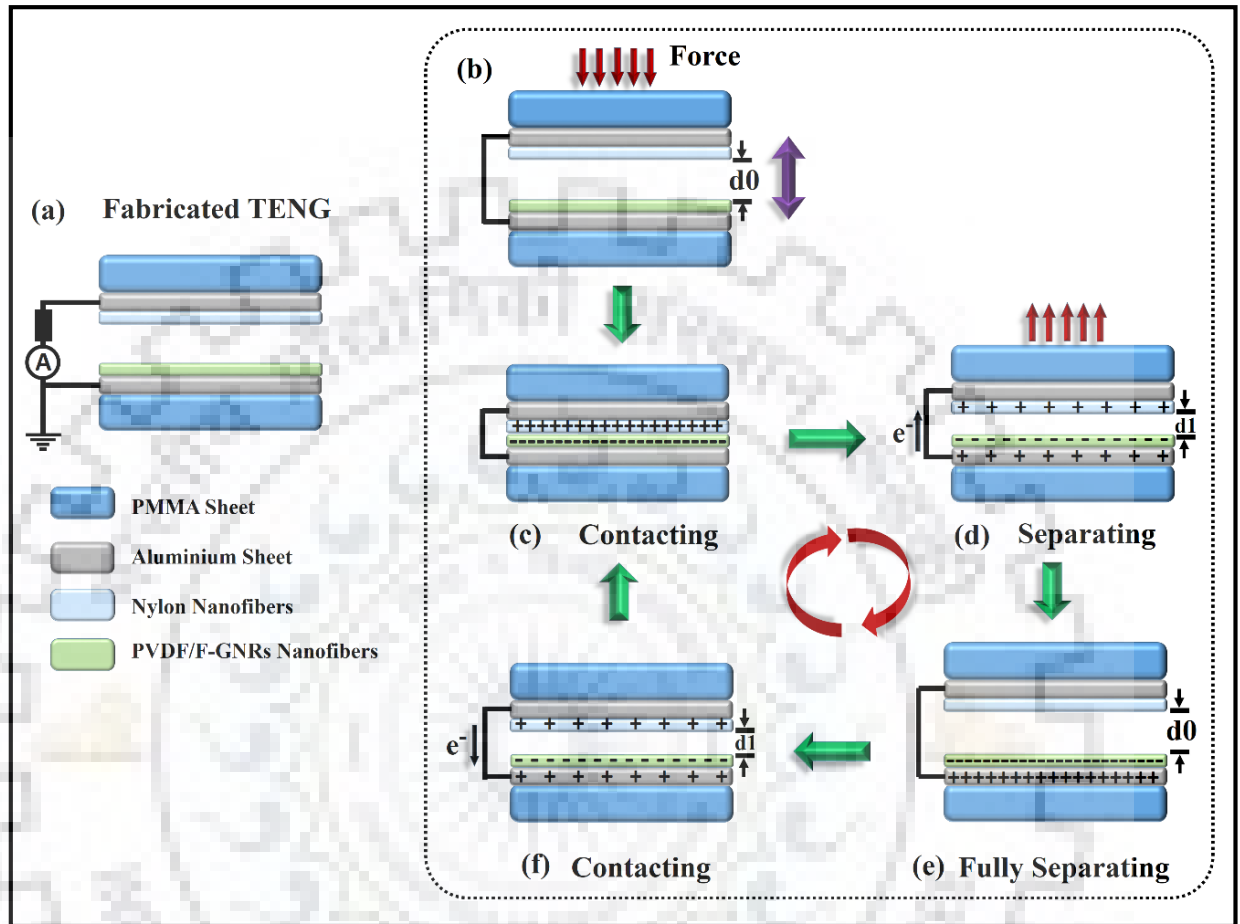


**Figure 4.2.14.** (a) Schematic of the fabricated TENG (b-f) Working mechanism of the TENG (b) Initial position, when no external mechanical force is applied (c) By applying external force on the top substrate, it brings PVDF/F-GNRs nanofibers layer into contact with nylon nanofibers layer, generating negative triboelectric charges on the PVDF/F-GNRs side and positive charges on the nylon side (d) By removing the external force, separation between the electrodes occurs and potential difference drives the electrons from the lower electrode to the top electrode, triboelectric charges are distributed on the surfaces and the inductive charges are left behind (e) Initial position is achieved by all the negative triboelectric charges distributed on the contact surface (f) As the force is reapplied, the electrons flow back towards the lower side electrode for screening the inductive charges Note: For the structure simplification, springs and nanofibers morphology in the schematics are not shown

The mechanism of electrical energy generation is explained by combining the electrostatic effect with triboelectric effect, as explained in **Figure 4.2.14 (a)**. Initially, the maximum separation distance ( $d_0$ ) (**Figure 4.2.14 (b)**) is upheld using springs. By applying the external force on the upper part, PVDF/F-GNRs nanofibers and nylon nanofibers comes in contact with each other. The materials have tendency to lose or gain electrons, as electrons are injected from nylon into PVDF/F-GNRs nanofibers, and hence surface acquire triboelectric charges, which are retained on both the surfaces (**Figure 4.2.14 (c)**), according to the triboelectric series [81,192,193]. When the force from the substrates is withdrawn, both the contacting surfaces move away from each other, owing to restoring force of the springs. As soon as the separation forms between the surfaces, a less electric potential is developed in the back electrode as compare to the contact surfaces, resulting in the electric potential difference, which drives the electrons through the external load (**Figure 4.2.14 (d)**). As the TENG comes back in its initial position, positive triboelectric charges on the top contact surface are entirely screened, leaving same quantity of inductive charges on the back electrode of the lower part (**Figure 4.2.14 (e)**). Afterwards, again mechanical force is used to reduce the separation distance, which produces an electric potential difference but with opposite polarity, resulting the flow of electrons in the opposite direction (**Figure 4.2.14 (f)**). The inductive charges are keep screening on the back electrode till a direct contact is established again (**Figure 4.2.14 (c)**). It has been observed that the insulating nylon and PVDF can hold the triboelectric charges on its surface for long time[248], while the triboelectric charges on the metals are sometimes screened by inductive charges. So, fabricated TENG behaves like an electron pump that transfers electrons between both the electrodes.

Human Hand is used to activate the TENG by applying force. The contacting force, which is defined interaction force generated between the nylon – PVDF nanofibers and nylon – PVDF/F-GNRs nanofibers as monitored by a pressure sensor. The electrical output performance of the TENG is measured in terms of short-circuit current ( $I_{SC}$ ) and open-circuit voltage ( $V_{OC}$ ). The  $V_{OC}$  and  $I_{SC}$  for both the TENGs are obtained by applying 260 N of contacting force as shown in **Figure 4.2.15 (a-d)**. The sharp increment is observed in the  $V_{OC}$  curve, when TENG shifts from initial position to contact position.



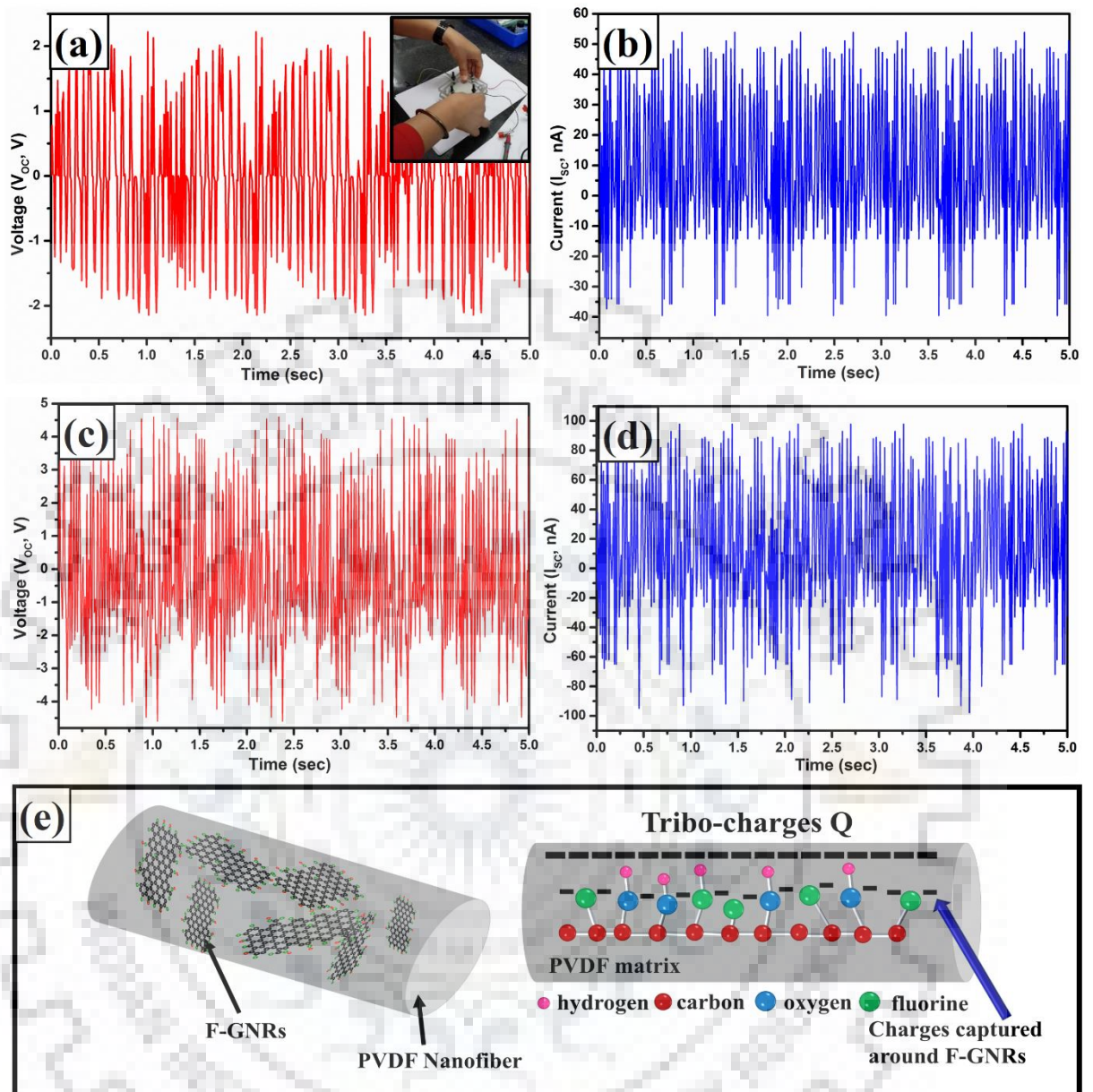


**Figure 4.2.15.** Electrical outputs of the fabricated TENG using pristine PVDF and nylon nanofibers: (a)  $V_{OC}$  (volts) (inset shows the mechanical energy applied on the TENG to get the output) and (b)  $I_{SC}$  (nA) For fabricated TENG using PVDF/F-GNRs and nylon nanofibers: (c)  $V_{OC}$  (volts) and (d)  $I_{SC}$  (nA) (e) Schematic for dispersion of F-GNRs in a PVDF nanofiber, and stored surface charge on the PVDF/F-GNRs nanofibers

The AC behaviour is observed within one cycle of the  $I_{SC}$  as same quantity of electrons are flowing in opposite directions. The data obtained experimentally authenticates the working principle of the TENG, which is described in **Figure 4.2.14**. At separate position, obtained

current signal having lower magnitude, but stable for longer time in comparison of contact position. The output could be explained by faster contact between the surfaces with the external forces, which is higher than the restoring force of springs. If the connections are reversed between the TENG, then the electrical output signals are also give reverse polarity. Further, by connecting a full-wave rectifier bridge, obtained output values are transmitted to pulse output in the similar direction.

The output of TENG is completely depends on the contact force, higher the contact force, higher the output and vice versa. When the force is low as 10 N, then TENG can also give  $I_{SC}$  as 27.4 nA. But as the contact force is increased to 260 N, then the electrical outputs reach a certain peak value, generating  $I_{SC}$  of 98 nA. Due to the faster contact separation between the contact surfaces, more force,  $I_{SC}$  increases and hence, contact area also increases. The surface morphology of the surfaces plays very significant role in the output generation. Both the contact surfaces must have certain morphology, which means the surface must be rough. Surface roughness can be triggered by the nanoparticle modification, or by fabricating defects, or by making certain morphology of the material, etc. When the lower force is applied on the surfaces, surface roughness doesn't allow the surfaces to have fully intimate contact among the PVDF/F-GNRs nanofibers and nylon nanofibers surfaces and hence produces less electrical outputs. However, when the large force is applied on the surfaces, the elastic property of the polymers has ability to fill the empty spaces, which leads to the larger contact area, resulting in higher electrical outputs.

For further investigating the effective electrical power of the TENG, resistors are connected in the circuit as external loads. Although by increasing the load resistance, the instantaneous current drops, owing to Ohmic loss, but the voltage enhances. Subsequently, the instantaneous power output ( $W$ ) is calculated using the equation (4.2.1) reached to the maximum value with a load resistance ( $R$ );

$$W = I_{peak}^2 \cdot R \quad (4.2.1)$$

Where  $W$  is instantaneous power output,  $I_{peak}$  is the peak value of  $I_{SC}$  and  $R$  is the load resistance applied in the circuit.

The electrical outputs of fabricated TENG using PVDF nanofibers are found to be 2.22 V and 54 nA as  $V_{OC}$  and  $I_{SC}$ , as shown in **Figure 4.2.15 (a)** and **(b)**, respectively and electrical charge after 4.5 s is calculated as 243.52 nC. However, when the pristine PVDF nanofibers are replaced with PVDF/F-GNRs nanofibers, then the electrical outputs are found to be 4.59 V as  $V_{oc}$  and 98 nA as  $I_{SC}$ , as displayed in **Figure 4.2.15 (c)** and **(d)**, respectively. The optical images of the maximum electrical outputs generated from PVDF/F-GNRs based TENG are displayed in **Figure 4.2.16**. The maximum charge ( $Q$ ) after 4.5 s is calculated to be 442.96 nC. This fabricated TENG is quite stable upto 2,000 cycles, without any loss in the output and in the nanofiber structures. Therefore, F-GNRs modified PVDF nanofibers exhibited higher electrical outputs in comparison to PVDF.

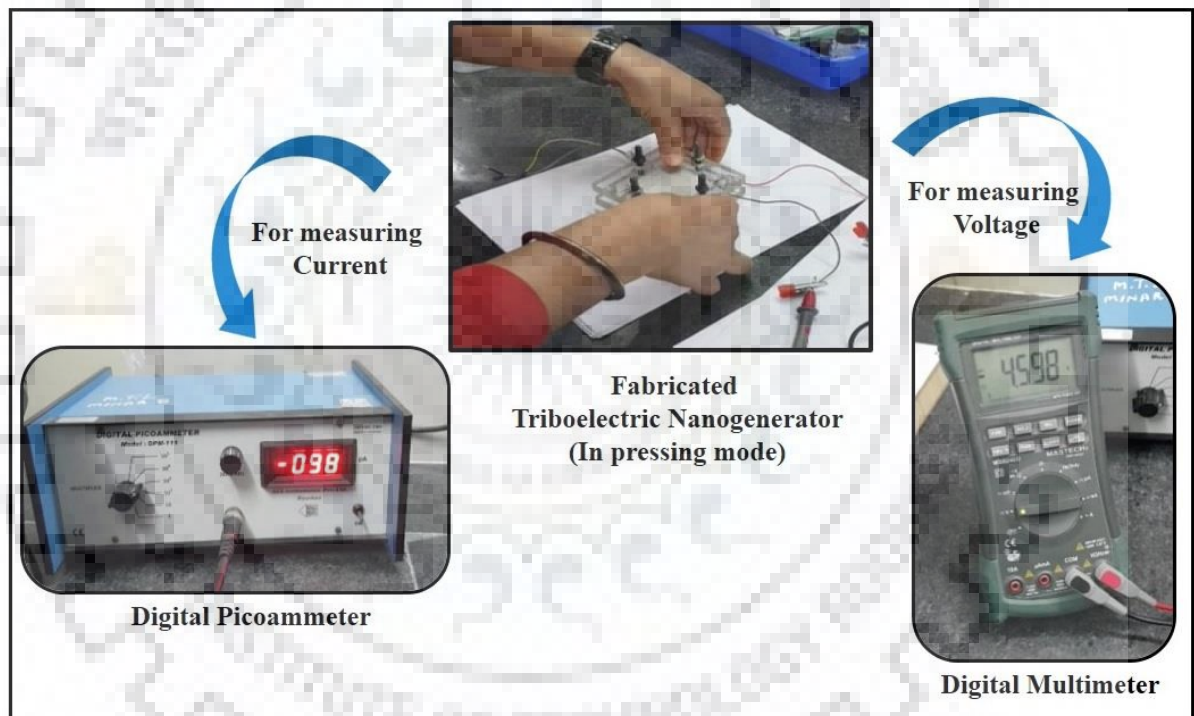


**Figure 4.2.16.** Electrical outputs (Current and Voltage) of fabricated TENG in hand pressing mode

The output of the TENG is mainly depends on the three main reasons. Firstly, the contact materials are having some morphological structures like nanofibers. These nanofibers has the ability to attain maximum charges on the surfaces. Secondly, due to elastic behaviour of the PVDF and nylon polymers have proper contact between the surfaces. These polymers can smoothly deform by applying low pressure on the surfaces and it will fill the empty spaces, which

will come in the fabrication defects. This can be possibly obtained that the surface roughness also enhances surface contact area. Lastly, the modification of the PVDF nanofibers by using the fluorinated-graphene nanoribbons (F-GNRs) in the PVDF polymer, which could enhance the charge trapping capacity of the nanofibers due to the presence of fluorine and oxygen groups in the F-GNRs as shown in **Figure 4.2.15 (e)**. As fluorine and oxygen are highly tribo-negative elements in the periodic table. The surface of polymer nanofibers would offer a more contact area as compare to flat surfaces. Chemically, the as-synthesised F-GNRs are negatively charges materials, due to the existence of fluorine and oxygen containing functional groups. Fluorine and oxygen are most electronegative elements in the periodic table, as they have strong tendency to accept electrons from the other material (nylon) to complete its outer most shell. So, accordingly the materials, which already have negative charges would enhance the triboelectric charges while contacting, leading to the largely improved surface charge density, and hence exhibit larger electrical outputs. The above study, which is carried out has analytically investigated the mechanism in enhancing the electrical output by the incorporation of filler in the polymer matrix. Hence, the selection of suitable materials, optimized structure and surface modified materials through functionalization are the three important factors, which contribute toward the higher power outputs.

For further understanding theoretically and transferred charge phenomena, which are based on contact of the dielectric-dielectric layers of the TENG, the open-circuit voltage (V) among both the electrodes is given using the following Eq. (4.2.2) [249]

$$V = E_1 t_1 + E_2 t_2 + E_{air} d \quad (4.2.2)$$

Whereas,  $E_1$ ,  $E_2$ , and  $E_{air}$ , are the electric-field strengths and could be expressed as Eqs. (4.2.3), (4.2.4), and (4.2.5), respectively.  $t_1$  and  $t_2$  are the thicknesses of the nylon nanofibers layer and PVDF/F-GNRs nanofibers layers, respectively and  $d$  is the gap distance among both the induced surfaces.

$$E_1 = -\frac{Q}{A\epsilon_{r1}\epsilon_0} \quad (4.2.3)$$

$$E_2 = -\frac{Q}{A\epsilon_{r2}\epsilon_0} \quad (4.2.4)$$

$$E_{air} = -\frac{Q + A\sigma}{A\epsilon_{r1}\epsilon_0} \quad (4.2.5)$$

Where, the relative permittivity of both the layers is measured in terms of  $\epsilon_{r1}$  and  $\epsilon_{r2}$ . Area of the electrode and transferred charges between the electrodes are denoted by A and Q, respectively. The theoretical charge density is calculated in terms of  $\sigma$  (calculated using Eq. (4.2.7)). The following equation (4.2.6) is obtained using above (4.2.2)-(4.2.5) [250].

$$V = \frac{\sigma d}{\epsilon_0} - \left( \frac{t_1 \epsilon_{r2} + t_2 \epsilon_{r1} \sigma}{\epsilon_{r1} \epsilon_{r2}} + d \right) \frac{Q}{A \epsilon_0} \quad (4.2.6)$$

Eq. (4.2.7) is used for determining the theoretical charge density of both the surfaces of the TENG and  $V_{OC}$  is the value obtained from open-circuit voltage.

$$\sigma = \frac{V_{oc} \epsilon_0}{d} \quad (4.2.7)$$

When both the triboelectric charged surfaces comes back to their initial position, then the transferred charges (Q) could be calculated by Eq. (4.2.8).

$$Q = \frac{\sigma d \epsilon_{r1} \epsilon_{r2}}{t_1 \epsilon_{r2} + t_2 \epsilon_{r1} + d \epsilon_{r1} \epsilon_{r2}} \quad (4.2.8)$$

The charge density ( $\sigma$ ) and transferred charge density (Q) are calculated theoretically by using the above formulas, if the thickness of both the dielectric layers is known and hence the ratio of theoretical charge density to transferred charge density i.e.  $\sigma/Q$  is also calculated from the above formulas. Therefore, the electro-spinning technique is an uncomplicated technique to process the melts or solution of polymers into extremely thin fibers with various unique properties and features. Thus, the integration of F-GNRs into PVDF polymer and nylon polymers are easily available and cheap polymers.

In this work, we have tried to improve the performance using F-GNRs instead of rGONRs, because, fluorine is highly electronegative element in periodic table, so that, fluorination of rGONRs should improve the tribo-electronegativity of resulting filler (F-GNRs) and hence we can increase the tribo-electronegativity of prepared F-GNRs/PVDF composite. In the performance of TENG, surface morphology and tribo-electronegativity play crucial role [74,251,252]. F-GNRs/PVDF composite nanofibers based TENG exhibited higher output (4.59 V, 0.98 nA) as compared to pristine PVDF nanofiber based TENG (2.22 V, 54 nA). This improvement in the output of TENG is due to incorporation of F-GNRs. Therefore, from obtained TENG performance, it is clearly revealed that we have improved performance of TENG (4.59 V,

0.98 nA) using F-GNRs/PVDF nanofiber composite as compared to rGONRs/PVDF composite (0.35 V). But according to the reported literature, still electrical outputs are low. We have already mention in the section 4.1 of Chapter 4 (Results and Discussion), as our output low due to hand pressing, digital multimeter without any amplifier circuit measurement system and small contact area of triboelectric surfaces. These factors play key role to obtain higher output of fabricated TENG.





## Chapter 5

# SUMMARY AND CONCLUSIONS

---





## 5.1 Research Summary

In the earlier chapter, detailed results of this dissertation work have been discussed in two successive sections. This chapter summarizes the key findings of this work and assists in defining the scope of future work in this field.

In the first section, we have synthesized the rGONRs through unzipping of MWCNTs. The charge storage and transfer capability of rGONRs/PVDF have been revealed by cyclic voltammetry. Therefore, we have designed single electrode TENG based on charge transfer between Al and rGONRs/PVDF thin film with finite size supported by kapton tape and modulating distance. In this approach, obtained AC voltage through finger touching convinced mechanical energy by TENG. The maximum output voltage would be achieved by TENG is 0.35 V. TENG could be quite stable up to 500 cycles and the energy generated by the TENG would be stored or can be directly used to operate portable electronics devices. This proposed work demonstrates the practicability of nanogenerator in which the mechanical energy is utilized and convert it into electrical energy.

Thereafter, in the second and last section, we have successfully fabricated PVDF and F-GNRs incorporated nanofibers using electro-spinning approach. The fabricated vertical TENG using F-GNRs showed higher electrical outputs in comparison to pristine PVDF based TENG. This enhancement in electrical outputs due to incorporation of F-GNRs, which enlarge the electronegativity of pristine PVDF. The maximum short circuit current and open circuit voltage are observed to be 98 nA and 4.59 V, respectively for PVDF/F-GNRs based TENG. This TENG has the ability to light up 3 LEDs serially connected instantaneously by converting the mechanical energy generated by hand tapping. The fabricated TENG is quite stable for 2,000 cycles. If the generated electrical output is stored in the rechargeable battery, then it could be used to drive various portable electronic devices. This study significantly demonstrates the innovative development of TENG with hybrid material (PVDF/F-GNRs), which is prepared by the combination of organic and inorganic material.

## 5.2 Conclusions

The main conclusions of this dissertation work are as following:

- The incorporations of rGONRs in PVDF polymer matrix enhances the electronegativity, due to presence of various oxygen containing functional groups in the rGONRs, average surface roughness and charge trapping property of fabricated rGONRs/PVDF thin film, which leads to higher electrical outputs of TENG.
- As fluorine having higher electronegativity in comparison to oxygen, so we have performed the fluorination of rGONRs, for further enhancement in electronegativity of resulting materials (F-GNRs, PVDF/F-GNRs). Therefore, we obtained higher electrical outputs in PVDF/F-GNRs nanofibers based TENG in comparison to PVDF nanofibers based TENG.
- Finally, we have concluded that the selection of suitable materials, optimized structure and surface modified materials through chemical treatments are the three important factors, which contributes toward the higher electrical outputs.



**Chapter 6**

**SCOPE FOR FUTURE WORK**

---



The invention of the TENG has been examined as a key milestone in the field of harvesting mechanical energy generated from walking, running, pressing, water waves, winds, and so on, and turning it into electrical energy for self-powered systems. TENG has become an impressive technology due to its easy fabrication, cost effectiveness, high performance, easy scalability, diverse choice of materials, and high efficiency. A TENG could combine the electrostatic-induction and contact electrification effect, which harvests mechanical energy in the various forms including rotation, sliding, vibration, impact, etc. A TENG has many features such as light-weight, high output intensity, and trivial volume, which makes it very interesting in the field of energy harvesting.

In this regard, some of the directions for carrying out the future research based on this work are as follows:

- As the new surface engineering technologies and new materials have been introduced, they have improved the efficiency and overall performance of TENGs. So, an entirely new approach using inorganic and organic materials to convert mechanical energy into useful electrical energy.
- TENGs could be an effective and more feasible choice for constructing self-powered systems that are useful for driving small electronic devices such as, wearable electronics, portable devices, flexible electronics, etc.
- Additionally, they possibly have the ability to generate electricity on a large scale. Moreover, in the near future, TENGs will be hybridized with other technologies, such as thermal electric generators and solar cells, simultaneously to harvest many forms of energies and also store that energy.
- TENGs will be hybridized with energy storage units such as, super-capacitors, Li-ion batteries, etc. to form TENG as the self-charged power pack.

In nanotechnology, this may become the new paradigm for achieving self-powering micro/nano systems, which have diverse applications. Therefore, nanotechnology has the ability to overcome the critical problems that need to be addressed for the sustainable development of the economy. This could be the aim of nanotechnology now and in the future.



## REFERENCES

---

- [1] D. Evans, The Internet of things - How the next evolution of the internet is changing everything, CISCO White Pap. (2011) 1–11.
- [2] S.K. Karan, R. Bera, S. Paria, A.K. Das, S. Maiti, A. Maitra, B.B. Khatua, An approach to design highly durable piezoelectric nanogenerator based on self-poled PVDF/AlO-rGO flexible nanocomposite with high power density and energy conversion efficiency, *Adv. Energy Mater.* 6 (2016) 1–12.
- [3] A. Sultana, M.M. Alam, S. Garain, T.K. Sinha, T.R. Middy, D. Mandal, An effective electrical throughput from PANI supplement ZnS nanorods and PDMS-based flexible piezoelectric nanogenerator for power up portable electronic devices: An alternative of MWCNT filler, *ACS Appl. Mater. Interfaces.* 7 (2015) 19091–19097.
- [4] H.H. Singh, S. Singh, N. Khare, Enhanced  $\beta$ -phase in PVDF polymer nanocomposite and its application for nanogenerator, *Polym. Adv. Technol.* 29 (2018) 143–150.
- [5] P. Rajagopalan, V. Singh, I.A. Palani, Enhancement of ZnO-based flexible nano generators via a sol–gel technique for sensing and energy harvesting applications, *Nanotechnology.* 29 (2018) 105406.
- [6] R. Bhunia, S. Das, S. Dalui, S. Hussain, R. Paul, R. Bhar, A.K. Pal, Flexible nano-ZnO/polyvinylidene difluoride piezoelectric composite films as energy harvester, *Appl. Phys. A Mater. Sci. Process.* 122 (2016) 1–13.
- [7] D. Mandal, K. Henkel, D. Schmeißer, Improved performance of a polymer nanogenerator based on silver nanoparticles doped electrospun P(VDF–HFP) nanofibers, *Phys. Chem. Chem. Phys.* 16 (2014) 10403.
- [8] D. Dhakras, S. Ogale, high-performance organic–inorganic hybrid piezo-nanogenerator via interface enhanced polarization effects for self-powered electronic systems, *Adv. Mater. Interfaces.* 3 (2016) 1–9.
- [9] A.M. Roji M, J. G, A.B. Raj T, A retrospect on the role of piezoelectric nanogenerators in the development of the green world, *RSC Adv.* 7 (2017) 33642–33670.
- [10] N. Abinnas, P. Baskaran, S. Harish, R.S. Ganesh, M. Navaneethan, K.D. Nisha, S. Ponnusamy, C. Muthamizhchelvan, H. Ikeda, Y. Hayakawa, 0.8 V nanogenerator for mechanical energy harvesting using bismuth titanate–PDMS nanocomposite, *Appl. Surf. Sci.*

418 (2017) 362–368.

- [11] L. Chen, H. Guo, X. Xia, G. Liu, H. Shi, M. Wang, Y. Xi, C. Hu, Novel spiral-like electrode structure design for realization of two modes of energy harvesting, *ACS Appl. Mater. Interfaces*. 7 (2015) 16450–16457.
- [12] Z. Yang, J. Wang, J. Zhang, Research and development of micro electret power generators, *Sci. China Technol. Sci.* 55 (2012) 581–587.
- [13] F. Belhora, P.J. Cottinet, D. Guyomar, L. Lebrun, A. Hajjaji, M. Mazroui, Y. Boughaleb, Hybridization of electrostrictive polymers and electrets for mechanical energy harvesting, *Sensors Actuators A Phys.* 183 (2012) 50–56.
- [14] M.E. Karagozler, I. Poupyrev, G.K. Fedder, Y. Suzuki, Paper generators: Harvesting energy from touching, rubbing and sliding, *26th Annu. ACM Symp.* (2013) 23–30.
- [15] Y. Arakawa, Y. Suzuki, N. Kasagi, Micro seismic power generator using electret polymer film, *Proc. Natl. Symp. Power Energy Syst.* 2004.9 (2004) 37–38.
- [16] T.D. Lee, A.U. Ebong, A review of thin film solar cell technologies and challenges, *Renew. Sustain. Energy Rev.* 70 (2017) 1286–1297.
- [17] D. Roy, N. Tiwari, K. Mukhopadhyay, T. Shripathi, A.K. Saxena, The role of functional moieties on carbon nanotube surfaces in solar energy conversion, *ChemPhysChem*. 15 (2014) 3839–3847.
- [18] S. Saha, P. Das, A.K. Chakraborty, R. Debbarma, S. Sarkar, Hybrid solar cell with TiO<sub>2</sub> Film: BBOT polymer and copper phthalocyanine as sensitizer, *Adv. Electr. Electron. Eng.* 14 (2016) 345–351.
- [19] Z.L. Wang, Piezoelectric nanogenerators based on zinc oxide nanowire arrays, *Science* 312 (2006) 242–246.
- [20] U. Saha, R. Jaiswal, T.H. Goswami, A facile bulk production of processable partially reduced graphene oxide as superior supercapacitor electrode material, *Electrochim. Acta*. 196 (2016) 386–404.
- [21] Q. Cheng, Z. Song, T. Ma, B.B. Smith, R. Tang, H. Yu, H. Jiang, C.K. Chan, Folding paper-based lithium-ion batteries for higher areal energy densities, *Nano Lett.* 13 (2013) 4969–4974.
- [22] Y. Wang, Y. Song, Y. Xia, Electrochemical capacitors: mechanism, materials, systems, characterization and applications, *Chem. Soc. Rev.* 45 (2016) 5925–5950.
- [23] S. Hu, W. Li, M. Yao, T. Li, X. Liu, Electrophoretic deposition of gadolinium-doped ceria



- as a barrier layer on yttrium-stabilized zirconia electrolyte for solid oxide fuel cells, *Fuel Cells*. 17 (2017) 869–874.
- [24] S. Niaz, T. Manzoor, A.H. Pandith, Hydrogen storage: Materials, methods and perspectives, *Renew. Sustain. Energy Rev.* 50 (2015) 457–469.
- [25] S.K. Ghosh, T.K. Sinha, B. Mahanty, D. Mandal, Self-poled efficient flexible “Ferroelectretic” nanogenerator: A new class of piezoelectric energy harvester, *Energy Technol.* 3 (2015) 1190–1197.
- [26] X. Wang, J. Song, J. Liu, Z.L. Wang, Direct-current nanogenerator driven by ultrasonic waves, *Science* 316 (2007) 102–105.
- [27] Y. Qin, X. Wang, Z.L. Wang, Microfibre–nanowire hybrid structure for energy scavenging, *Nature*. 451 (2008) 809–813.
- [28] R. Yang, Y. Qin, L. Dai, Z.L. Wang, Power generation with laterally packaged piezoelectric fine wires., *Nat. Nanotechnol.* 4 (2009) 34–39.
- [29] C. Chang, V.H. Tran, J. Wang, Y.K. Fuh, L. Lin, Direct-write piezoelectric polymeric nanogenerator with high energy conversion efficiency, *Nano Lett.* 10 (2010) 726–731.
- [30] S. Xu, B.J. Hansen, Z.L. Wang, Piezoelectric-nanowire-enabled power source for driving wireless microelectronics, *Nat. Commun.* 1 (2010) 93.
- [31] S. Paria, S.K. Karan, R. Bera, A.K. Das, A. Maitra, B.B. Khatua, A facile approach to develop a highly stretchable PVC/ZnSnO<sub>3</sub> piezoelectric nanogenerator with high output power generation for powering portable electronic devices, *Ind. Eng. Chem. Res.* 55 (2016) 10671–10680.
- [32] P. Adhikary, D. Mandal, Enhanced electro-active phase in a luminescent P(VDF–HFP)/Zn<sup>2+</sup> flexible composite film for piezoelectric based energy harvesting applications and self-powered UV light detection, *Phys. Chem. Chem. Phys.* 19 (2017) 17789–17798.
- [33] S. Maiti, S.K. Karan, J. Lee, A.K. Mishra, B.B. Khatua, J.K. Kim, Bio-waste onion skin as an innovative nature-driven piezoelectric material with high energy conversion efficiency, *Nano Energy*. 42 (2017) 282–293.
- [34] S.K. Ghosh, A. Biswas, S. Sen, C. Das, K. Henkel, D. Schmeisser, D. Mandal, Yb<sup>3+</sup> assisted self-polarized PVDF based ferroelectretic nanogenerator: A facile strategy of highly efficient mechanical energy harvester fabrication, *Nano Energy*. 30 (2016) 621–629.
- [35] Y. Yang, S. Wang, Y. Zhang, Z.L. Wang, Pyroelectric nanogenerators for driving wireless sensors, *Nano Lett.* 12 (2012) 6408–6413.

- [36] Y. Yang, W. Guo, K.C. Pradel, G. Zhu, Y. Zhou, Y. Zhang, Y. Hu, L. Lin, Z.L. Wang, Pyroelectric nanogenerators for harvesting thermoelectric energy, *Nano Lett.* 12 (2012) 2833–2838.
- [37] Y. Yang, Y. Zhou, J.M. Wu, Z.L. Wang, Single micro/nanowire pyroelectric nanogenerators as self-powered temperature sensors, *ACS Nano.* 6 (2012) 8456–8461.
- [38] Y. Yang, J.H. Jung, B.K. Yun, F. Zhang, K.C. Pradel, W. Guo, Z.L. Wang, Flexible pyroelectric nanogenerators using a composite structure of lead-free  $\text{KNbO}_3$  nanowires, *Adv. Mater.* 24 (2012) 5357–5362.
- [39] Y. Yang, H. Zhang, G. Zhu, S. Lee, Z.H. Lin, Z.L. Wang, flexible hybrid energy cell for simultaneously harvesting thermal, mechanical, and solar energies, *ACS Nano.* 7 (2013) 785–790.
- [40] C.C. Hsiao, J.C. Ciou, A.S. Siao, C.Y. Lee, Temperature field analysis for PZT pyroelectric cells for thermal energy harvesting, *Sensors.* 11 (2011) 10458–10473.
- [41] C.S. Wei, Y.Y. Lin, Y.C. Hu, C.W. Wu, C.K. Shih, C.T. Huang, S.H. Chang, Partial-electroded ZnO pyroelectric sensors for responsivity improvement, *Sensors Actuators, A Phys.* 128 (2006) 18–24.
- [42] C.C. Hsiao, A.S. Siao, Improving pyroelectric energy harvesting using a sandblast etching technique, *Sensors.* 13 (2013) 12113–12131.
- [43] S.K. Ghosh, M. Xie, C.R. Bowen, P.R. Davies, D.J. Morgan, D. Mandal, A hybrid strain and thermal energy harvester based on an infra-red sensitive  $\text{Er}^{3+}$  modified poly(vinylidene fluoride) ferroelectret structure, *Sci. Rep.* 7 (2017) 1–13.
- [44] J. Peng, S.D. Kang, G.J. Snyder, Optimization principles and the figure of merit for triboelectric generators, *Sci. Adv.* 3 (2017) 1–7.
- [45] J. Cross, J.F. Hughes, *Electrostatics, principles, problems and applications*, Taylor & Francis, 1987.
- [46] G.M. Sessler, Physical principles of electrets, in: G.M. Sessler (Ed.), *Electrets*, Springer Berlin Heidelberg, Berlin, Heidelberg, 1987: pp. 13–80.
- [47] F.R. Fan, Z.Q. Tian, Z.L. Wang, Flexible triboelectric generator, *Nano Energy.* 1 (2012) 328–334.
- [48] S. Lee, H. Wang, Q. Shi, L. Dhakar, J. Wang, N. V. Thakor, S.C. Yen, C. Lee, Development of battery-free neural interface and modulated control of tibialis anterior muscle via common peroneal nerve based on triboelectric nanogenerators (TENGs), *Nano Energy.* 33 (2017) 1–

11.

- [49] C. Moganapriya, R. Rajasekar, K. Ponappa, R. Karthick, R.V. Perundurai, P.S. Kumar, S.K. Pal, Tribomechanical behavior of TiCN/TiAlN/WC-C multilayer film on cutting tool inserts for machining, *Mater. Test.* 59 (2017) 703–707.
- [50] J. Chen, G. Zhu, W. Yang, Q. Jing, P. Bai, Y. Yang, T.C. Hou, Z.L. Wang, Harmonic-resonator-based triboelectric nanogenerator as a sustainable power source and a self-powered active vibration sensor, *Adv. Mater.* 25 (2013) 6094–6099.
- [51] J. Zhong, Q. Zhong, F. Fan, Y. Zhang, S. Wang, B. Hu, Z.L. Wang, J. Zhou, Finger typing driven triboelectric nanogenerator and its use for instantaneously lighting up LEDs, *Nano Energy.* 2 (2013) 491–497.
- [52] X.S. Zhang, M.D. Han, R.X. Wang, F.Y. Zhu, Z.H. Li, W. Wang, H.X. Zhang, Frequency-multiplication high-output triboelectric nanogenerator for sustainably powering biomedical microsystems, *Nano Lett.* 13 (2013) 1168–1172.
- [53] W. Yang, J. Chen, G. Zhu, J. Yang, P. Bai, Y. Su, Q. Jing, X. Cao, Z.L. Wang, Harvesting energy from the natural vibration of human walking, *ACS Nano.* 7 (2013) 11317–11324.
- [54] G. Zhu, P. Bai, J. Chen, Z.L. Wang, Power-generating shoe insole based on triboelectric nanogenerators for self-powered consumer electronics, *Nano Energy.* 2 (2013) 688–692.
- [55] T.C. Hou, Y. Yang, H. Zhang, J. Chen, L.J. Chen, Z.L. Wang, Triboelectric nanogenerator built inside shoe insole for harvesting walking energy, *Nano Energy.* 2 (2013) 856–862.
- [56] S. Wang, L. Lin, Y. Xie, Q. Jing, S. Niu, Z.L. Wang, Sliding-triboelectric nanogenerators based on in-plane charge-separation mechanism, *Nano Lett.* 13 (2013) 2226–2233.
- [57] G. Zhu, J. Chen, Y. Liu, P. Bai, Y.S. Zhou, Q. Jing, C. Pan, Z.L. Wang, Linear-grating triboelectric generator based on sliding electrification, *Nano Lett.* 13 (2013) 2282–2289.
- [58] S. Niu, Y. Liu, S. Wang, L. Lin, Y.S. Zhou, Y. Hu, Z.L. Wang, Theory of sliding-mode triboelectric nanogenerators, *Adv. Mater.* 25 (2013) 6184–6193.
- [59] S. Niu, S. Wang, Y. Liu, Y.S. Zhou, L. Lin, Y. Hu, K.C. Pradel, Z.L. Wang, A theoretical study of grating structured triboelectric nanogenerators, *Energy Environ. Sci.* 7 (2014) 2339–2349.
- [60] C. Han, C. Zhang, W. Tang, X. Li, Z.L. Wang, High power triboelectric nanogenerator based on printed circuit board (PCB) technology, *Nano Res.* 8 (2015) 722–730.
- [61] P. Bai, G. Zhu, Y. Liu, J. Chen, Q. Jing, W. Yang, J. Ma, G. Zhang, Z.L. Wang, Cylindrical rotating triboelectric nanogenerator, *ACS Nano.* 7 (2013) 6361–6366.

- [62] L. Lin, S. Wang, Y. Xie, Q. Jing, S. Niu, Y. Hu, Z.L. Wang, Segmentally structured disk triboelectric nanogenerator for harvesting rotational mechanical energy, *Nano Lett.* 13 (2013) 2916–2923.
- [63] C. Zhang, T. Zhou, W. Tang, C. Han, L. Zhang, Z.L. Wang, Rotating-disk-based direct-current triboelectric nanogenerator, *Adv. Energy Mater.* 4 (2014) 1301798.
- [64] Q. Jing, G. Zhu, P. Bai, Y. Xie, J. Chen, R.P.S. Han, Z.L. Wang, Case-encapsulated triboelectric nanogenerator for harvesting energy from reciprocating sliding motion, *ACS Nano.* 8 (2014) 3836–3842.
- [65] Y. Xie, S. Wang, S. Niu, L. Lin, Q. Jing, Y. Su, Z. Wu, Z.L. Wang, Multi-layered disk triboelectric nanogenerator for harvesting hydropower, *Nano Energy.* 6 (2014) 129–136.
- [66] Y. Xie, S. Wang, L. Lin, Q. Jing, Z.H. Lin, S. Niu, Z. Wu, Z.L. Wang, Rotary triboelectric nanogenerator based on a hybridized mechanism for harvesting wind energy, *ACS Nano.* 7 (2013) 7119–7125.
- [67] Y. Yang, H. Zhang, J. Chen, Q. Jing, Y.S. Zhou, X. Wen, Z.L. Wang, Single-electrode-based sliding triboelectric nanogenerator for self-powered displacement vector sensor system, *ACS Nano.* 7 (2013) 7342–7351.
- [68] Y. Yang, Y.S. Zhou, H. Zhang, Y. Liu, S. Lee, Z.L. Wang, A single-electrode based triboelectric nanogenerator as self-powered tracking system, *Adv. Mater.* 25 (2013) 6594–6601.
- [69] Q. Liang, X. Yan, Y. Gu, K. Zhang, M. Liang, S. Lu, X. Zheng, Y. Zhang, Highly transparent triboelectric nanogenerator for harvesting water-related energy reinforced by antireflection coating, *Sci. Rep.* 5 (2015) 9080.
- [70] Q. Zhong, J. Zhong, B. Hu, Q. Hu, J. Zhou, Z.L. Wang, A paper-based nanogenerator as a power source and active sensor, *Energy Environ. Sci.* 6 (2013) 1779.
- [71] Y. Yang, G. Zhu, H. Zhang, J. Chen, X. Zhong, Z.H. Lin, Y. Su, P. Bai, X. Wen, Z.L. Wang, Triboelectric nanogenerator for harvesting wind energy and as self-powered wind vector sensor system, *ACS Nano.* 7 (2013) 9461–9468.
- [72] H. Zhang, Y. Yang, X. Zhong, Y. Su, Y. Zhou, C. Hu, Z.L. Wang, Single-electrode-based rotating triboelectric nanogenerator for harvesting energy from tires, *ACS Nano.* 8 (2014) 680–689.
- [73] S. Wang, Y. Xie, S. Niu, L. Lin, Z.L. Wang, Freestanding triboelectric-layer-based nanogenerators for harvesting energy from a moving object or human motion in contact and

- non-contact modes, *Adv. Mater.* 26 (2014) 2818–2824.
- [74] Z.L. Wang, Triboelectric nanogenerators as new energy technology and self-powered sensors – Principles, problems and perspectives, *Faraday Discuss.* 176 (2014) 447–458.
- [75] L. Lin, Y. Xie, S. Niu, S. Wang, P.K. Yang, Z.L. Wang, Robust triboelectric nanogenerator based on rolling electrification and electrostatic induction at an instantaneous energy conversion efficiency of ~55%, *ACS Nano.* 9 (2015) 922–930.
- [76] S. Niu, Y. Liu, S. Wang, L. Lin, Y.S. Zhou, Y. Hu, Z.L. Wang, Theoretical investigation and structural optimization of single-electrode triboelectric nanogenerators, *Adv. Funct. Mater.* 24 (2014) 3332–3340.
- [77] M. Zhu, Y. Huang, W.S. Ng, J. Liu, Z. Wang, Z. Wang, H. Hu, C. Zhi, 3D spacer fabric based multifunctional triboelectric nanogenerator with great feasibility for mechanized large-scale production, *Nano Energy.* 27 (2016) 439–446.
- [78] H. Chu, H. Jang, Y. Lee, Y. Chae, J.H. Ahn, Conformal, graphene-based triboelectric nanogenerator for self-powered wearable electronics, *Nano Energy.* 27 (2016) 298–305.
- [79] J. Yang, J. Chen, Y. Yang, H. Zhang, W. Yang, P. Bai, Y. Su, Z.L. Wang, Broadband vibrational energy harvesting based on a triboelectric nanogenerator, *Adv. Energy Mater.* 4 (2014) 1–9.
- [80] L. Dhakar, P. Pitchappa, F.E.H. Tay, C. Lee, An intelligent skin based self-powered finger motion sensor integrated with triboelectric nanogenerator, *Nano Energy.* 19 (2016) 532–540.
- [81] F.R. Fan, L. Lin, G. Zhu, W. Wu, R. Zhang, Z.L. Wang, Transparent triboelectric nanogenerators and self-powered pressure sensors based on micropatterned plastic films, *Nano Lett.* 12 (2012) 3109–3114.
- [82] L. Lin, Y. Xie, S. Wang, W. Wu, S. Niu, X. Wen, Z.L. Wang, Triboelectric active sensor array for self-powered static and dynamic pressure detection and tactile imaging, *ACS Nano.* 7 (2013) 8266–8274.
- [83] H. Zhang, Y. Yang, Y. Su, J. Chen, K. Adams, S. Lee, C. Hu, Z.L. Wang, Triboelectric nanogenerator for harvesting vibration energy in full space and as self-powered acceleration sensor, *Adv. Funct. Mater.* 24 (2014) 1401–1407.
- [84] B. Meng, W. Tang, Z.H. Too, X.S. Zhang, M.D. Han, W. Liu, H.X. Zhang, A transparent single-friction-surface triboelectric generator and self-powered touch sensor, *Energy Environ. Sci.* 6 (2013) 3235–3240.
- [85] J. Zhong, Y. Zhang, Q. Zhong, Q. Hu, B. Hu, Z.L. Wang, J. Zhou, Fiber-based generator for

wearable electronics and mobile medication, *ACS Nano*. 8 (2014) 6273–6280.

- [86] Z. Zhang, J. He, T. Wen, C. Zhai, J. Han, J. Mu, W. Jia, B. Zhang, W. Zhang, X. Chou, C. Xue, Magnetically levitated-triboelectric nanogenerator as a self-powered vibration monitoring sensor, *Nano Energy*. 33 (2017) 88–97.
- [87] Z.H. Lin, G. Zhu, Y.S. Zhou, Y. Yang, P. Bai, J. Chen, Z.L. Wang, A self-powered triboelectric nanosensor for mercury ion detection, *Angew. Chemie - Int. Ed.* 52 (2013) 5065–5069.
- [88] Z.H. Lin, G. Cheng, L. Lin, S. Lee, Z.L. Wang, Water-solid surface contact electrification and its use for harvesting liquid-wave energy, *Angew. Chemie - Int. Ed.* 52 (2013) 12545–12549.
- [89] W. Tang, Y. Han, C.B. Han, C.Z. Gao, X. Cao, Z.L. Wang, Self-powered water splitting using flowing kinetic energy, *Adv. Mater.* 27 (2015) 272–276.
- [90] J. Chen, G. Zhu, J. Yang, Q. Jing, P. Bai, W. Yang, X. Qi, Y. Su, Z.L. Wang, Personalized keystroke dynamics for self-powered human-machine interfacing, *ACS Nano*. 9 (2015) 105–116.
- [91] Y. Zi, J. Wang, S. Wang, S. Li, Z. Wen, H. Guo, Z.L. Wang, Effective energy storage from a triboelectric nanogenerator., *Nat. Commun.* 7 (2016) 10987.
- [92] Z.H. Lin, G. Cheng, X. Li, P.K. Yang, X. Wen, Z.L. Wang, A multi-layered interdigitated-electrodes-based triboelectric nanogenerator for harvesting hydropower, *Nano Energy*. 15 (2015) 256–265.
- [93] L. Zheng, Z.H. Lin, G. Cheng, W. Wu, X. Wen, S. Lee, Z.L. Wang, Silicon-based hybrid cell for harvesting solar energy and raindrop electrostatic energy, *Nano Energy*. 9 (2014) 291–300.
- [94] M.L. Seol, S.B. Jeon, J.W. Han, Y.K. Choi, Ferrofluid-based triboelectric-electromagnetic hybrid generator for sensitive and sustainable vibration energy harvesting, *Nano Energy*. 31 (2017) 233–238.
- [95] H. Moon, J. Chung, B. Kim, H. Yong, T. Kim, S. Lee, S. Lee, Stack/flutter-driven self-retracting triboelectric nanogenerator for portable electronics, *Nano Energy*. 31 (2017) 525–532.
- [96] Y. Zi, H. Guo, J. Wang, Z. Wen, S. Li, C. Hu, Z.L. Wang, An inductor-free auto-power-management design built-in triboelectric nanogenerators, *Nano Energy*. 31 (2016) 302–310.
- [97] J.M. Wu, C.K. Chang, Y.T. Chang, High-output current density of the triboelectric

- nanogenerator made from recycling rice husks, *Nano Energy*. 19 (2016) 39–47.
- [98] D. Jang, Y. Kim, T.Y. Kim, K. Koh, U. Jeong, J. Cho, Force-assembled triboelectric nanogenerator with high-humidity-resistant electricity generation using hierarchical surface morphology, *Nano Energy*. 20 (2016) 283–293.
- [99] Y. Feng, Y. Zheng, S. Ma, D. Wang, F. Zhou, W. Liu, High output polypropylene nanowire array triboelectric nanogenerator through surface structural control and chemical modification, *Nano Energy*. 19 (2016) 48–57.
- [100] K.N. Kim, Y.K. Jung, J. Chun, B.U. Ye, M. Gu, E. Seo, S. Kim, S.W. Kim, B.S. Kim, J.M. Baik, Surface dipole enhanced instantaneous charge pair generation in triboelectric nanogenerator, *Nano Energy*. 26 (2016) 360–370.
- [101] S.J. Park, M.L. Seol, D. Kim, S.B. Jeon, Y.K. Choi, Triboelectric nanogenerator with nanostructured metal surface using water-assisted oxidation, *Nano Energy*. 21 (2016) 258–264.
- [102] X. Wang, Z.L. Wang, Y. Yang, Hybridized nanogenerator for simultaneously scavenging mechanical and thermal energies by electromagnetic-triboelectric-thermoelectric effects, *Nano Energy*. 26 (2016) 164–171.
- [103] C. Jin, D.S. Kia, M. Jones, S. Towfighian, On the contact behavior of micro-/nano-structured interface used in vertical-contact-mode triboelectric nanogenerators, *Nano Energy*. 27 (2016) 68–77.
- [104] W.G. Kim, I.W. Tcho, D. Kim, S.B. Jeon, S.J. Park, M.L. Seol, Y.K. Choi, Performance-enhanced triboelectric nanogenerator using the glass transition of polystyrene, *Nano Energy*. 27 (2016) 306–312.
- [105] J. Wang, Z. Wen, Y. Zi, L. Lin, C. Wu, H. Guo, Y. Xi, Y. Xu, Z.L. Wang, Self-powered electrochemical synthesis of polypyrrole from the pulsed output of a triboelectric nanogenerator as a sustainable energy system, *Adv. Funct. Mater.* 26 (2016) 3542–3548.
- [106] C. Yao, A. Hernandez, Y. Yu, Z. Cai, X. Wang, Triboelectric nanogenerators and powerboards from cellulose nanofibrils and recycled materials, *Nano Energy*. 30 (2016) 103–108.
- [107] L.B. Huang, W. Xu, G. Bai, M.C. Wong, Z. Yang, J. Hao, Wind energy and blue energy harvesting based on magnetic-assisted noncontact triboelectric nanogenerator, *Nano Energy*. 30 (2016) 36–42.
- [108] Q. Liang, X. Yan, X. Liao, Y. Zhang, Integrated multi-unit transparent triboelectric nanogenerator harvesting rain power for driving electronics, *Nano Energy*. 25 (2016) 18–

25.

- [109] W. Kim, H.J. Hwang, D. Bhatia, Y. Lee, J.M. Baik, D. Choi, Kinematic design for high performance triboelectric nanogenerators with enhanced working frequency, *Nano Energy*. 21 (2016) 19–25.
- [110] L. Dhakar, S. Gudla, X. Shan, Z. Wang, F.E.H. Tay, C.H. Heng, C. Lee, Large scale triboelectric nanogenerator and self-powered pressure sensor array using low cost roll-to-roll UV embossing, *Sci. Rep.* 6 (2016) 22253.
- [111] Y. Zhu, B. Yang, J. Liu, X. Wang, L. Wang, X. Chen, C. Yang, A flexible and biocompatible triboelectric nanogenerator with tunable internal resistance for powering wearable devices., *Sci. Rep.* 6 (2016) 22233.
- [112] Y. Mao, N. Zhang, Y. Tang, M. Wang, M. Chao, E. Liang, A paper triboelectric nanogenerator for self-powered electronic systems, *Nanoscale*. 9 (2017) 14499–14505.
- [113] Y. Su, G. Xie, S. Wang, H. Tai, Q. Zhang, H. Du, H. Zhang, X. Du, Y. Jiang, Novel high-performance self-powered humidity detection enabled by triboelectric effect, *Sensors Actuators B Chem.* 251 (2017) 144–152.
- [114] Q. Shi, H. Wang, H. Wu, C. Lee, Self-powered triboelectric nanogenerator buoy ball for applications ranging from environment monitoring to water wave energy farm, *Nano Energy*. 40 (2017) 203–213.
- [115] W. Xu, L.B.B. Huang, J. Hao, Fully self-healing and shape-tailorable triboelectric nanogenerators based on healable polymer and magnetic-assisted electrode, *Nano Energy*. 40 (2017) 399–407.
- [116] G. Cheng, H. Zheng, F. Yang, L. Zhao, M. Zheng, J. Yang, U. States, H. Qin, Z. Du, Z.L. Wang, Managing and maximizing the output power of a triboelectric nanogenerator by controlled tip–electrode air-discharging and application for UV sensing, *Nano Energy*. 44 (2017) 208–216.
- [117] J. Shen, Z. Li, J. Yu, B. Ding, Humidity-resisting triboelectric nanogenerator for high performance biomechanical energy harvesting, *Nano Energy*. 40 (2017) 282–288.
- [118] F. Xing, Y. Jie, X. Cao, T. Li, N. Wang, Natural triboelectric nanogenerator based on soles for harvesting low-frequency walking energy, *Nano Energy*. 42 (2017) 138–142.
- [119] Y. Dong, S.S.K. Mallineni, K. Maleski, H. Behlow, V.N. Mochalin, A.M. Rao, Y. Gogotsi, R. Podila, Metallic MXenes: A new family of materials for flexible triboelectric nanogenerators, *Nano Energy*. 44 (2018) 103–110.



- [120] Y. Chen, M. Wang, M. Tian, Y. Zhu, X. Wei, T. Jiang, S. Gao, An innovative electro-fenton degradation system self-powered by triboelectric nanogenerator using biomass-derived carbon materials as cathode catalyst, *Nano Energy*. 42 (2017) 314–321.
- [121] B. Dudem, N.D. Huynh, W. Kim, D.H. Kim, H.J. Hwang, D. Choi, J.S. Yu, Nanopillar-array architected PDMS-based triboelectric nanogenerator integrated with a windmill model for effective wind energy harvesting, *Nano Energy*. 42 (2017) 269–281.
- [122] G.H. Lim, S.S. Kwak, N. Kwon, T. Kim, H. Kim, S.M. Kim, S.W. Kim, B. Lim, Fully stretchable and highly durable triboelectric nanogenerators based on gold-nanosheet electrodes for self-powered human-motion detection, *Nano Energy*. 42 (2017) 300–306.
- [123] I.W. Tcho, W.G. Kim, S.B. Jeon, S.J. Park, B.J. Lee, H.K. Bae, D. Kim, Y.K. Choi, Surface structural analysis of a friction layer for a triboelectric nanogenerator, *Nano Energy*. 42 (2017) 34–42.
- [124] C.C. Jin, X.C. Liu, H.H. Fan, Y. Wang, H.L. Hwang, Y.F. Zhang, Q. Wang, Fabrication and structure of lead-free BCTZ-MWCNTs composite and its application in energy harvesting, *Ceram. Int.* 43 (2017) 15886–15890.
- [125] A.S.M.I. Uddin, G.S. Chung, Wide-ranging impact-competent self-powered active sensor using a stacked corrugated-core sandwich-structured robust triboelectric nanogenerator, *Sensors Actuators B Chem.* 245 (2017) 1–10.
- [126] M.L. Seol, J.W. Han, D.I. Moon, M. Meyyappan, Triboelectric nanogenerator for Mars environment, *Nano Energy*. 39 (2017) 238–244.
- [127] L. Jin, J. Tao, R. Bao, L. Sun, C. Pan, Self-powered real-time movement monitoring sensor using triboelectric nanogenerator technology, *Sci. Rep.* 7 (2017) 10521.
- [128] H. Peng, X. Fang, S. Ranaei, Z. Wen, A.L. Porter, Forecasting potential sensor applications of triboelectric nanogenerators through tech mining, *Nano Energy*. 35 (2017) 358–369.
- [129] X. Li, J. Tao, J. Zhu, C. Pan, A nanowire based triboelectric nanogenerator for harvesting water wave energy and its applications, *APL Mater.* 5 (2017) 74104.
- [130] D. Yoo, D. Choi, D.S. Kim, Comb-shaped electrode-based triboelectric nanogenerators for bi-directional mechanical energy harvesting, *Microelectron. Eng.* 174 (2017) 46–51.
- [131] A. Ahmed, S.L. Zhang, I. Hassan, Z. Saadatnia, Y. Zi, J. Zu, Z.L. Wang, A washable, stretchable, and self-powered human-machine interfacing triboelectric nanogenerator for wireless communications and soft robotics pressure sensor arrays, *Extrem. Mech. Lett.* 13 (2017) 25–35.

- [132] X. Ren, H. Fan, C. Wang, J. Ma, S. Lei, Y. Zhao, H. Li, N. Zhao, Magnetic force driven noncontact electromagnetic-triboelectric hybrid nanogenerator for scavenging biomechanical energy, *Nano Energy*. 35 (2017) 233–241.
- [133] S.S.K. Mallineni, H. Behlow, Y. Dong, S. Bhattacharya, A.M. Rao, R. Podila, Facile and robust triboelectric nanogenerators assembled using off-the-shelf materials, *Nano Energy*. 35 (2017) 263–270.
- [134] W. Xu, L.B. Huang, M.C. Wong, L. Chen, G. Bai, J. Hao, Environmentally friendly hydrogel-based triboelectric nanogenerators for versatile energy harvesting and self-powered sensors, *Adv. Energy Mater.* 7 (2017) 1601529.
- [135] J.P. Lee, B.U. Ye, K.N. Kim, J.W. Lee, W.J. Choi, J.M. Baik, 3D printed noise-cancelling triboelectric nanogenerator, *Nano Energy*. 38 (2017) 377–384.
- [136] A. Ahmed, I. Hassan, M. Hedaya, T.A. El-Yazid, J. Zu, Z.L. Wang, Farms of triboelectric nanogenerators for harvesting wind energy: A potential approach towards green energy, *Nano Energy*. 36 (2017) 21–29.
- [137] J. Qian, X. Wu, D.S. Kima, D.W. Lee, Seesaw-structured triboelectric nanogenerator for scavenging electrical energy from rotational motion of mechanical systems, *Sensors Actuators A Phys.* 263 (2017) 600–609.
- [138] Z.L. Wang, T. Jiang, L. Xu, Toward the blue energy dream by triboelectric nanogenerator networks, *Nano Energy*. 39 (2017) 9–23.
- [139] Y. Xi, J. Wang, Y. Zi, X. Li, C. Han, X. Cao, C. Hu, Z. Wang, High efficient harvesting of underwater ultrasonic wave energy by triboelectric nanogenerator, *Nano Energy*. 38 (2017) 101–108.
- [140] J.H. Park, K.J. Park, T. Jiang, Q. Sun, J. Huh, Z.L. Wang, S. Lee, J.H. Cho, Light-transformable and -healable triboelectric nanogenerators, *Nano Energy*. 38 (2017) 412–418.
- [141] X. Chen, Y. Song, Z. Su, H. Chen, X. Cheng, J. Zhang, M. Han, H. Zhang, Flexible fiber-based hybrid nanogenerator for biomechanical energy harvesting and physiological monitoring, *Nano Energy*. 38 (2017) 43–50.
- [142] Y. Lee, W. Kim, D. Bhatia, H.J. Hwang, S. Lee, D. Choi, Cam-based sustainable triboelectric nanogenerators with a resolution-free 3D-printed system, *Nano Energy*. 38 (2017) 326–334.
- [143] X. Chen, Y. Wu, A. Yu, L. Xu, L. Zheng, Y. Liu, H. Li, Z.L. Wang, Self-powered modulation of elastomeric optical grating by using triboelectric nanogenerator, *Nano*

Energy. 38 (2017) 91–100.

- [144] C. Wu, R. Liu, J. Wang, Y. Zi, L. Lin, Z.L. Wang, A spring-based resonance coupling for hugely enhancing the performance of triboelectric nanogenerators for harvesting low-frequency vibration energy, *Nano Energy*. 32 (2017) 287–293.
- [145] F. Xi, Y. Pang, W. Li, T. Jiang, L. Zhang, T. Guo, G. Liu, C. Zhang, Z.L. Wang, Universal power management strategy for triboelectric nanogenerator, *Nano Energy*. 37 (2017) 168–176.
- [146] X. Chen, X. Pu, T. Jiang, A. Yu, L. Xu, Z.L. Wang, Tunable optical modulator by coupling a triboelectric nanogenerator and a dielectric elastomer, *Adv. Funct. Mater.* 27 (2017) 1603788.
- [147] J.G. Sun, T.N. Yang, I.S. Kuo, J.M. Wu, C.Y. Wang, L.J. Chen, A leaf-molded transparent triboelectric nanogenerator for smart multifunctional applications, *Nano Energy*. 32 (2017) 180–186.
- [148] M.L. Seol, J.W. Han, D.I. Moon, M. Meyyappan, Hysteretic behaviour of contact force response in triboelectric nanogenerator, *Nano Energy*. 32 (2017) 408–413.
- [149] W. Liu, C. Zhang, H. Lin, W. Qu, X. Li, X. Wang, Texture and sliding motion sensation with a triboelectric-nanogenerator transducer, *Sensors Actuators A Phys.* 256 (2017) 89–94.
- [150] S. Park, H. Ryu, S. Park, H. Hong, H.Y. Jung, J.J. Park, Rotating triboelectric generator using sliding contact and noncontact from 1D fiber friction, *Nano Energy*. 33 (2017) 184–194.
- [151] X. Ren, H. Fan, J. Ma, C. Wang, Y. Zhao, S. Lei, Triboelectric nanogenerators based on fluorinated wasted rubber powder for self-powering application, *ACS Sustain. Chem. Eng.* 5 (2017) 1957–1964.
- [152] H.J. Kim, E.C. Yim, J.H. Kim, S.J. Kim, J.Y. Park, I.K. Oh, Bacterial nano-cellulose triboelectric nanogenerator, *Nano Energy*. 33 (2017) 130–137.
- [153] H. Phan, D.M. Shin, S.H. Jeon, T.Y. Kang, P. Han, G.H. Kim, H.K. Kim, K. Kim, Y.H. Hwang, S.W. Hong, Aerodynamic and aeroelastic flutters driven triboelectric nanogenerators for harvesting broadband airflow energy, *Nano Energy*. 33 (2017) 476–484.
- [154] Q. Liang, Q. Zhang, X. Yan, X. Liao, L. Han, F. Yi, M. Ma, Y. Zhang, Recyclable and green triboelectric nanogenerator, *Adv. Mater.* 29 (2017) 1604961.
- [155] B. Yu, H. Yu, H. Wang, Q. Zhang, M. Zhu, High-power triboelectric nanogenerator prepared from electrospun mats with spongy parenchyma-like structure, *Nano Energy*. 34 (2017) 69–

- [156] X. He, Y. Zi, H. Guo, H. Zheng, Y. Xi, C. Wu, J. Wang, W. Zhang, C. Lu, Z.L. Wang, A highly stretchable fiber-based triboelectric nanogenerator for self-powered wearable electronics, *Adv. Funct. Mater.* 27 (2017) 1604378.
- [157] J. Wang, H. Zhang, Y. Xie, Z. Yan, Y. Yuan, L. Huang, X. Cui, M. Gao, Y. Su, W. Yang, Y. Lin, Smart network node based on hybrid nanogenerator for self-powered multifunctional sensing, *Nano Energy.* 33 (2017) 418–426.
- [158] J. Gong, B. Xu, X. Tao, Breath figure micromolding approach for regulating the microstructures of polymeric films for triboelectric nanogenerators, *ACS Appl. Mater. Interfaces.* 9 (2017) 4988–4997.
- [159] X. Chen, M. Han, H. Chen, X. Cheng, Y. Song, Z. Su, Y. Jiang, H.A. Zhang, Wavy-shaped hybrid piezoelectric and triboelectric nanogenerator based on P(VDF-TrFE) nanofibers, *Nanoscale.* 24 (2016) 1263–1270.
- [160] D. Ali, B. Yu, X. Duan, H. Yu, M. Zhu, Enhancement of output performance through post-poling technique on BaTiO<sub>3</sub>/PDMS-based triboelectric nanogenerator, *Nanotechnology.* 28 (2017) 75203.
- [161] Y. Pang, J. Li, T. Zhou, Z. Yang, J. Luo, L. Zhang, G. Dong, C. Zhang, Z.L. Wang, Flexible transparent tribotronic transistor for active modulation of conventional electronics, *Nano Energy.* 31 (2017) 533–540.
- [162] L. Xu, Y. Pang, C. Zhang, T. Jiang, X. Chen, J. Luo, W. Tang, X. Cao, Z.L. Wang, Integrated triboelectric nanogenerator array based on air-driven membrane structures for water wave energy harvesting, *Nano Energy.* 31 (2017) 351–358.
- [163] Y.C. Lai, J. Deng, S.L. Zhang, S. Niu, H. Guo, Z.L. Wang, Single-thread-based wearable and highly stretchable triboelectric nanogenerators and their applications in cloth-based self-powered human-interactive and biomedical sensing, *Adv. Funct. Mater.* 27 (2017) 1604462.
- [164] S.W. Chen, X. Cao, N. Wang, L. Ma, H.R. Zhu, M. Willander, Y. Jie, Z.L. Wang, An ultrathin flexible single-electrode triboelectric-nanogenerator for mechanical energy harvesting and instantaneous force sensing, *Adv. Energy Mater.* 7 (2017) 1601255.
- [165] X. Xia, J. Chen, G. Liu, M.S. Javed, X. Wang, C. Hu, Aligning graphene sheets in PDMS for improving output performance of triboelectric nanogenerator, *Carbon* 111 (2017) 569–576.
- [166] T. Jiang, Y. Yao, L. Xu, L. Zhang, T. Xiao, Z.L. Wang, Spring-assisted triboelectric

- nanogenerator for efficiently harvesting water wave energy, *Nano Energy*. 31 (2017) 560–567.
- [167] Q. Jiang, C. Wu, Z. Wang, A.C. Wang, J.H. He, Z.L. Wang, H.N. Alshareef, MXene electrochemical microsupercapacitor integrated with triboelectric nanogenerator as a wearable self-charging power unit, *Nano Energy*. 45 (2018) 266–272.
- [168] T. Guo, G. Liu, Y. Pang, B. Wu, F. Xi, J. Zhao, T. Bu, X. Fu, X. Li, C. Zhang, Z.L. Wang, Compressible hexagonal-structured triboelectric nanogenerators for harvesting tire rotation energy, *Extrem. Mech. Lett.* 18 (2018) 1–8.
- [169] J. Chen, X. Pu, H. Guo, Q. Tang, L. Feng, X. Wang, C. Hu, A self-powered 2D barcode recognition system based on sliding mode triboelectric nanogenerator for personal identification, *Nano Energy*. 43 (2018) 253–258.
- [170] R. Pan, W. Xuan, J. Chen, S. Dong, H. Jin, X. Wang, H. Li, J. Luo, Fully biodegradable triboelectric nanogenerators based on electrospun polylactic acid and nanostructured gelatin films, *Nano Energy*. 45 (2018) 193–202.
- [171] B. Chen, N. Yang, Q. Jiang, W. Chen, Y. Yang, Transparent triboelectric nanogenerator-induced high voltage pulsed electric field for a self-powered handheld printer, *Nano Energy*. 44 (2018) 468–475.
- [172] C. He, W. Zhu, G.Q. Gu, T. Jiang, L. Xu, B.D. Chen, C.B. Han, D. Li, Z.L. Wang, Integrative square-grid triboelectric nanogenerator as a vibrational energy harvester and impulsive force sensor, *Nano Res.* 11 (2018) 1157–1164.
- [173] Y. Jie, X. Jia, J. Zou, Y. Chen, N. Wang, Z.L. Wang, X. Cao, Natural leaf made triboelectric nanogenerator for harvesting environmental mechanical energy, *Adv. Energy Mater.* 8 (2018) 1703133.
- [174] J. Chung, H. Yong, H. Moon, S.T. Choi, D. Bhatia, D. Choi, D. Kim, S. Lee, Capacitor-integrated triboelectric nanogenerator based on metal-metal contact for current amplification, *Adv. Energy Mater.* 1703024 (2018) 1703024.
- [175] D. Kim, S. Lee, Y. Ko, C.H. Kwon, J. Cho, Layer-by-layer assembly-induced triboelectric nanogenerators with high and stable electric outputs in humid environments, *Nano Energy*. 44 (2018) 228–239.
- [176] M.F. Lin, J. Xiong, J. Wang, K. Parida, P.S. Lee, Core-shell nanofiber mats for tactile pressure sensor and nanogenerator applications, *Nano Energy*. 44 (2018) 248–255.
- [177] B. Chen, Y. Yang, Z.L. Wang, Scavenging wind energy by triboelectric nanogenerators,

- Adv. Energy Mater. 1702649 (2018) 1–13.
- [178] Y. Bian, T. Jiang, T. Xiao, W. Gong, X. Cao, Z. Wang, Z.L. Wang, Triboelectric nanogenerator tree for harvesting wind energy and illuminating in subway tunnel, Adv. Mater. Technol. 3 (2018) 1700317.
- [179] P. Vasandani, B. Gattu, Z.H. Mao, W. Jia, M. Sun, Using a synchronous switch to enhance output performance of triboelectric nanogenerators, Nano Energy. 43 (2018) 210–218.
- [180] J. Zou, M. Zhang, J. Huang, J. Bian, Y. Jie, M. Willander, X. Cao, N. Wang, Z.L. Wang, Coupled supercapacitor and triboelectric nanogenerator boost biomimetic pressure sensor, Adv. Energy Mater. 1702671 (2018) 1–8.
- [181] Z. Tian, J. He, X. Chen, T. Wen, C. Zhai, Z. Zhang, J. Cho, X. Chou, C. Xue, Core–shell coaxially structured triboelectric nanogenerator for energy harvesting and motion sensing, RSC Adv. 8 (2018) 2950–2957.
- [182] B. Dudem, D.H. Kim, J.S. Yu, Triboelectric nanogenerators with gold-thin-film-coated conductive textile as floating electrode for scavenging wind energy, Nano Res. 11 (2018) 101–113.
- [183] C. Wu, T.W. Kima, S. Sung, J.H. Park, F. Li, Ultrasoft and cuttable paper-based triboelectric nanogenerators for mechanical energy harvesting, Nano Energy. 44 (2018) 279–287.
- [184] C. Cui, X. Wang, Z. Yi, B. Yang, X. Wang, X. Chen, J.Q. Liu, C. Yang, Flexible single-electrode triboelectric nanogenerator and body moving sensor based on porous Na<sub>2</sub>CO<sub>3</sub>/Polydimethylsiloxane film, ACS Appl. Mater. Interfaces. 10 (2018) 3652–3659.
- [185] T.X. Xiao, T. Jiang, J.X. Zhu, X. Liang, L. Xu, J.J. Shao, C.L. Zhang, J. Wang, Z.L. Wang, Silicone-based triboelectric nanogenerator for water wave energy harvesting, ACS Appl. Mater. Interfaces. 10 (2018) 3616–3623.
- [186] K. Dai, X. Wang, F. Yi, C. Jiang, R. Li, Z. You, Triboelectric nanogenerators as self-powered acceleration sensor under high-g impact, Nano Energy. 45 (2018) 84–93.
- [187] A. Šutka, J. Ruža, M. Järvekülg, A. Linarts, K. Mālnieks, V. Jurkāns, I. Gorņevs, J. Blūms, K. Rubenis, M. Knite, Triboelectric nanogenerator based on immersion precipitation derived highly porous ethyl cellulose, J. Electrostat. 92 (2018) 1–5.
- [188] S. Gao, M. Wang, Y. Chen, M. Tian, Y. Zhu, X. Wei, T. Jiang, An advanced electro-Fenton degradation system with triboelectric nanogenerator as electric supply and biomass-derived carbon materials as cathode catalyst, Nano Energy. 45 (2018) 21–27.
- [189] M.L. Seol, J.W. Han, D.I. Moon, K.J. Yoon, C.S. Hwang, M. Meyyappan, All-printed

- triboelectric nanogenerator, *Nano Energy*. 44 (2018) 82–88.
- [190] S. Li, D. Zhang, X. Meng, Q.A. Huang, C. Sun, Z.L. Wang, A flexible lithium-ion battery with quasi-solid gel electrolyte for storing pulsed energy generated by triboelectric nanogenerator, *Energy Storage Mater.* 12 (2018) 17–22.
- [191] G. Zhu, C. Pan, W. Guo, C.Y. Chen, Y. Zhou, R. Yu, Z.L. Wang, Triboelectric-generator-driven pulse electrodeposition for micropatterning, *Nano Lett.* 12 (2012) 4960–4965.
- [192] G.S.P. Castle, Contact charging between insulators, *J. Electrostat.* 40 (1997) 13–20.
- [193] E. Németh, V. Albrecht, G. Schubert, F. Simon, Polymer tribo-electric charging: dependence on thermodynamic surface properties and relative humidity, *J. Electrostat.* 58 (2003) 3–16.
- [194] M. Lungu, Electrical separation of plastic materials using the triboelectric effect, *Miner. Eng.* 17 (2004) 69–75.
- [195] S. Wang, L. Lin, Z.L. Wang, Nanoscale-triboelectric-effect enabled energy conversion for sustainable powering of portable electronics, *Nano Lett.* 12 (2012) 6339–46.
- [196] G. Zhu, Z. Lin, Q. Jing, P. Bai, C. Pan, Y. Yang, Y. Zhou, Z.L. Wang, toward large-scale energy harvesting by a nanoparticle-enhanced triboelectric nanogenerator, *Nano Lett.* 13 (2013) 847–853.
- [197] Y. Hu, J. Yang, Q. Jing, S. Niu, W. Wu, Z.L. Wang, Triboelectric nanogenerator built on suspended 3D spiral structure as vibration and positioning sensor and wave energy harvester, *ACS Nano*. 7 (2013) 10424–10432.
- [198] A.F. Diaz, R.M. Felix-Navarro, A semi-quantitative tribo-electric series for polymeric materials: the influence of chemical structure and properties, *J. Electrostat.* 62 (2004) 277–290.
- [199] G. Cheng, Z.H. Lin, L. Lin, Z.L. Du, Z.L. Wang, Pulsed nanogenerator with huge instantaneous output power density, *ACS Nano*. 7 (2013) 7383–7391.
- [200] H. Zhang, Y. Yang, Y. Su, J. Chen, C. Hu, Z. Wu, Y. Liu, C. Ping Wong, Y. Bando, Z.L. Wang, Triboelectric nanogenerator as self-powered active sensors for detecting liquid/gaseous water/ethanol, *Nano Energy*. 2 (2013) 693–701.
- [201] P. Bai, G. Zhu, Z.H. Lin, Q. Jing, J. Chen, G. Zhang, J. Ma, Z.L. Wang, Integrated multilayered triboelectric nanogenerator for harvesting biomechanical energy from human motions, *ACS Nano*. 7 (2013) 3713–3719.
- [202] F.R. Fan, J. Luo, W. Tang, C. Li, C. Zhang, Z. Tian, Z.L. Wang, Highly transparent and flexible triboelectric nanogenerators: performance improvements and fundamental

- mechanisms, *J. Mater. Chem. A*. 2 (2014) 13219–13225.
- [203] X.H. Li, C.B. Han, L.M. Zhang, Z.L. Wang, Cylindrical spiral triboelectric nanogenerator, *Nano Res.* 8 (2015) 3197–3204.
- [204] J. Sun, W. Li, G. Liu, W. Li, M. Chen, Triboelectric nanogenerator based on biocompatible polymer materials, *J. Phys. Chem. C*. 119 (2015) 9061–9068.
- [205] B.U. Ye, B.J. Kim, J. Ryu, J.Y. Lee, J.M. Baik, K. Hong, Electrospun ion gel nanofibers for flexible triboelectric nanogenerator: electrochemical effect on output power, *Nanoscale*. 7 (2015) 16189–16194.
- [206] B.K. Yun, J.W. Kim, H.S. Kim, K.W. Jung, Y. Yi, M.S. Jeong, J.H. Ko, J.H. Jung, Base-treated polydimethylsiloxane surfaces as enhanced triboelectric nanogenerators, *Nano Energy*. 15 (2015) 523–529.
- [207] T. Huang, M. Lu, H. Yu, Q. Zhang, H. Wang, M. Zhu, Enhanced power output of a triboelectric nanogenerator composed of electrospun nanofiber mats doped with graphene oxide, *Sci. Rep.* 5 (2015) 13942.
- [208] J. Chen, J. Yang, Z. Li, X. Fan, Y. Zi, Q. Jing, H. Guo, Z. Wen, K.C. Pradel, S. Niu, Z.L. Wang, Networks of triboelectric nanogenerators for harvesting water wave energy: A potential approach toward blue energy, *ACS Nano*. 9 (2015) 3324–3331.
- [209] L. Zhang, L. Jin, B. Zhang, W. Deng, H. Pan, J. Tang, M. Zhu, W. Yang, Multifunctional triboelectric nanogenerator based on porous micro-nickel foam to harvest mechanical energy, *Nano Energy*. 16 (2015) 516–523.
- [210] M.L. Seol, S.H. Lee, J.W. Han, D. Kim, G.H. Cho, Y.K. Choi, Impact of contact pressure on output voltage of triboelectric nanogenerator based on deformation of interfacial structures, *Nano Energy*. 17 (2015) 63–71.
- [211] S.J. Park, M.L. Seol, S.B. Jeon, D. Kim, D. Lee, Y.K. Choi, Surface engineering of triboelectric nanogenerator with an electrodeposited gold nanoflower structure., *Sci. Rep.* 5 (2015) 13866.
- [212] J. Chung, S. Lee, H. Yong, H. Moon, D. Choi, S. Lee, Self-packaging elastic bellows-type triboelectric nanogenerator, *Nano Energy*. 20 (2016) 84–93.
- [213] X. Wang, Y. Yin, F. Yi, K. Dai, S. Niu, Y. Han, Y. Zhang, Z. You, Bioinspired stretchable triboelectric nanogenerator as energy-harvesting skin for self-powered electronics, *Nano Energy*. 39 (2017) 429–436.
- [214] B.D. Chen, W. Tang, C. He, T. Jiang, L. Xu, L.P. Zhu, G.Q. Gu, J. Chen, J.J. Shao, J.J. Luo,



- Z.L. Wang, Ultrafine capillary-tube triboelectric nanogenerator as active sensor for microliquid biological and chemical sensing, *Adv. Mater. Technol.* 3 (2018) 1700229.
- [215] F. Yi, L. Lin, S. Niu, J. Yang, W. Wu, S. Wang, Q. Liao, Y. Zhang, Z.L. Wang, Self-powered trajectory, velocity, and acceleration tracking of a moving object/body using a triboelectric sensor, *Adv. Funct. Mater.* 24 (2014) 7488–7494.
- [216] Y. Su, G. Zhu, W. Yang, J. Yang, J. Chen, Q. Jing, Z. Wu, Y. Jiang, Z.L. Wang, Triboelectric sensor for self-powered tracking of object motion inside tubing, *ACS Nano.* 8 (2014) 3843–3850.
- [217] Y. Yang, H. Zhang, Z.H. Lin, Y.S. Zhou, Q. Jing, Y. Su, J. Yang, J. Chen, C. Hu, Z.L. Wang, Human skin based triboelectric nanogenerators for harvesting biomechanical energy and as self-powered active tactile sensor system, *ACS Nano.* 7 (2013) 9213–9222.
- [218] G. Zhu, W.Q. Yang, T. Zhang, Q. Jing, J. Chen, Y.S. Zhou, P. Bai, Z.L. Wang, Self-Powered, Ultrasensitive, Flexible Tactile Sensors Based on Contact Electrification, *Nano Lett.* 14 (2014) 3208–3213.
- [219] H. Zhang, Y. Yang, T.C. Hou, Y. Su, C. Hu, Z.L. Wang, Triboelectric nanogenerator built inside clothes for self-powered glucose biosensors, *Nano Energy.* 2 (2013) 1019–1024.
- [220] P. Bai, G. Zhu, Q. Jing, J. Yang, J. Chen, Y. Su, J. Ma, G. Zhang, Z.L. Wang, Membrane-based self-powered triboelectric sensors for pressure change detection and its uses in security surveillance and healthcare monitoring, *Adv. Funct. Mater.* 24 (2014) 5807–5813.
- [221] Y. Su, X. Wen, G. Zhu, J. Yang, J. Chen, P. Bai, Z. Wu, Y. Jiang, Z.L. Wang, Hybrid triboelectric nanogenerator for harvesting water wave energy and as a self-powered distress signal emitter, *Nano Energy.* 9 (2014) 186–195.
- [222] P.K. Yang, Z.H. Lin, K.C. Pradel, L. Lin, X. Li, X. Wen, J.H. He, Z.L. Wang, Paper-based origami triboelectric nanogenerators and self-powered pressure sensors, *ACS Nano.* 9 (2015) 901–907.
- [223] P. Bai, G. Zhu, Q. Jing, Y. Wu, J. Yang, J. Chen, J. Ma, G. Zhang, Z.L. Wang, Transparent and flexible barcode based on sliding electrification for self-powered identification systems, *Nano Energy.* 12 (2015) 278–286.
- [224] F. Saurenbach, D. Wollmann, B.D. Terris, A.F. Diaz, Force microscopy of ion-containing polymer surfaces: morphology and charge structure, *Langmuir.* 8 (1992) 1199–1203.
- [225] X.T. Zhang, O. Sato, M. Taguchi, Y. Einaga, T. Murakami, A. Fujishima, Self-cleaning particle coating with antireflection properties, *Chem. Mater.* 17 (2005) 696–700.

- [226] J. Ma, Y. Jie, J. Bian, T. Li, X. Cao, N. Wang, From triboelectric nanogenerator to self-powered smart floor: a minimalist design, *Nano Energy*. 39 (2017) 192–199.
- [227] M. Xu, Y.C. Wang, S.L. Zhang, W. Ding, J. Cheng, X. He, P. Zhang, Z. Wang, X. Pan, Z.L. Wang, An aeroelastic flutter based triboelectric nanogenerator as a self-powered active wind speed sensor in harsh environment, *Extrem. Mech. Lett.* 15 (2017) 122–129.
- [228] D. V Kosynkin, A.L. Higginbotham, A. Sinitskii, J.R. Lomeda, A. Dimiev, B.K. Price, J.M. Tour, Longitudinal unzipping of carbon nanotubes to form graphene nanoribbons, *Nature*. 458 (2009) 872–876.
- [229] P.B. Arthi G, L. BD, A simple approach to stepwise synthesis of graphene oxide nanomaterial, *J. Nanomed. Nanotechnol.* 6 (2015) 2–5.
- [230] J.G.S. Moo, B. Khezri, R.D. Webster, M. Pumera, Graphene oxides prepared by Hummers', Hofmann's, and Staudenmaier's Methods: Dramatic influences on heavy-metal-ion adsorption, *ChemPhysChem*. 15 (2014) 2922–2929.
- [231] Z. Ni, Y. Wang, T. Yu, Z. Shen, Raman spectroscopy and imaging of graphene, *Nano Res.* 1 (2008) 273–291.
- [232] J. Li, S. Ye, T. Li, X. Li, X. Yang, S. Ding, Preparation of Graphene Nanoribbons (GNRs) as an Electronic Component with the Multi-walled Carbon Nanotubes (MWCNTs), *Procedia Eng.* 102 (2015) 492–498.
- [233] S.A. Hasan, J.L. Rigueur, R.R. Harl, A.J. Krejci, I. Gonzalo-Juan, B.R. Rogers, J.H. Dickerson, Transferable Graphene Oxide Films with Tunable Microstructures, *ACS Nano*. 4 (2010) 7367–7372.
- [234] X. Cai, T. Lei, D. Sun, L. Lin, A critical analysis of the  $\alpha$ ,  $\beta$  and  $\gamma$  phases in poly(vinylidene fluoride) using FTIR, *RSC Adv.* 7 (2017) 15382–15389.
- [235] Z. Wang, J. Wang, Z. Li, P. Gong, J. Ren, H. Wang, X. Han, S. Yang, Cooperatively exfoliated fluorinated graphene with full-color emission, *RSC Adv.* 2 (2012) 11681.
- [236] J. Fang, X. Wang, T. Lin, Electrical power generator from randomly oriented electrospun poly(vinylidene fluoride) nanofibre membranes, *J. Mater. Chem.* 21 (2011) 11088.
- [237] D. Sengupta, A.G.P. Kottapalli, S.H. Chen, J.M. Miao, C.Y. Kwok, M.S. Triantafyllou, M.E. Warkiani, M. Asadnia, Characterization of single polyvinylidene fluoride (PVDF) nanofiber for flow sensing applications, *AIP Adv.* 7 (2017) 105205.
- [238] M.V. Jose, B.W. Steinert, V. Thomas, D.R. Dean, M.A. Abdalla, G. Price, G.M. Janowski, Morphology and mechanical properties of Nylon 6/MWNT nanofibers, *Polymer (Guildf)*.

48 (2007) 1096–1104.

- [239] S.K. Gupta, P. Singh, R. Kumar, PALS and physico-chemical study of swift heavy ions and gamma radiation irradiated polyamide nylon 66 polymer, *Vacuum*. 121 (2015) 177–186.
- [240] S.K. Tiwari, K. Verma, P. Saren, R. Oraon, A. De Adhikari, G.C. Nayak, V. Kumar, Manipulating selective dispersion of reduced graphene oxide in polycarbonate/nylon 66 based blend nanocomposites for improved thermo-mechanical properties, *RSC Adv.* 7 (2017) 22145–22155.
- [241] D.J. Lin, C.L. Chang, C.K. Lee, L.P. Cheng, Fine structure and crystallinity of porous Nylon 66 membranes prepared by phase inversion in the water/formic acid/Nylon 66 system, *Eur. Polym. J.* 42 (2006) 356–367.
- [242] V.K. Thakur, M.F. Lin, E.J. Tan, P.S. Lee, Green aqueous modification of fluoropolymers for energy storage applications, *J. Mater. Chem.* 22 (2012) 5951.
- [243] M.M. Ren, X. Wang, C.S. Dong, B.Y. Li, Y. Liu, T. Chen, P. Wu, Z. Cheng, X.Y. Liu, Reduction and transformation of fluorinated graphene induced by ultraviolet irradiation, *Phys. Chem. Chem. Phys.* 17 (2015) 24056–24062.
- [244] S. Dash, R.N.P. Choudhary, M.N. Goswami, Enhanced dielectric and ferroelectric properties of PVDF-BiFeO<sub>3</sub> composites in 0–3 connectivity, *J. Alloys Compd.* 715 (2017) 29–36.
- [245] E. Kabir, M. Khatun, L. Nasrin, M.J. Raihan, M. Rahman, Pure  $\beta$  -phase formation in polyvinylidene fluoride ( PVDF ) -carbon nanotube composites, *J. Phys. D: Appl. Phys.* 50 (2017) 163002.
- [246] D.B. Shinde, J. Debgupta, A. Kushwaha, M. Aslam, V.K. Pillai, Electrochemical unzipping of multi-walled carbon nanotubes for facile synthesis of high-quality graphene nanoribbons, *J. Am. Chem. Soc.* 133 (2011) 4168–4171.
- [247] R. Xing, Y. Li, H. Yu, Preparation of fluoro-functionalized graphene oxide via the Hunsdiecker reaction, *Chem. Commun.* 52 (2016) 390–393.
- [248] P.K. Watson, Z.Z. Yu, The Contact Electrification of Polymers and the Depth of Charge Penetration, *J. Electrostat.* 40–41 (1997) 67–72.
- [249] S. Niu, Z.L. Wang, Theoretical systems of triboelectric nanogenerators, *Nano Energy.* 14 (2015) 161–192.
- [250] S. Niu, S. Wang, L. Lin, Y. Liu, Y.S. Zhou, Y. Hu, Z.L. Wang, Theoretical study of contact-mode triboelectric nanogenerators as an effective power source, *Energy Environ. Sci.* 6 (2013) 3576–3583.

- [251] G. Zhu, B. Peng, J. Chen, Q. Jing, Z.L. Wang, Triboelectric nanogenerators as a new energy technology: From fundamentals, devices, to applications, *Nano Energy*. 14 (2015) 126–138.
- [252] H.S. Kim, I.K. Park, Enhanced output power from triboelectric nanogenerators based on electrospun Eu-doped polyvinylidene fluoride nanofibers, *J. Phys. Chem. Solids*. 117 (2018) 188–193.



## LIST OF PUBLICATIONS

---

### List of Publications:

1. **Navjot Kaur**, Jitendra Bahadur, Vinay Panwar, Pushpendra Singh, Keerti and Kaushik Pal, Effective energy harvesting from a single electrode based triboelectric nanogenerator for driving wearable devices, **Nature - Scientific Reports**, 6, 38835 (2016). DOI: 10.1038/srep38835. [I.F.: 4.2]
2. **Navjot Kaur** and Kaushik Pal, Triboelectric nanogenerator for mechanical energy harvester, **Energy Technology (Wiley)**, 6, 958-997 (2018). DOI:10.1002/ente.201700639 [I.F.: 3.175]
3. **Navjot Kaur** and Kaushik Pal, Fabrication of triboelectric nanogenerator using fluorinated-graphene nanoribbons and poly(vinylidene fluoride) composite nanofibers.

### Other Publications:

1. **Navjot Kaur** and Kaushik Pal, Enhanced magnetic properties of cobalt doped graphene nanoribbons, **Applied Physics A (Springer)**, 123, 259 (2017). DOI: 10.1007/s00339-017-0893-6 [I.F.: 1.784]



## PRESENTATIONS IN CONFERENCES

---

### International Conferences

1. Presented paper as Oral at **International Conference on Nanotechnology for Better Living** held at NIT Srinagar in collaboration with IIT Kanpur, Srinagar, India from May 26-30, 2016.
2. Presented paper as Oral at **Graphene Canada 2016** held at Montreal, Canada in October, 2016.

### National Conferences

1. Presented paper as Oral on **2<sup>nd</sup> National Conference on Innovations & Recent Trends in Engineering and Technology** held at Vyas Institute of Engineering & Technology, Jodhpur from April 14-15, 2017.

